PREDICTION OF TOOL TEMPERATURE DURING MACHINING OF TI-6AL-4V ALLOY WITH ATOMIZATION-BASED CUTTING FLUID SPRAY SYSTEM

BY

ASIF TANVEER

THESIS

Submitted in partial fulfillment of the requirements
for the degree of Master of Science in Mechanical Engineering
in the Graduate College of the
University of Illinois at Urbana-Champaign, 2015

Urbana, Illinois

Adviser:

Professor Shiv G. Kapoor

ABSTRACT

Atomization-based cutting fluid (ACF) spray system is being sought as an alternative to cooling processes currently used for machining difficult-to-cut materials such as Ti-6Al-4V alloy. The ACF spray system generates a stream of monodispersed droplets of cutting fluid which then gets mixed in a high-velocity gas flow to form a focused axisymmetric jet of droplets. During machining, this jet is able to penetrate the small region of the tool-chip interface helping in lubrication and cooling of the interface. The advantage of the ACF spray system is that it requires very small amount of cutting fluid, which makes the system more energy efficient and environmentally friendly. It has been recently reported that ACF spray system improves machining performances including tool life and reduced temperature near the tool-chip interface in turning Ti-alloy. It is clear from these studies that the reduction in temperature and improvement in machining are mainly dependent on the interaction of the cutting fluid from the ACF spray system with the chip-tool interface. Therefore, it is imperative to have a physics-based understanding of the phenomena taking place at the interface that is responsible for the tool temperature reduction.

In this study, a thermal model for the atomization-based cutting fluid (ACF) spray system is developed to predict the temperature of the cutting edge of the tool during machining of titanium alloys. In the model, film boiling is taken into account because of the high temperatures involved in turning of Ti-6Al-4V alloy. Due to film boiling a thin vapor film is formed between the heated tool surface and the droplet. Heat is being conducted away from the tool through this film. It is shown that the thermal model is able to predict the temperature reduction due to ACF spray cooling and the predicted temperature profile is comparable to the experimental results.

ACKNOWLEDGMENTS

I would like first to thank my adviser Professor Shiv G. Kapoor, Postdoc Dr. Deepak Marla and Postdoc Dr. Chandra Nath for their constant guidance and knowledge that made this research possible. I would also like to thank the Grayce Wicall Gauthier Chair for funding this research. Thanks to the UIUC MechSE machine shop for their fine EDM work. This research was supported by the grant from NSF CMMI 12-33944.

I would also like to thank Soham Mujumdar, Alex Hoyne, James Zhu, Arvind Pattabhiraman and Surojit Ganguly for their valuable input into my research.

TABLE OF CONTENTS

LIST OF TABLES

LIST OF FIGURES

LIST OF ABBREVIATIONS

α	Contact angle at maximum spreading length
d	Diameter of droplet before impingement
D_{max}	Maximum spread diameter of droplet
dr, dz	Differential vapor cell volume dimensions
dt	Differential time
dT	Differential temperature
E_1	Initial energy of droplet just before impact
E_2	Final energy of droplet after impact
g	Acceleration due to gravity
k_c	Thermal conductivity of tool material
k_v	Thermal conductivity of vapor
K_1	Kinetic energy of droplet just before impact
K_2	Kinetic energy of droplet after impact
L_v	Latent heat of vapor
p	Pressure of vapor
q''	Boiling heat flux
q''	Heat flux generated during cutting
r	Horizontal coordinate describing radius of droplet spread
r_0	Droplet spread radius
S_{BC}	Surface area at the interface of liquid and vapor

S_{BAC}	Top surface area liquid droplet
$S_{lg,1}$	Initial liquid-air surface energy
$S_{sg,1}$	Initial solid-air surface energy
$S_{lg,2}$	Final liquid-air surface energy
$S_{sg,2}$	Final solid-air surface energy
t	Time domain
T	Temperature
T_s	Tool surface temperature
T_b	Boiling temperature
u	Axial vapor velocity
v	Radial vapor velocity
$V(0)$	Initial droplet volume
$V(t)$	Liquid volume
z	Vertical coordinate describing thickness of droplet
δ	Vapor film thickness
θ	Contact angle at equilibrium
σ_{lg}	Liquid-air surface tension
σ_{sg}	Solid-air surface tension
σ_{sl}	Solid-liquid surface tension
ρ_v	Vapor density
ρ_l	Liquid density
μ_v	Dynamic viscosity of vapor
ζ_{max}	Ratio of maximum droplet spreading length

CHAPTER 1

INTRODUCTION

1.1 Background and Motivation

Titanium and its alloys have a high demand in the biomedical, aerospace, automotive, and precision industries due to their unique physical and mechanical properties such as high strength-to-weight ratio, high corrosion and wear resistance, durability, and biocompatibility [1, 2, 3, 4, 5]. However, some thermophysical and mechanical properties of titanium such as low thermal conductivity, low elongation-to-break ratio, low elastic modulus, and high strength at elevated temperatures pose serious challenges to machining processes as extreme temperatures over 600°C may develop within the small tool-chip interface causing accelerated tool wear and reduced tool life [1, 6].

To improve tool life, the atomized cutting fluid (ACF) spray system has recently been introduced as a viable solution over the conventional flood cooling[7, 8]. The ACF spray system generates monodispersed droplets with the help of an ultrasonic generator. The low-velocity droplets are carried by a high-velocity gas (air or CO_2), which then impinges onto the surface of the tool and penetrates the chip-tool interface. This in turn cools the surface

and reduces the temperature of the tool. The system is also environmental friendly as it uses cutting fluid as low as 20 mL/min [9]. In comparison to other cooling techniques such as high-pressure cooling and cryogenic cooling, the ACF spray system uses less energy, thus making it energy efficient. Nath *et al.* [7] developed the system for turning of Ti-6Al-4V to study droplet spray characteristics including droplet entrainment zone (e.g., angle and distance) and droplet-gas co-flow development regions with respect to droplet and gas velocities, and spray distance. It was found that a high droplet velocity, a low gas velocity and a longer spray distance significantly improve tool life and surface finish. Hoyne *et al.* [9] also performed experiments on the ACF spray system and came to a conclusion that a thin film forms at the cutting interface during spraying and might have tendency to penetrate into the toolchip interface with the use of the ACF spray system. In a separate study by the same authors [10], inserted thermocouple technique was used to measure and map cutting zone temperatures at different locations inside the tool during turning of Ti-6Al-4V. The mapped temperature profiles further indicated that the average temperature of the tool during ACF spray system with CO_2 is reduced, thereby indicating a longer tool life.

Although it has been established from the studies by Hoyne *et al.* [10] that temperature decrease in the tool has a correlation with ACF spray cooling, it has not been verified if the cutting fluid film formation at the cutting interface is directly responsible for the temperature reduction. Additionally,

measuring temperature near the cutting edge has proven to be challenging owing to difficulties in setting the inserted thermocouple inside the tool close to the cutting edge. Using other temperature measuring techniques near the cutting zone such as pyrometry to take infrared photos of the tool for determining the tool temperature is difficult since the spray and the chip formed interfere with the imaging [11]. A model-based approach however, may be helpful in predicting the temperature profile of the tool and also may help to explain how the heat transfer phenomenon associated with the ACF spray system is responsible for the reduction in tool temperature in general.

A limited number of predictive cutting temperature models have been proposed for titanium machining applications. Two-dimensional analytical models by Loewen *et al.* [12] and Weiner *et al.* [13] tried to predict the temperature in the tool and chip but the models neglected the interaction of air or cutting fluid in the surrounding. Radulescu *et al.* [14] formulated a 3D transient analytical thermal model but it also suffered the limitation of overlooking any fluid interaction with the cutting interface. Anagonye *et al.* [15] studied the influence of tool geometry on cutting temperature for titanium alloy machining using finite element techniques and showed that increasing tool nose radius decreases the peak temperature reached in the tool. Li *et al.* [16] modeled the turning of titanium alloy numerically in 3D to predict the cutting forces and temperatures and showed a direct correlation with cutting speed and chip-tool interface temperature. However, the

temperature prediction for the model was not validated with the experimental data. Sima *et al.* [17] modeled the cutting temperature during high-speed machining of Ti-6Al-4V using a modified Johnson-Cook (JC) equation and predicted the effect of various tool coatings on temperature of the tool. A finite element study using JC model wasn also performed by Karpat *et al.* [18] to predict the temperature of the chip. However, in this study the model-predicted cutting temperatures and the temperature gradient on the forming chip were not validated. Thepsonthi *et al.* [19] used finite element model to predict the effect of tool coating on the cutting zone temperature by defining temperature-dependent strain softening terms in the model. Results show that cBN coating has a lower cutting temperature and also has a lower wear rate during milling of Ti-6Al-4V. Pervaiz *et al.* [20] conducted a finite element simulation coupled with CFD simulation to predict the temperature distribution in tool during Ti-6Al-4V machining in the presence of dry air. In this study, the temperature distribution of the cutting tool is estimated by considering the solid-fluid interface. However, by considering the flow of air only, this model can only be extended to simulate MQL and flood cooling techniques. While these models can be modified to different work materials they are all concerned with dry cutting and do not include the application of cutting fluid in the prediction of tool temperatures.

On the spray system modeling front, there are a few droplet and spray heat transfer models in the literature but majority of them deal with temperatures

that are lower than the cutting zone temperature usually found during titanium machining. Zhao *et al.* [21] formulated a droplet impact and heat transfer model for water and liquid metal droplets on a glass substrate but the study focused mainly on the impact shape of the droplets and considered time-dependent solidification by cooling only. Mehmet *et al.* [22] modeled unsteady convective heat transfer for fuel droplets but the work focused on the heat transfer between droplet and the ambient gas only and did not include any validation of the model predictions. Sazhin *et al.* [23] modeled droplet heat transfer model of biodiesel. However, it focused the temperature at boiling point only. Yang *et al.* [24] considered film boiling in their 3D modeling of droplet heat transfer, but did not account for the variable surface temperature and the heat generation. Nishio *et al.* [25] modeled heat transfer of dilute spray impinging on hot surface but included only convective and conductive heat transfer. Bernardin *et al.* [26] also studied spray thermal model and focused on film boiling but relied on empirical correlations for the heat flux from other previous studies.

In summary, measurement of tool temperature in titanium machining has always remained a challenge owing to the difficulty in accommodating thermocouples inside the tool and masking problems associated with infrared imaging. To overcome the issue, analytical and numerical models have been proposed as an alternative way to predict the tool temperature but they primarily deal with dry cutting and do not consider the effect of the cutting

fluid. On the other hand, models developed for droplet and spray cooling do not consider the high temperatures produced during titanium machining. In general, most of these studies do not address the effect of coolant on the temperature at the chip-tool interface during machining of titanium alloys. Therefore, a thermal model that will combine heat generation in tool and heat transfer from the tool due to cutting fluid to predict the tool temperature with the application of ACF spray system is required.

1.2 Research Objectives and Scope

1.2.1 Objectives

The main objective of this research is to develop a thermal model to predict the cutting tool temperature when machining titanium alloys using the ACF spray system. To accomplish this, the specific research objectives are:

1. To gain an understanding of the possible heat transfer mechanism that may take place at the cutting interface with the ACF spray system.

2. To formulate a physics-based model describing the influence of ACF spray cooling on the tool temperature during machining and predict the tool temperature profile.

3. To design parameters of the ACF spray system that will ensure spreading of the droplets, which in turn contributes to heat transfer and im-

prove tool life.

1.2.2 Research Scopes

This research focuses on the modeling of the heat transfer of droplets impinged on the heated surface of the tool to have a better understanding of the actual cooling mechanism of the ACF spray system that takes place during machining. The model consists of the tool geometry only and does not include the chip geometry. The boundaries of the model include the tool rake face that utilizes the chip-tool contact area for the heat source term, and a heat transfer coefficient is applied to the rest of the face. The flanks are exposed to ambient air and the rest of the tool faces are modeled as adiabatic walls. The tool material is selected to be tungsten carbide (WC). The model considers the heat transfer taking place in the tool for turning operation of titanium alloy and utilizes typical cutting conditions (speed: 80 m/min, depth of cut: 1.5 mm) to calculate the heat source term. For the ACF spray system, droplet sizes of 30 μm in diameter or less are used since the actual ACF spray utilizes monodisperse droplets with sizes in the order of μm.

For temperature measurement and validation, K-type (chromel-alumel) thermocouple is found to be suitable for use during the inserted thermocouple measurements of temperatures since it can withstand temperatures upto 1300°C [27]. Due to the difficulty in measuring the temperature exactly at

the cutting edge, distances of 0.15 mm, 0.25 mm, 0.35 mm and 0.45 mm from the cutting edge are validated instead.

1.2.3 Overview of the Thesis

Chapter 2 provides an overview of the literature on titanium machining, cooling techniques used in machining of titanium alloy, the ACF spray system, single droplet impingement dynamics, and thermal model predictions of temperatures generated during machining.

In Chapter 3 the methodology involved in ACF spray model and the heat transfer of an impinging droplet are described. Relevant assumptions involving the modeling are also highlighted.

Chapter 4 presents the results of the numerical models along with a study on the selection of optimal design parameters for the spray system to be effectively used in machining.

Chapter 5 discusses the results obtained from the thermal model and explains experimental procedures used for measurement and validation of temperatures in the tool. Experimental setup and cutting conditions are discussed and technique for measuring temperature using inserted thermocouples is showcased. Experiment for measuring and validation of the gas velocity is also highlighted

Finally, Chapter 6 summarizes the work and draws conclusions from the research findings.

CHAPTER 2

LITERATURE REVIEW

This chapter gives a synopsis of the available literature of the properties and machinability of titanium and its alloys, cooling techniques used in machining and the ACF spray system along with its spray dynamics and droplet impingement. Available literature concerning prediction of cutting temperatures in the tool and chip and current techniques used in thermal models for titanium machining is also reviewed. In addition to that, droplet and spray models focused on heat transfer are highlighted. The chapter then concludes with a review of gaps that exist in literature on prediction of cutting temperature in titanium machining.

2.1 Machining of titanium alloy

Over the last few decades, titanium alloys have found new applications in consumer industries including biomedical applications [4] and aviation industries [3]. In aircrafts, some of the parts and components that utilize titanium alloys include engine parts, rotors, compressor blades, landing gears, fasteners, hydraulic system components and nacelles. It is estimated that titanium, especially Ti-6Al-4V accounts for 50% of all alloys used in aircraft

industries [3]. In biomedical applications, titanium alloys are being developed as an alternative orthopedic and dental implant material. Such demand for these alloys is mainly attributed to their unique properties such as high strength-to-weight ratio, ability to withstand moderately high temperatures without creeping, and good corrosion and fracture resistance [1, 2].

Despite their inherent qualities, titanium alloys have certain metallurgical properties such as poor thermal conductivity and chemical affinity to most tool materials above 600^{o}C which cause rapid tool wear and make them difficult-to-machine materials [2, 1]. As a result, conventional processes of machining titanium involve downtime and loss in productivity.

2.1.1 Properties and applications of titanium alloy

Titanium alloys are found in applications where combination of weight, strength, corrosion resistance, and/or high temperature stability is required. The main reasons for using titanium in aerospace applications are:

- weight reduction (replacement for steels and Ni-based super-alloys)
- application temperature (substitute for Al alloys, Ni-based superalloys, and steels)
- corrosion resistance (substitute for Al alloys and low-alloyed steels)
- galvanic compatibility with polymer matrix composites (sub-stitute for Al alloys)

- space limitation (substitute for Al alloys and steels)

Weight saving is one of the primary reasons for using titanium since its alloys have high strength-to-weight ratio. The lower density of titanium compared to steel allows it to replace steel even though steel has a greater strength. On the other hand, it has significantly higher strength than aluminum [3]. This allows titanium alloys to be used in air frames and components of jet engines. Also, titanium can retain its strength at high operating temperatures and is able to outperform aluminum at places such as nacelles and auxiliary power units where temperatures in excess of 130^{o}C exist. Titanium also replaces aluminum and steel as material for landing gears of aircraft where correct amount of material is needed to sustain the high load.

The corrosion resistance of titanium alloys is such that protective coating is often not required, which saves weight. Due to this, much of the floor support structure under the galleys and lavatories is made of titanium.

Titanium is also galvanically compatible with materials such as carbon used in polymer matrix composites (PMC). Since PMCs are extensively used as composite structures in modern aircrafts, the selection of titanium over aluminum and steel is crucial [3].

In biomedical industries titanium and its alloys have found abundant usages due to their salient physical properties such as resistance to corrosion and biocompatibility [4]. Ideally, biomedical implants are required to be highly innocuous without any inflammatory or allergic reactions in human

body. An implant surgery being successful mainly depends on the reaction of human body to the implant, which evaluates the biocompatibility of a biomaterial. Titanium was proposed originally as an alternative for the 316L stainless steel and Co-Cr alloys owing to better biocompatibility and corrosion resistance [28], since stainless steels and Co-Cr alloys usually contain some harmful elements, such as Ni, Co and Cr.

Titanium-based alloys are also widely used for manufacturing orthopedic and dental devices under load-bearing applications [29]. Porous titanium alloys have been found to be suitable for porous implants since they exhibit a good combination of mechanical strength with low elastic modulus. Therefore, porous alloys can overcome the mechanical weakness of porous ceramics and polymeric materials as well as eliminating problems of biomechanical mismatch of elastic modulus. At the same time, they possess interconnected structure to provide space for maintenance of stable blood supply and ingrowth of new bone tissues. Interconnectivity is very important for porous biomaterials, as the connected pores allow cells to grow inside biomaterials and body fluid to circulate [30].

2.1.2 Metallurgy of Titanium Alloys

Titanium at its pure form undergoes an allotropic transformation at 882^oC. The close-packed hexagonal alpha structure is transformed into the body-centered cubic phase at this temperature. Alloying elements that are added

to titanium either stabilizes the alpha phase or the beta phase, which in turn, changes the transformation temperature. The elements that increase the transformation temperature are called alpha stabilizers and Al, O, N and C elements fall into this group. Mo, V, Cu and Nb decrease the transformation temperature and are known as beta stabilizers. Based on the presence of these stabilizers, titanium alloys are classified into three major groups: alpha alloys, alpha-beta alloys and beta alloys.

- Alpha (α) alloys: Alpha alloys have alpha stabilizers. The resulting microstructure provides excellent creep resistance and tensile strength at temperatures up to 300^oC and hence, alpha alloys used for high-temperature applications such as rotating components of turbines. [3].

- Beta (β) alloys: Beta alloys contain beta stabilizers and are characterized by high hardenability, high forgeability and improved fracture toughness at a given strength level. These alloys are thermally stable and are used as coil springs such as hydraulic return springs and flight control springs, as well as biomedical implants. [3].

- Alpha-beta ($\alpha - \beta$) alloys: Alpha-beta alloy is the most widely used titanium alloys in aerospace industries and consist of both alpha and beta stabilizers. It has good fatigue and fracture properties, and has high yield strength. As a result, it is used in components where static and fatigue strengths are important. These alloys also possesses good corrosion and high temperature resistances. In addition to all these

qualities, it is compatible with PMCs, and hence is a premiere metal for next-generation aircrafts where PMCs are used extensively [3].

2.1.3 Machinability of Titanium Alloys

Machinability of titanium alloys is poor in terms of tool life. The tool wears fast, which means the cutting speed must be kept low. This increases machining time and machining cost per part is automatically increased. Table 2.1 shows the machining time ratios for various types of titanium alloys compared to AISI 4340 steel at 300 BHN. Similarly, it takes over three times longer to manufacture titanium parts than to manufacture aluminum parts [5]. In this section, a review of the machinability of titanium alloys in terms of cutting force, temperature, surface roughness, chip formation and residual stresses is made in order to highlight the importance of difficulty in machining these alloys.

Table 2.1: Machining time ratios for various types of titanium alloys to AISI 4340 steel at 300 BHN [31]

TITANIUM ALLOY	TURNING (Carbide Tool)	FACE MILLING (Carbide Tool)	DRILLING (HSS Tool)
Commercially pure 175 BHN	0.7:1	1.4:1	0.7:1
α Ti-8Al-1Mo-1V 300 BHN	1.4:1	2.5:1	1:1
α-β Ti-6Al-4V 365 BHN	2.5:1	3.3:1	1.7:1
β Ti-13V-11Cr-3Al 400 BHN	5:1	10:1	10:1

Following points have been identified as the main factors for poor machinability of titanium alloys [1, 2]:

- Titanium chips are thin and have a small contact area with tool con-

sequently. This causes high stresses in tool.

- Titanium has strong chemical affinity with most tool materials at temperatures above 500^{o}C.
- The catastrophic thermoplastic shear process by which chips are formed.
- Titanium has low modulus of elasticity which can cause chatter, deflection, and rubbing problems.
- Titanium has a tendency to ignite during machining due to high temperatures involved.

Cutting Force

Studies on cutting force during machining of titanium alloys, namely Ti-6Al-4V, have been conducted by various authors [32, 33, **?**]. Experimental results by Sun *et al.* [32] on turning of Ti-6Al-4V show that all the three cutting conditions - feedrate, depth of cut and speed have influence on the cutting force. Figure 2.1 shows that as the feed-rate is increased the cutting force also increases in general. However, feed and thrust force components do not vary as much as the cutting force. It has also been observed that there is a variation in the amplitude of the cutting force and the oscillation is prominent at lower feeds. This is attributed to the low modulus of elasticity and high strength of titanium. With depth of cut the force also increases (see Fig. 2.1) as tool is plunged further into the material. This causes wear

of the tool and affects the tool life.

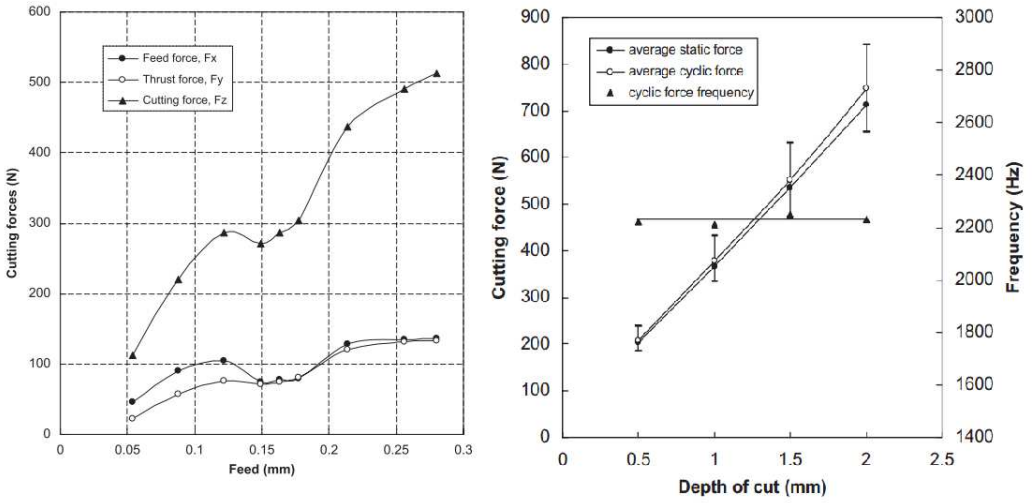

Figure 2.1: Effect of feed and depth of cut on cutting force at cutting speed of 75 m/min) [32]

Increase in the average cutting speed show a general decrease in the cutting force as observed by both Sun *et al.* [32] and Balaji *et al.* [33]. Results from the works of Sun *et al.* (see Fig. 2.2) show that cutting force increases initially with cutting speed up to 21 m/min due to strain hardening and then decreases dramatically with cutting speed from 21 to 57 m/min. This decrease is attributed to thermal softening due to the increased cutting temperature, which requires less work for shear failure and hence, lower average cutting forces. Therefore, the temperature sensitivity of the workpiece predominates over the strain rate sensitivity within the cutting speed range and force is decreased. However, the increase in temperature is detrimental to the tool and will cause rapid wear during machining at those cutting conditions.

Figure 2.3 shows the effect of the cutting speed and feed on the tool life as observed by Kahles *et al.* [34].

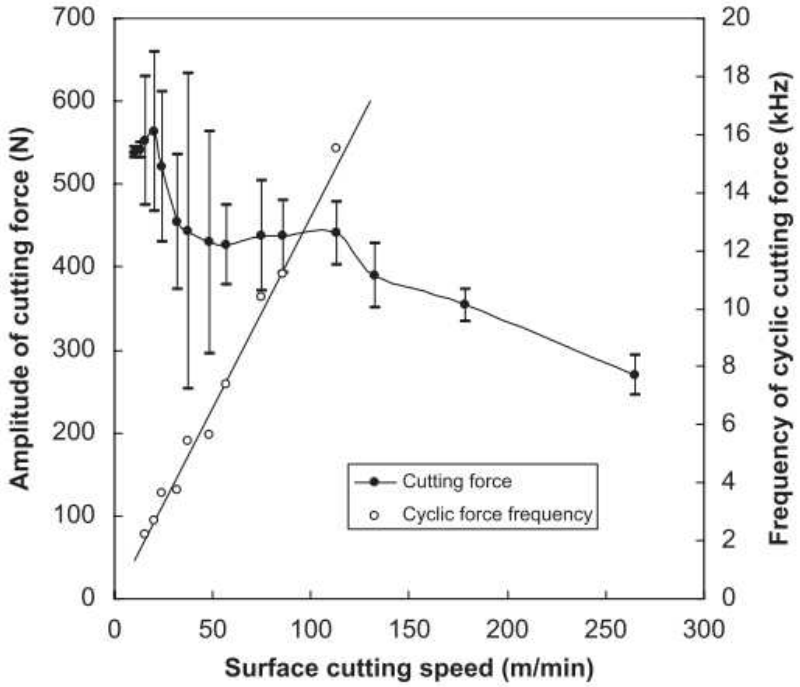

Figure 2.2: Effect of depth of cut and on cutting force at a cutting speed of 16 m/min and feed of 0.280 mm) [32]

During milling, cutting forces can also be high, as observed by Shi *et al.* [35] in their experimental study of the milling of a new damage-tolerant titanium alloy (TC21). Their results are shown in Fig. 2.4. Vijay *et al.* [36] also conducted experiments on end milling of Ti-6Al-4V and found similar trend in cutting force with the increase in the depth of cut and feed rate. This may be attributed to the unusually small chip-tool contact area on the rake face when machining titanium.

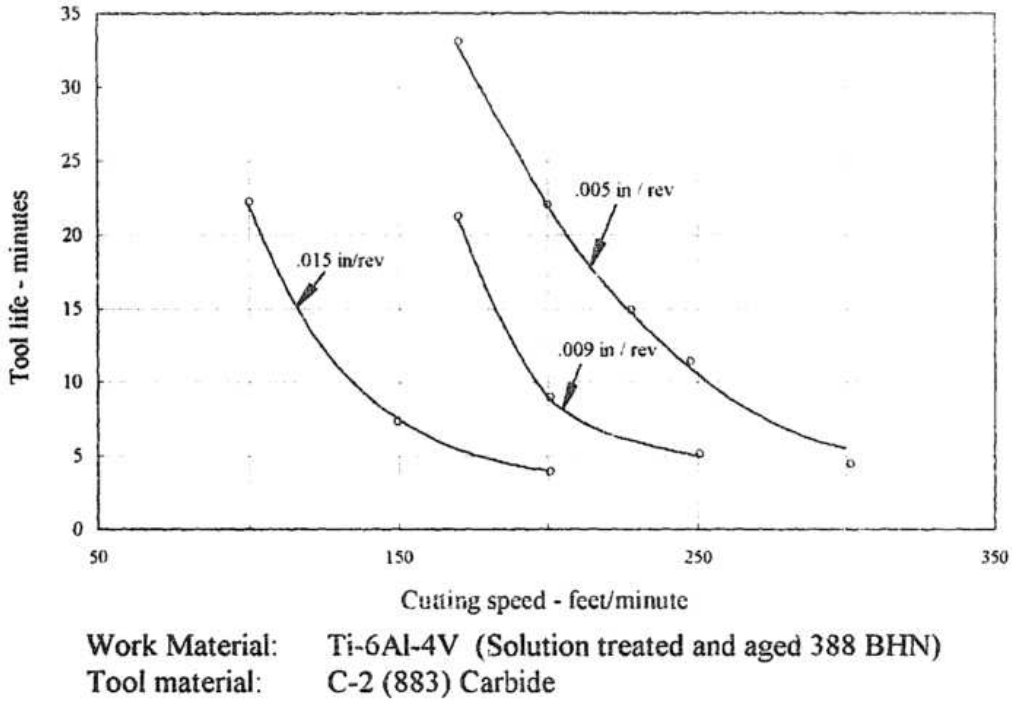

Figure 2.3: Effect of cutting speed and feed on tool life in turning Ti-6Al-4V) [34]

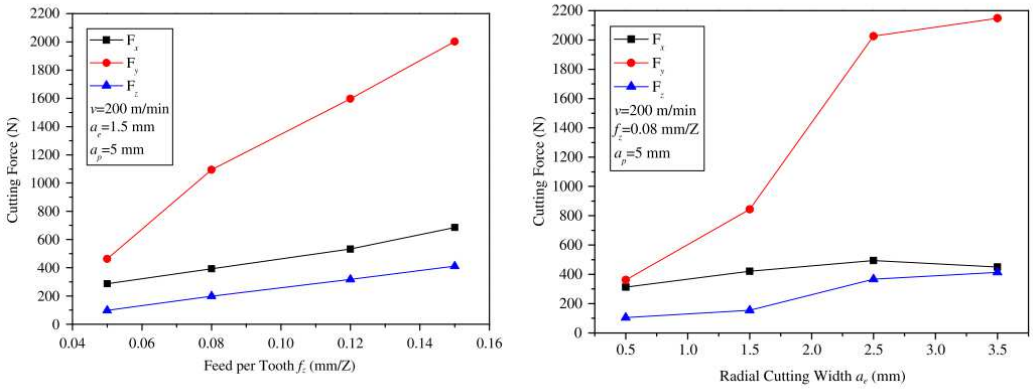

Figure 2.4: Effect of depth of cut and on cutting force during milling of TC21 alloy) [35]

Cutting Temperature

It is well known that high cutting temperatures are generated during machining of titanium alloys. High temperatures act close to the cutting edge of the tool and are responsible for the rapid tool wear observed in most machining operations [1]. This high temperature is attributed to the large proportion of heat generated when machining titanium alloys. This large amount of heat generated is conducted into the tool because it cannot be removed with the fast flowing chip or bed into the titanium alloy workpiece due to the low thermal conductivity of the alloy. The amount of heat absorbed by the tool can be as high as 80% compared to 50% when machining steel [37]. Figure 2.5 shows the relative distribution of the thermal load during machining titanium alloy and steel. It has been studied that the temperature gradient is very steep and the heat-affected zone is very small and closer to the cutting edge of the tool because of the thinner chips produced. The presence of a very thin flow zone between the chip and tool and the fact that titanium alloy has very low conductivity causes the tool tip to reach temepratures as high as 1100^{o}C [1, 38, 39].

Kitagawa *et al.* [40] studied the temperature and wear of sintered carbide tool in high-speed orthogonal turning of Ti-6Al-4V alloy. The authors constructed a thermocouple between an alumina-coated tungsten wire and the carbide inserts and created hot junctions on the rake face and within the tool to measure local temperatures. Figure 2.6 shows the mean temperature

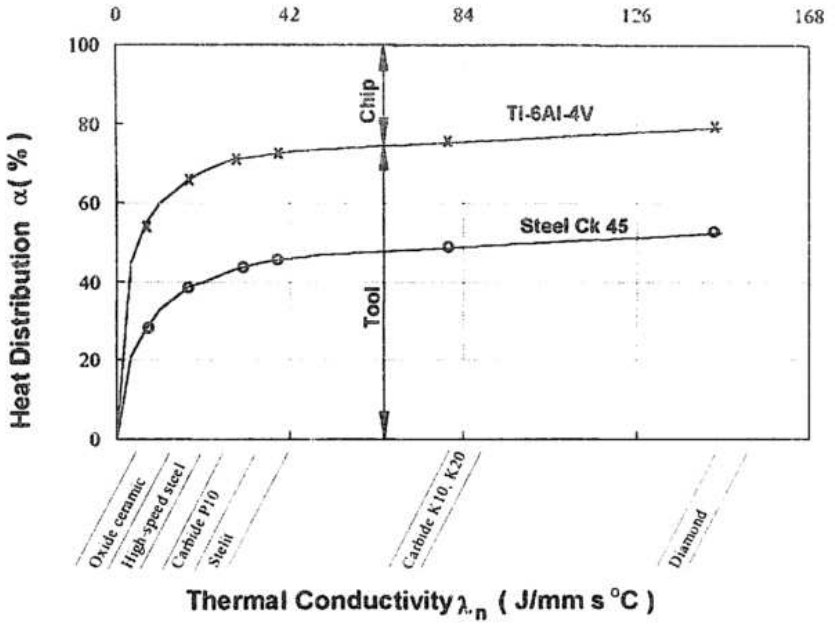

Figure 2.5: Distribution of thermal load during machining titanium alloys and steel) [37]

of the tool rake at varying cutting speeds measured by the authors. It can be seen that turning of titanium alloy can result in tool temperatures over 1000^oC.

Kitagawa *et al.* [40] further studied the effect of intermittent turning of titanium alloy and compared the temperature profile with that of continuous turning. Figure 2.7 shows the temperature data measured from both intermittent and continuous turning with and without cooling. Measurements in local tool temperatures at the tool-chip interface and the tool interior reveal that the maximum rake temperature is lower for intermittent cutting than for continuous cutting by approximately 15%. Therefore, feasibility of high-speed end milling depends on lower tool temperatures than in continuous

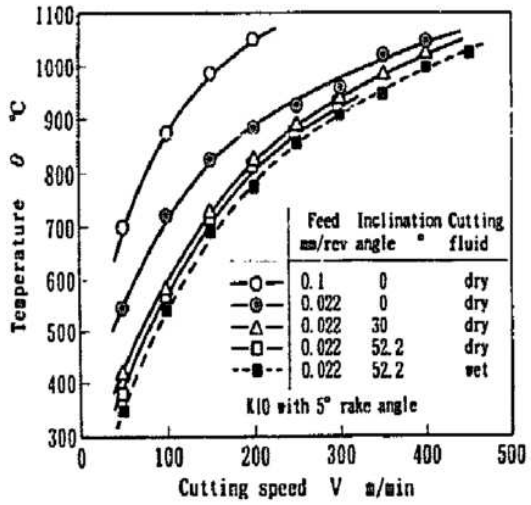

Figure 2.6: Mean rake temperature vs. culling speed in turning titanium alloy) [40]

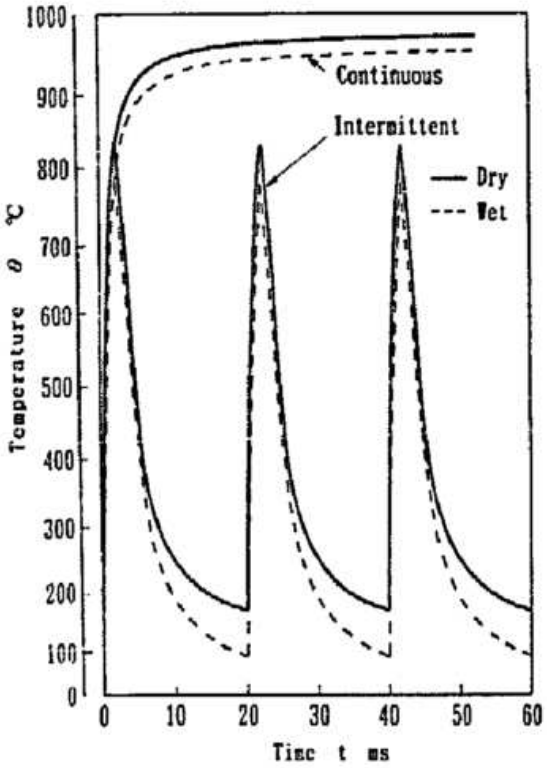

Figure 2.7: Measured rake temperature vs. time for 5 tool engagements at cutting speed of 100 m/min and feed-rate of 0.1 mm/rev) [40]

turning, owing to the time lag in temperature rise. Additionally, from this study it is clear that an efficient cooling technique is essential for reduced cutting temperature in turning of Ti-6Al-4V alloy and consequent longer tool life.

Infact, it has been observed that cutting speed has the most considerable influence on tool life; the tool life is extremely short at high cutting speeds but improves dramatically as the speed is reduced [1]. At higher cutting speed, thermal softening of the workpiece takes place as temperatures increase. This increased temperature is responsible for thermal degradation of tool wear.

Surface Roughness

There are many methods to quantify the surface integrity of a machined part, and the most widely used method is the surface roughness. It is considered to be the primary indicator of the quality of the surface finish [41]. The temperatures created during high-speed machining of titanium alloy were found to play a major role in tool wear, which is a significant factor in surface roughness of materials [40].

For turning, cutting speed has the most significant effect on surface roughness [42, 43]. Che-Haron *et al.*[42] have observed that surface roughness values at first decrease slightly with time with Ti-6Al-4V turning using uncoated carbide inserts (See Fig. 2.8). This is because when the tool is fresh, there can be micron-level sharp edges or peaks at its surface that can be

trimmed out to create a smoother contact surface with the workpiece as cutting proceeds. However, as time goes by, the surface roughness values increase sharply. This can be attributed to the deformation/wear of flank face or adherence of workpiece material at tool nose. In addition to this, it has been found that average surface roughness produced during machining using tungsten carbide inserts is lower compared to that using PCD for speeds of 40-80m/min [43].

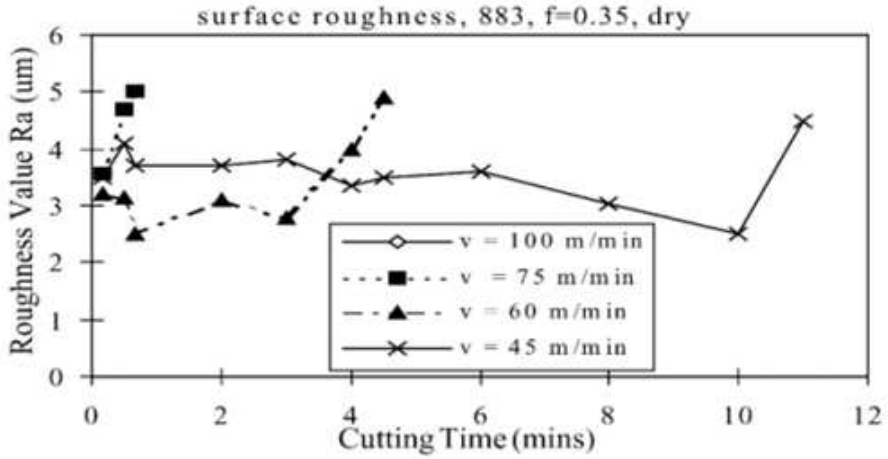

Figure 2.8: Typical surface roughness at feedrate of 0.35 mm/rev) [42]

Chip Morphology

Chip morphology and segmentation play a predominant role in determining the machinability of titanium alloy and tool wear. At lower cutting speeds the chip is often discontinuous, while the chip becomes serrated as the cutting speeds are increased [44]. Chip formation involves two fracture mechanisms of work material [45], ductile fracture mechanism caused by over-

strain under compressive stress and high-speed ductile fracture mechanism caused by strain concentration due to the local weakening by heat generation. The titanium chips form saw-tooth shape as a consequence of a catastrophic thermoplastic shear. This takes place when thermal softening in the primary shear zone due to high heat generation during high-speed machining, is equal or higher than the strain hardening produced by high strain rate. This leads to the formation of the shear bands. Komanduri *et al.* [46] studied the chip formation process during the cutting of Ti6Al4V and concluded that the catastrophic shear chip exists in all speed ranges and is independent of tool geometry. Figure 2.9 shows the segmented chips formed during machining of Ti-6Al-4V alloy.

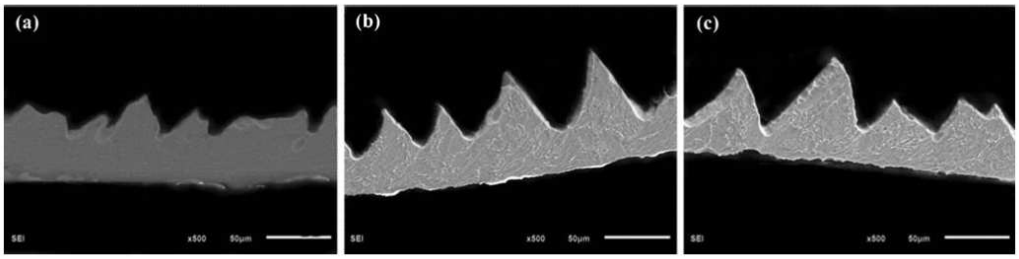

Figure 2.9: SEM images of cross-sectional top view of the major section of the chips at different cutting speeds. (a) 150 m/min. (b) 300 m/min. (c) 450 m/min) [47]

2.2 Cutting Fluid Application Techniques used in Machining

The high temperature and stresses developed at the cutting edge of the tool are the main reasons for the difficult machinability of titanium alloys. To address the problem, a cutting fluid needs to be applied as a basic rule. The cutting fluid not only acts as a coolant but also as a lubricant that reduces the tool friction and cutting forces, thus improving the tool life. Uninterrupted flow of coolant can also provide a good flushing action to remove chips and minimize the temperature. Additionally, a high pressure coolant supply can result in discontinuous and easily disposable chips, as opposed to the continuous chips produced in machining with conventional cooling methods [1].

Palanisamy *et al.* [48] studied the effect of the application of cutting fluid at high pressure during machining of titanium alloys. The authors observed that using high-pressure coolant during machining results in longer tool life and better surface finish on the machined material. Figure 2.10 shows that application of high-pressure cooling (90 bar) increases machining time and minimizes flank wear compared to low-pressure (6 bar) cooling. With low-pressure cooling the excessive temperature at the chip-tool interface can result in the welding of chips to the insert (Fig. 2.10a). This results in significant damage in the crater and flank section of the insert. This weakens the cutting edge and results in the edge breakdown. In high-pressure cooling,

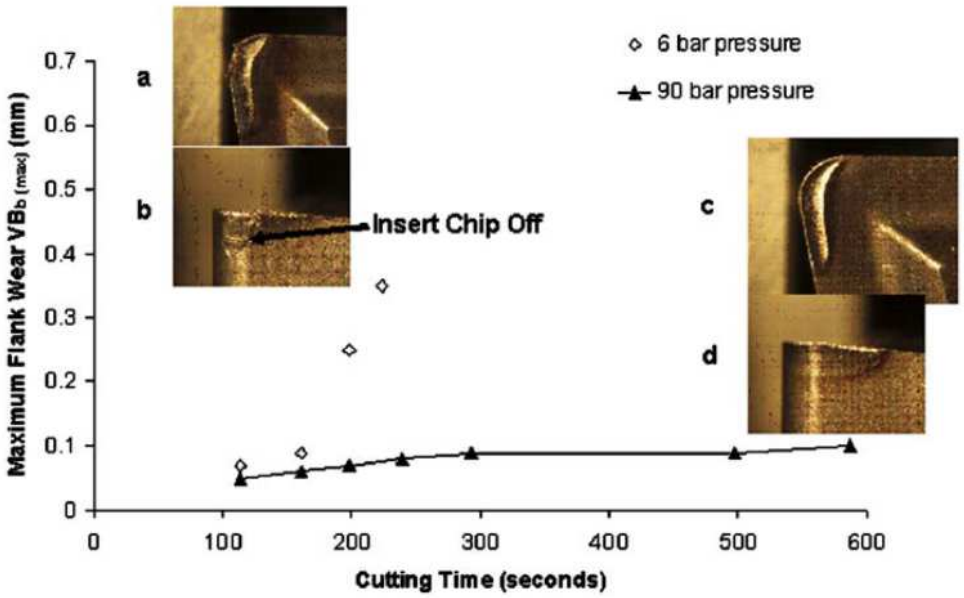

Figure 2.10: Tool wear along with (a) crater view and (b) flank view of the insert obtained after tool chip-off with the application of standard pressure coolant. (c) Crater view and (d) flank view of the insert obtained with the application of HPC) [48]

chip evacuation process by mechanical fracture is improved and this prevents welding of chips. In general, tool life increases with increasing coolant supply pressure from 6 to 90 bar. In addition, the authors concluded that high-pressure cooling improves tool temperature by directing fluid at the secondary cutting zone. They presume that cutting temperature decreases primarily by an increase in the effective heat transfer coefficient operating at the chip-tool interface.

Cryogenic cooling has also been studied extensively for the purpose of cooling in titanium alloy machining. It is basically a cooling system where liquefied gases such as nitrogen are used as the coolant. Hong *et al.* [49]

studied the effect of cryogenic cooling of liquid nitrogen (LN2) in Ti-6Al-4V numerically using FEM techniques and compared the tool temperature data with the experimental results. Fig. 2.11 shows the temperatures measured and predicted at the pick-up point and predicted maximum tool temperature, respectively, for various cooling conditions. The pick-up position is the location of the node in the FEM model where the center of the actual thermocouple bead is located. It is observed that cryogenic cooling reduces the tool temperature to a great extent compared to dry cutting. The results are also reflected by the works of Venugopal *et al.* [50] where the authors studied the tool wear in cryogenic turning of Ti-6Al-4V alloy. They studied flank wear, crater depth and edge depression and observed that cryogenic cooling had maximum effect on all these wears and performed better than conventional wet cooling. Figure 2.12 shows the different wears obtained from dry cutting, wet cooling and cryogenic cooling. Some of these wear mechanisms are thermally controlled. The authors concluded that such desirable control of tool wear can be attributed to more effective control of machining temperature under cryogenic cooling.

Although cryogenic cooling and high-pressure cooling improve tool life by reducing the temperature and enhancing lubrication, both these methods consume high amount of energy [7]. Compared to flood/wet cooling these processes offer the same productivity due to the large amount of cuttinf fluid required and/or energy consumed for liquefaction of cryogenic coolant

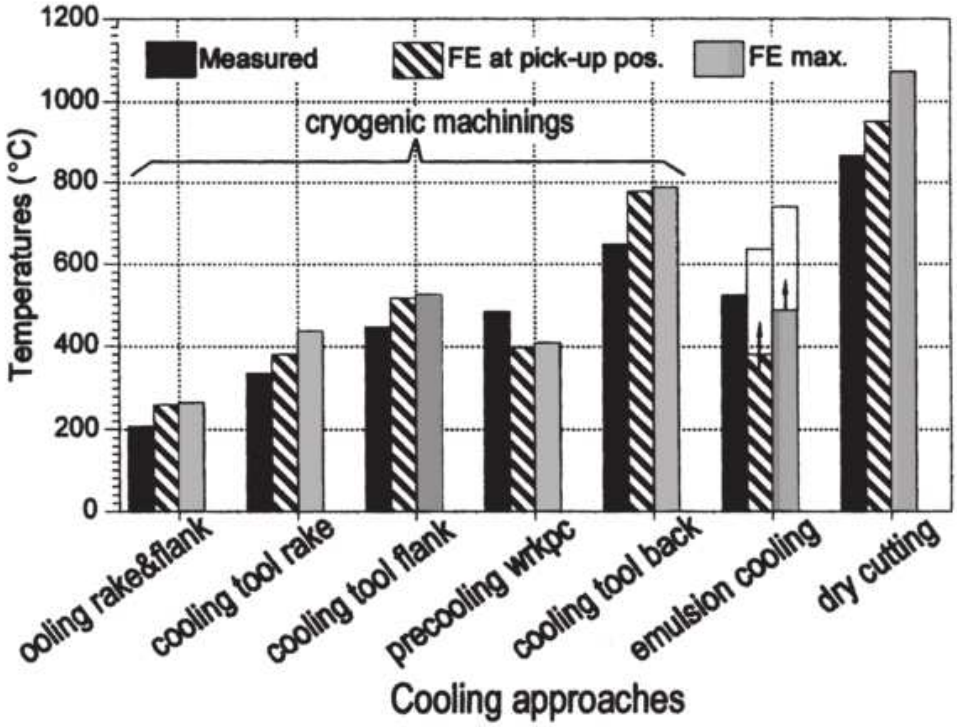

Figure 2.11: Predicted vs experimetnal tool temperature for cryogenic cooling of Ti-6Al-4V alloy) [49]

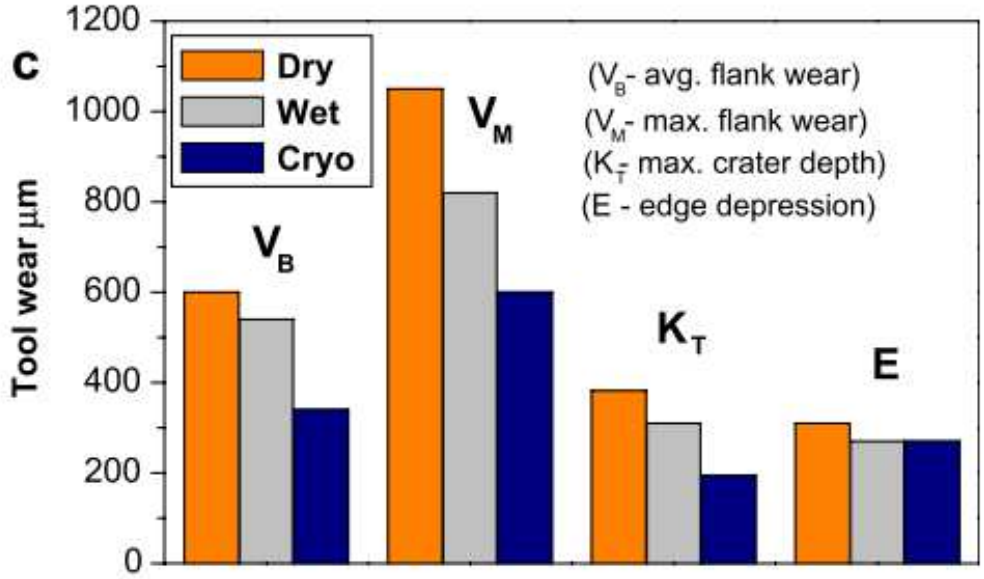

Figure 2.12: Predicted vs experimetnal tool temperature for cryogenic cooling of Ti-6Al-4V alloy) [50]

and for pumping high-pressure coolant. As a result, an alternative form of cooling method has recently been developed that consumes less energy and reduces the cutting temperature at the same time [9]. The new cooling method, known as the atomization-based cutting-fluid (ACF) spray system, has helped in reducing the tool temperature during machining [10] and has improved tool life by 40-50% over flood cooling [7]. A combination of spray system parameters used in the ACF spray system has shown improved machining performance such as tool life, cutting force, and chip breakability during titanium machining [7]. More details on the ACF spray system as one of the alternative cooling technologies is described in the next section.

2.3 ACF Spray System

The atomization-based cutting fluid (ACF) spray system was first proposed as an efficient cooling technique for micromachining [8]. Hoyne *et al.* [10] and Nath *et al.* [7] later showed that ACF spray system is able to successfully reduce the overall temperature of the tool and increase tool lifespan during turning of titanium alloys. In the study by Nath *et al.* [7], the ACF spray system was observed to reduce friction coefficient at the cutting interface, and improve tool life and surface finish during machining. Hoyne *et al.* [9] further studied the film that is formed after the spray from the ACF spray system impinges on the surface. From the study, it was established that there are three zones of film and the steady film zone is the most suit-

able for the cutting interface in machining for lubrication and temperature reduction. In addition, it was also observed experimentally in another study by the same authors [10] that the ACF spray system is able to reduce the tool temperature successfully.

2.3.1 ACF Spray System Components

The ACF spray system schematic is shown in Fig. 2.13. It consists of a cutting fluid reservoir, an ultrasonic atomizer, two coaxial nozzles of different diameters, and a gas supply system. The ultrasonic atomizer at one end that generates monodispersed spray droplets (e.g. $\sim 10-100\ \mu$m). There are two coaxial nozzles in the system, the droplet nozzle and the gas nozzle. The low-velocity droplets formed from the atomizer flow through the larger droplet nozzle that are then entrained by the high-velocity gas (e.g. air and/or CO_2) flowing through the inner gas nozzle. The entrainment is created by the pressure drop around the gas jet that draws in the droplets and carry them forward. This produces a focused axisymmetric jet of droplets that are impinged at the tool-chip interface. Upon impingement, the droplets interact with the heated tool/chip surface leading to heat transfer and vaporization of droplets that results in cooling of the tool/chip surface.

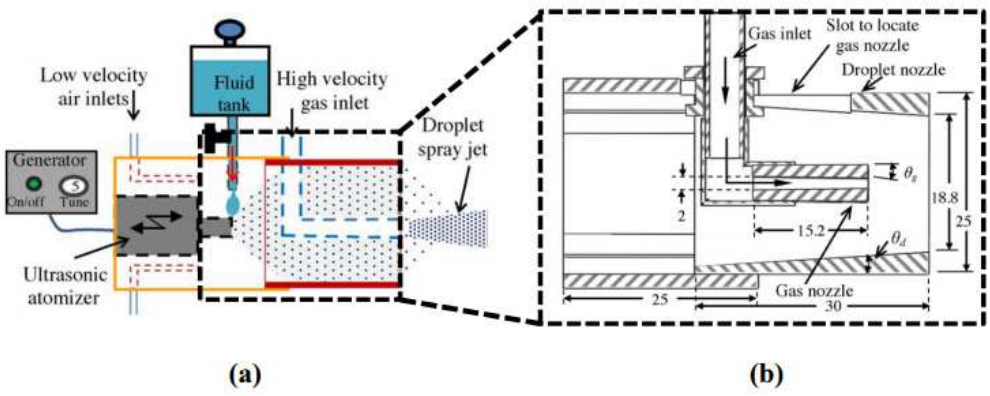

Figure 2.13: (a) Schematic of the ACF spray system and (b) Cross-section of coaxial nozzle system; θ_g: gas nozzle convergence, θ_d: droplet nozzle convergence [9]

2.3.2 Ultrasonic Atomization

There are two types of atomization methods: i) conventional atomizing where nozzles use mechanical energy to shear fluid into small drops, and ii) ultrasonic atomizing where the atomizers use only low vibrational energy for the generation of drops [51]. The ACF spray system uses ultrasonic atomizer for generating the droplets. In the ultrasonic atomizer, a liquid coming on to a solid surface gets disturbed through acoustic resonance and disintegrates into tiny droplets and leaves the surface in the form of a mist, as shown in Fig. 2.14. On the other hand, in the shearing action the liquid is atomized when two fluids moving in the same direction have a large difference in velocity. Due to this difference, instability occurs and the liquid breaks onto tiny droplets. Atomization by shearing gives a high flow rate. However, in this method, the droplets produced are not of uniform size. In addition,

pumps are required to produce the co-flowing jets of fluids, which require energy.

The ultrasonic atomizer is more suitable for machining applications [8] because it can generate droplets of uniform size and also do not require high pressure pump. This allows the ACF spray system to be more compact in design and also be more energy efficient. In addition, the droplets are of uniform size and have more controllability.

Since the ACF spray system uses a fluid with higher viscosity than that of water, the effect of the fluid viscosity should be considered when using the system. Sindayihebura *et al.* [52] studied experimentally the effects of physical properties of different fluid on mean diameter of droplets generated by ultrasonic atomization. They observed and photographed the structure of unstable surface waves which give rise to the droplets formation. They concluded from their studies that that the effect of the liquid viscosity on

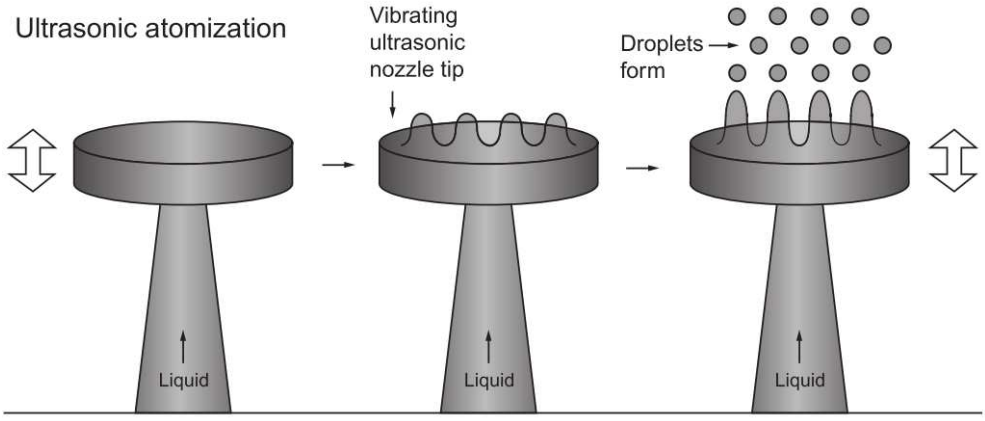

Figure 2.14: Schematic diagram of ultrasonic atomization [51]

the droplet mean diameter is insignificant. However, the effect of viscosity is significant for impingement characteristics as the droplets interact with the surface.

2.3.3 ACF spray dynamics and entrainment of droplets

The high-velocity gas coming out of the gas nozzle in the ACF spray system is responsible for the transport of droplets at a desired velocity to the surface of the tool. Nath *et al.* [7] studied the entrainment behavior of droplets in the high-velocity gas of the ACF spray system for machining titanium alloys. The study identified three zones that define droplet entrainment and mixing. The three regions of entrainment development are shown in Fig. 2.15.

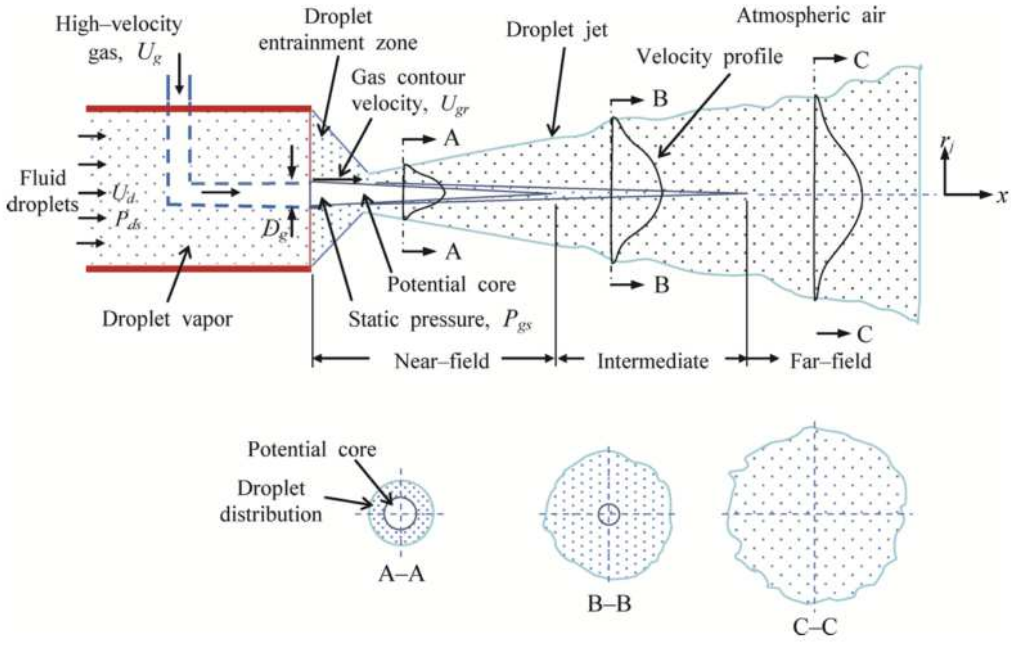

Figure 2.15: Schematic of the entrainment behavior of axisymmetric co-flow jet produced by a high-velocity gas and fluid droplets (AA, BB, and CC denote cross-sections at three different regions) [7]

In the first region called the near-field (NF) zone, a potential core is observed with the absence of any droplet generated by the ultrasonic atomizer. In this NF region, the vorticity is zero and as a result, no mixing of the fluids occurs. On the other hand, the droplets are distributed uniformly in the FF zone. In between the NF and the FF zone the droplets get entrained by the high-velocity gas. For the different conditions studied, the authors have reported that uniform distribution takes place at 25-35 mm or at $x/D_g > 16$. They have also observed that when droplet velocity increases and gas velocity decreases, the distance between the gas nozzle exit and the FF region becomes smaller. Finally, the authors concluded that having the spray distance outside the potential core ensured an even distribution of droplets and consequently an even fluid film formation in machining. Thus, a larger spray distance reduces friction coefficient at the cutting interface, and improves tool life and surface finish during machining.

Rukosuyev *et al.* [53] studied the effects of system parameters on ultrasonic cutting fluid application system in micro-machining. In this study the authors evaluated the focusing capability of the generated spray and the effects of different nozzle geometries and spray parameters (spray velocity). Figure 2.16 shows the different positions of the gas nozzle with respect to the droplet nozzle and Fig. 2.17 shows the resulting spray at those geometries and spray parameters (see Fig. 2.17 for the spray parameters). They concluded that the position of the nozzle with respect to the cutting zone is

important for the systems cooling and lubricating performance because the spray focuses at a specific point and then diverges. Also, for better focusing of the spray it is preferable to have the high speed air jet pipe within the nozzle and a converging slope for the nozzle.

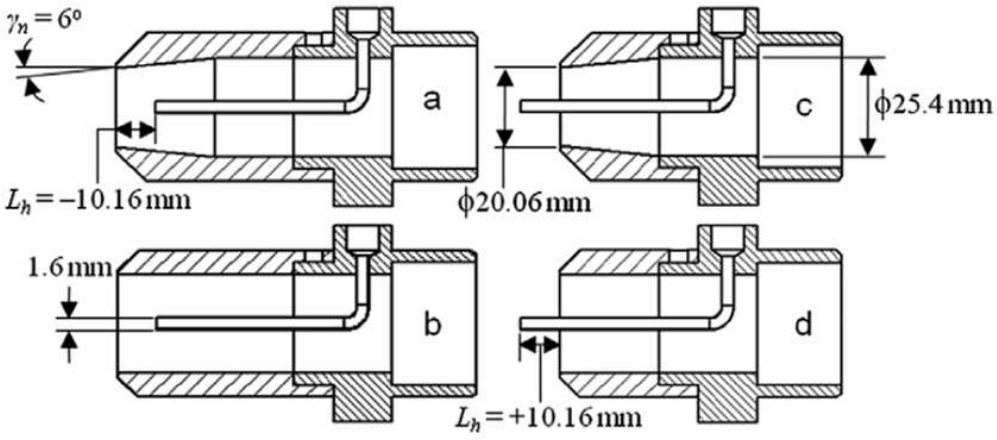

Figure 2.16: Four different nozzle geometries studied by Rukosuyev *et al.*with a. L_h=-10.16 mm and y_n=6^o, b. L_h=-10.16 mm and y_n=0^o, c. L_h=+10.16 mm and y_n=6^o, d. L_h=+10.16 mm and y_n=0^o [53]

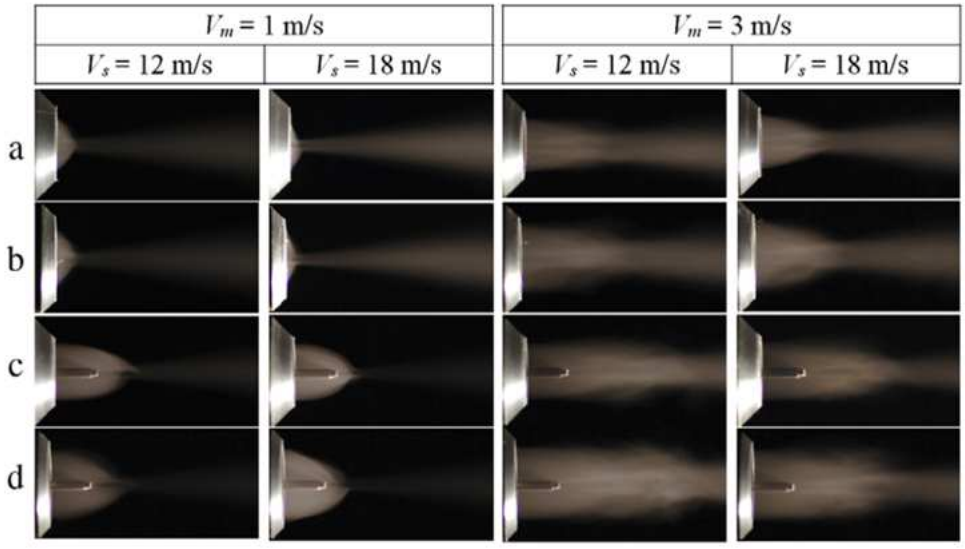

Figure 2.17: Spray behavior at different nozzle geometries [53]

2.3.4 Single droplet impingement behavior

Droplet dynamics and impingement regimes

Single droplet impingement behavior has been explored thoroughly in literature because it has found numerous applications in different industries such as in fuel injection systems of vehicles, spray painting and inkjet technology [54, 55, 56, 57]. In single droplet impingement, a droplet of specified diameter is allowed to interact with a wet or dry surface. Interaction can be of different types depending on the fluid properties of the droplet and droplet impingement velocities [58, 59]. In addition, the shape of the droplet [57], [56] and surface type are also important in determining the impact of the droplet [56, 60, 61]. Rein *et al.* [56] gave an overall outline of the possible situations that might be faced during droplet impingement based on the droplet shape, angle of impact and surface condition.

For ACF spray system oblique impact of spherical droplet on a dry surface or a wet surface with a thin film is of interest. Yarin *et al.* [58] states that the outcome of drop impact depends on the impact velocity, direction of the droplet relative to the surface, droplet size, properties of the liquid (its density, viscosity etc.), surface tension, roughness and wettability of the solid surface, non-isothermal effects (e.g., solidification and evaporation) and air entrapment. Several studies have been performed by varying these conditions and four interaction regimes have been identified. They are sticking, rebound, spreading and splashing regimes as shown in Fig. 2.18. These

regimes can be characterized by several non-dimensional numbers. These include: Reynolds number (Re), Ohnesorge number (Oh), Weber number (We) and non-dimensional number, K_m. Reynolds number Re is the ratio of the inertial force by viscous force and is characterized by,

$$Re = \frac{\rho v_d d_0}{\mu}, \tag{2.1}$$

where ρ is the density and is the dynamic viscosity of the fluid. The term d_0 represents characteristic length and v_d the impact velocity of the droplet. Ohnesorge number gives the relation between the inertial, viscous and surface tension forces and is given by,

$$Oh = \frac{\mu}{\sqrt{\rho \sigma d_0}}, \tag{2.2}$$

where σ is the surface tension of the liquid droplet. Weber number is defined as the ration of the droplet kinetic energy to the droplet surface energy and is mathematically written as:

$$We = \frac{\rho {v_d}^2 d_0}{\sigma} \tag{2.3}$$

The final non-dimensional number associated with droplet-surface interaction is K_m, and it is defined as a ratio between the Weber number and the Ohnesorge number:

$$K_m = \frac{We^{5/8}}{Oh^{1/4}} \tag{2.4}$$

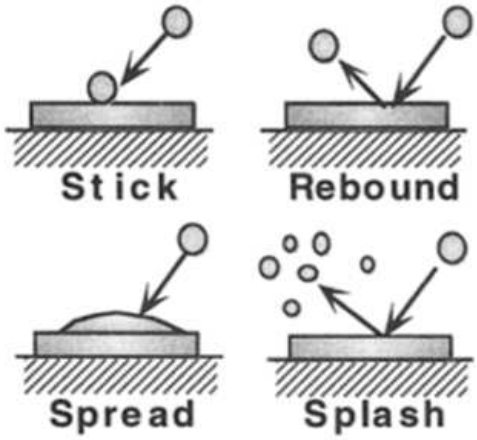

Figure 2.18: Droplet Impingement Regimes) [59]

It is important to define the ranges at which these regimes will occur because they will predict the droplet behavior after impact. For a particular liquid, if the velocity of impact is too low then sticking will occur. On the other hand, if the velocity is too high, the droplet will splash upon impact and disintegrate further into smaller droplets. For the droplet to spread and maximize the surface contact the velocity has to be in between these two extremes. In addition to the velocity, the change in properties of the liquid

will also affect the droplet impact regime. Based on these parameters, the non-dimensionless numbers discussed above will have ranges for which these regimes occur.

For the stick regime to occur, the Weber number needs to be less than 5, as reported by Jayaratne *et al.* [62], who studied the sticking regime of water droplets on wetted surface experimentally by varying the droplet diameter, velocity and impingement angle. Above this Weber number, rebound will take place. The rebound regime for water droplets on a fixed wetted surface is $5 < We < 10$, as reported by Stow *et al.* [63]. Above Weber number of 10, spreading occurs. This regime is of interest in ACF spray system cooling, since the droplet in this regime spreads to form maximum contact with the surface and can contribute to higher heat transfer rate. With higher impact energy the droplet breaks up into further smaller diameter droplets and splashing occurs. To distinguish between the spreading and the splashing regime the non-dimensionless number, K_m is used. Mundo *et al.* [64] used LED visualization technique to perform droplet impact tests on two different steel surfaces and developed the non-dimensional number K_m. The authors determined that the droplet will spread if $K_m < 57.7$ and splash otherwise (See Fig. 2.19).

For a surface at a temperature above Leidenfrost temperature of the liquid being used, the droplet may also break up or rebound and break up induced by boiling as stated by Bai *et al.* [65]. At such high temperatures, partial

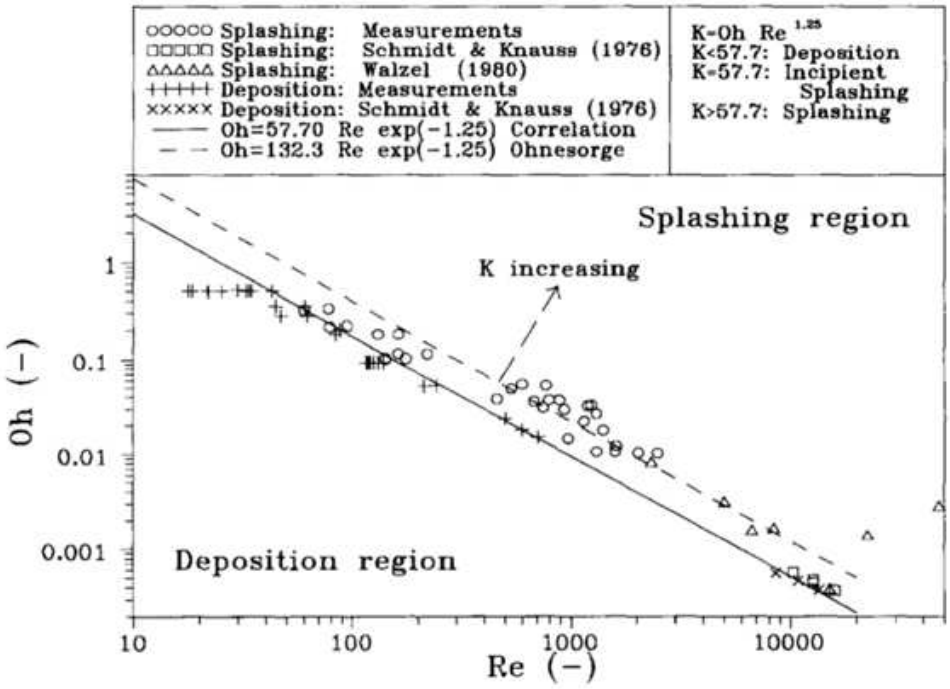

Figure 2.19: Spreading and splashing regimes for primary droplets) [64]

evaporation of droplet upon impact occurs and a thin film of vapor is formed underneath it.

It can be concluded that for maximum surface contact the droplet impact energy should be maximum without exceeding the spreading-splashing boundary. With maximum surface contact, the heat transfer rate and the cooling process will be improved. Therefore, for the machining application of the ACF spray system, the maximum impact energy should be cont rolled in a way so that the impingement behavior of the droplet falls within the spreading regime. According to the researches above, the spreading region is defined by $We > 10$ and $K_m < 57.7$. As a result, it is imperative to understand the impingement parameters that will describe this spreading

regime.

Modeling of the spreading of single droplet and spray impingement

A number of researchers have worked on modeling the dynamics of single droplet impingement. These studies are focused on the mechanism of crown formation and generation of secondary droplets. This is expected since there are a number of applications where splashing and consequent atomization of droplets are important, such as fuel spray inside combustion chambers [64, 66]. During ACF spray cooling, the droplet should spread with the highest energy without exceeding the spreading/splashing boundary so that maximum amount of area for the spreading is covered and droplets penetrate the chip-tool interface. Fukai *et al.* [67] created a model of an impinging droplet on a flat dry surface using mass continuity and momentum equations for a long time scale (greater than 1 second). In the model the authors studied the deformation of the droplet by accounting for the presence of inertial, viscous, gravitational, surface- tension, and wetting effects, including the phenomenon of contact-angle hysteresis. Experiments were also performed for a water droplet system in which impingement surfaces of different wettability were employed. The contact angles determined experimentally were used as input to the numerical model. The authors concluded that the theoretical model predicted well the deformation of the impacting droplet both during spreading and recoiling.

Ghai *et al.* [68] created a model of a spreading droplet during impact with a dry rotating surface by using conservation of energy and volume in a modified spherical cap approach. The authors also extended the work for oblique impacts on stationary dry surface by taking the tangential component of the impact velocity on the surface. Yarin *et al.* [69] modeled droplet impact behavior on a thin liquid film for weak impacts ($We < 40$) and established that crowning does not occur at low We numbers. Instead, the droplet upon impact on wetted surface at much longer times (of the order of 10^{-2} s) produces spreading patterns. A doughnut-like wave with a rim as shown in Figure 2.20 represents such a pattern of inertial spreading counteracted by surface tension.

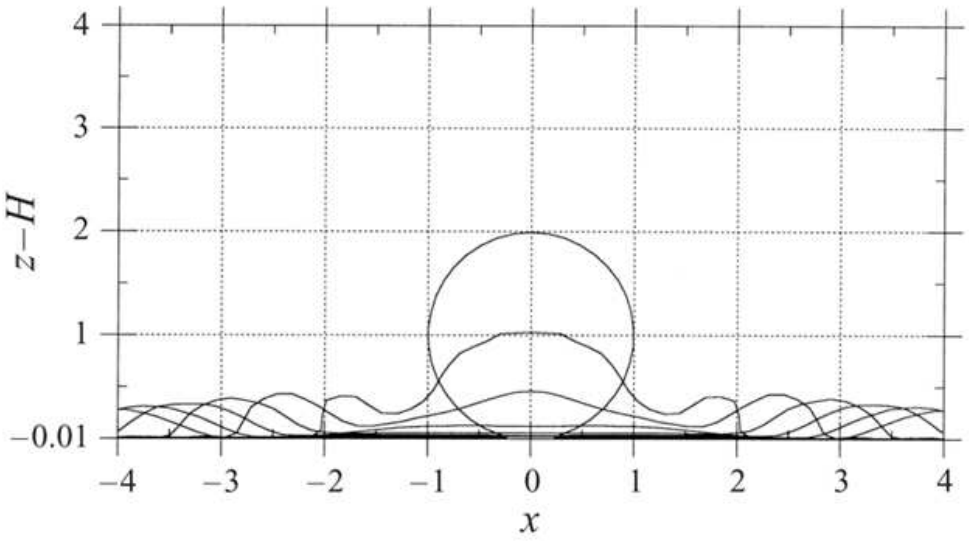

Figure 2.20: Evolution of droplet spread for We=20 and at times 0, 0.1, 0.2, 0.3, and 0.4 sec) [69]

Modeling of the ACF Spray Impingement

Since the ACF spray system is relatively a new technology, few works have been done regarding the modeling of the system to characterize and understand its operation. Hoyne *et al.* [9] developed a 3D thin fluid film model for the ACF spray system based on the NavierStokes equations for mass and momentum to predict the film thickness as it approaches the cutting interface. The model takes into account of the cross-film velocity profile, droplet impingement, pressure distributions and gasliquid shear interaction. The authors also measured the film thickness experimentally by using fluorescent dye and camera and identified three three distinct zones of the fluid film created by the ACF spray system: (1) impingement zone; (2) steady zone; and (3) unsteady zone. The three zones are shown in Fig. 2.21. The impingement zone features a fast moving unsteady thin film that is due to the disturbance of the high-velocity gas. The zone appears for a distance from point of impingement (DIP) of less than 3 mm. Beyond the impingement zone, the film reaches the steady zone, which features thickness values between 10 and 50 mm. After 7 mm, the film transitions to the unsteady zone and becomes rougher as waviness and wisps develop on the film surface. It was concluded from the experiments that the film present in the steady zone is the least disturbed and therefore, most desirable of the three zones at the chip-tool interface. The model developed the steady zone of the film, and it was found that the film thickness was comparable to the experimental

findings at the steady zone. The comparisons are shown in Fig. 2.22. It also validates the film thickness at perpendicular offset distances (POD) from the centerline. However, the model assumes that the film formation that takes place is on a cold surface, that is, any effect temperature is ignored in the model.

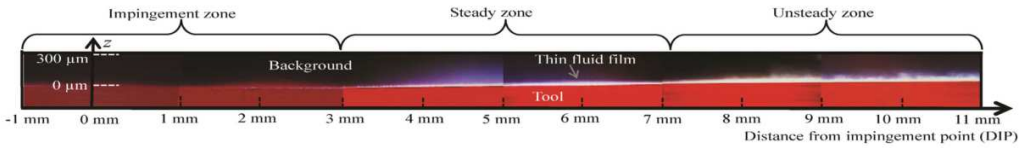

Figure 2.21: Side-view of spreading film) [9]

2.4 Prediction of Cutting Temperature in Machining

There are several cutting temperature models that exist for machining, and some of these studies are focused on studying and predicting the temperature generated in titanium machining. In this section, the analytical and numerical models for machining are reviewed.

Analytical tool temperature models available in the literature utilize energy balance to the tool-chip-work thermal system predict the cutting interface temperature distribution. Trigger *et al.* [70] used analytical methods to obtain the temperature distribution on an insert. It was shown that steady-state analysis predicts accurately the temperature distribution on the rake face of a rectangular insert. The two-dimensional analytical model by Loewen *et al.* [12] assumed a shear plane to be a heat source on a semi-infinite work-

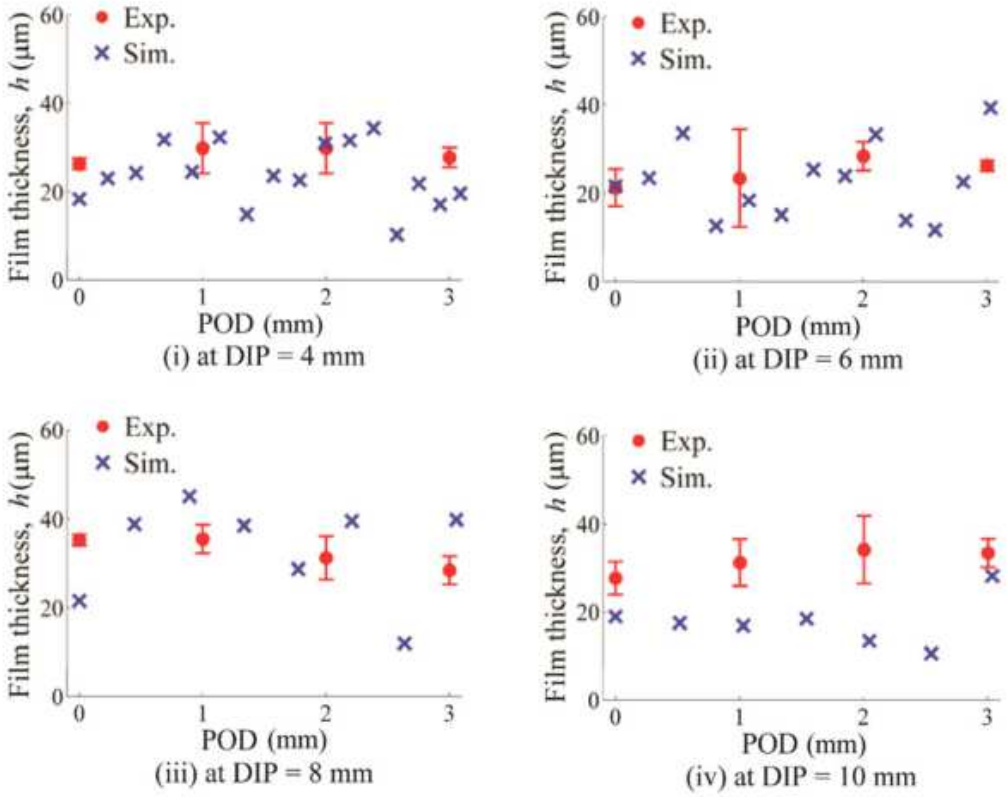

Figure 2.22: Experimental and predicted film thickness values over POD and DIP for:) [9]

piece. Weiner *et al.* [13] predicted the average tool interface temperature by also assuming that the shear plane was a heat source moving with a speed equal to the cutting speed over a semi-infinite workpiece. However, they neglected the heat flow in the direction of tool motion. In general, these models did not include the effect of air or cutting fluid on the temperature. Radulescu *et al.* [14] formulated a 3D transient analytical thermal model by using differential equations to define heat transfer of the tool and workpiece and validated with face-milling experiments on AISI 1018 and aluminum. Although the model could be modified for titanium machining conditions,

it also suffered the limitation of overlooking any fluid interaction with the cutting interface.

Anagonye *et al.* [15] have studied the influence of tool geometry on cutting temperature for orthogonal machining of titanium using finite element techniques using steady-state heat transfer conduction. Tool geometry consisted of tool nose radius and included angle of the tool. The results obtained from the model are shown in Fig. 2.23 and shows the influence of the two geometry parameters on the maximum cutting temperature. It can be seen that increasing both the tool nose radius and included angle (shape of insert) decrease the peak temperature reached in the tool. Although the authors predicted the trend using a tool-work thermocouple, the model temperature gradient results were not validated with the actual gradients.

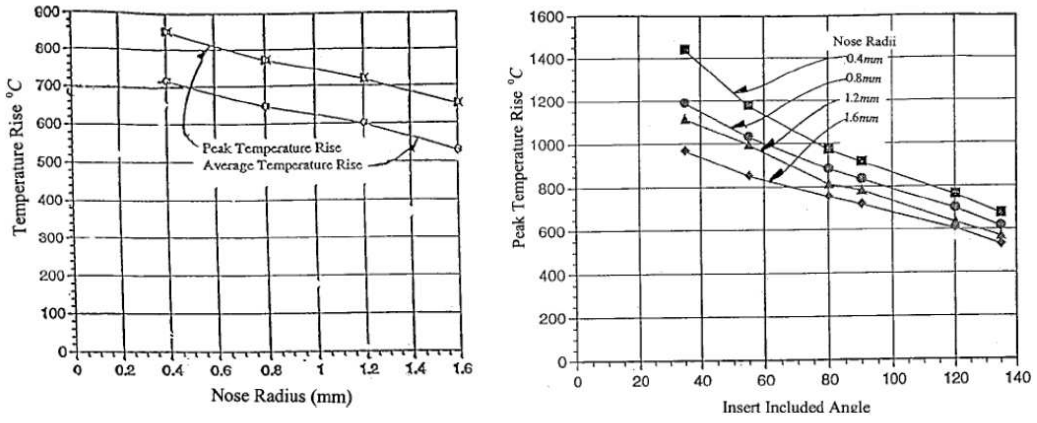

Figure 2.23: Influence of (a) the tool nose radius and (b) the included angle of the tool on the maximum cutting temperature [15]

Li *et al.* [16] modeled the three-dimensional turning of titanium alloy in

the commercially available AdvantEdge 3D simulation software. The work-material model in finite element analysis consists of the power-law strain hardening, thermal softening, and rate sensitivity. The authors investigated the effects of cutting speed on peak tool temperature and tool cutting edge radius on forces, chip thickness, and tool temperature. Six finite element simulations at two feeds and four cutting speeds were run to obtain the peak temperature on the tool rake face. The peak tool temperature data is shown in Fig. 2.24. Results show the temperature is independent of the feed and has a direct correlation with cutting speed. They also studied the effect of tool edge radius on the maximum temperature through the simulations. The results shown in Fig. 2.25 indicate that with increase in the tool edge radius, the peak temperature decreases. However, the authors did not validate any of the temperature profiles predicted in their work. They also generated chip temperature from the model by assuming that maximum chip and tool temperatures are same as they are in contact with one another.

A finite element study using Johnson-Cook (JC) model was performed by Karpat *et al.* [18] to predict the temperature of the chip. The study investigates the influence of various flow softening conditions on the finite element simulation outputs for machining titanium alloy Ti-6Al-4V. A new flow softening expression, which allows defining temperature-dependent flow softening behavior, is also proposed by the authors. In the model, assumption of rigid tool is maintained. Figure 2.26 shows the temperature contour of the

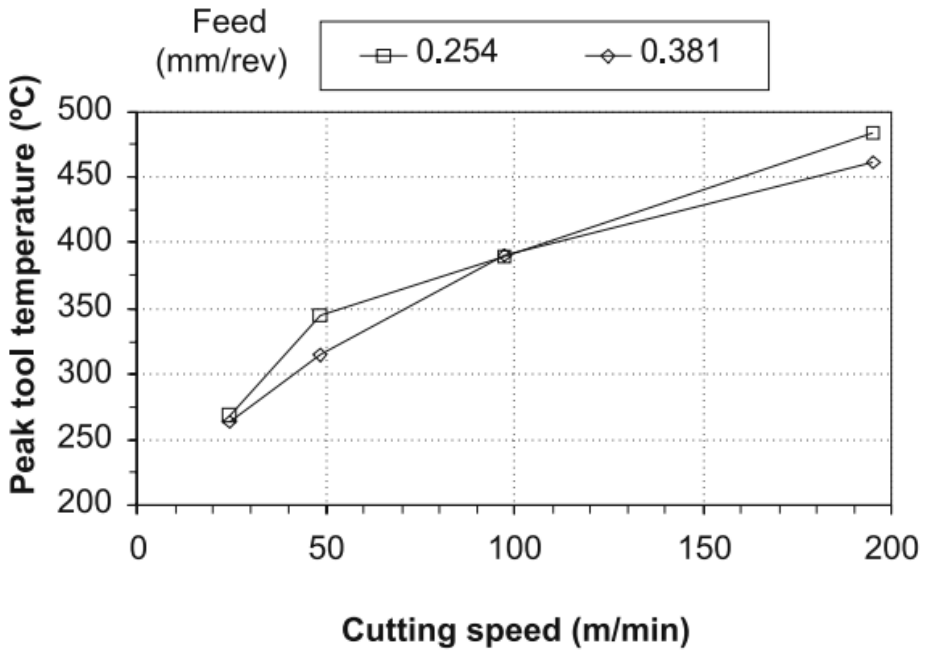

Figure 2.24: Peak tool temperature as a function of cutting speed [16]

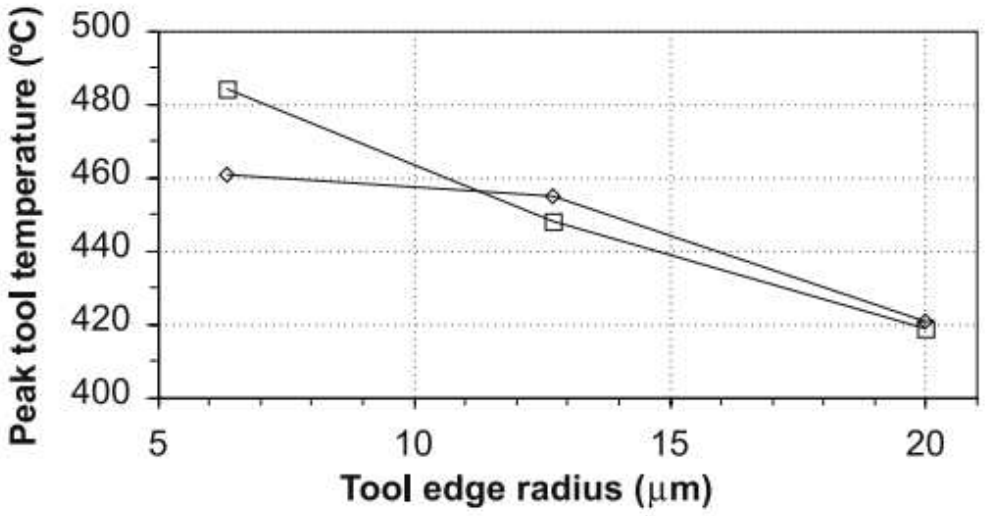

Figure 2.25: Peak tool temperature vs. tool edge radius speed [16]

chip predicted by the model.

Sima *et al.* [17] modeled the cutting temperature during the high-speed

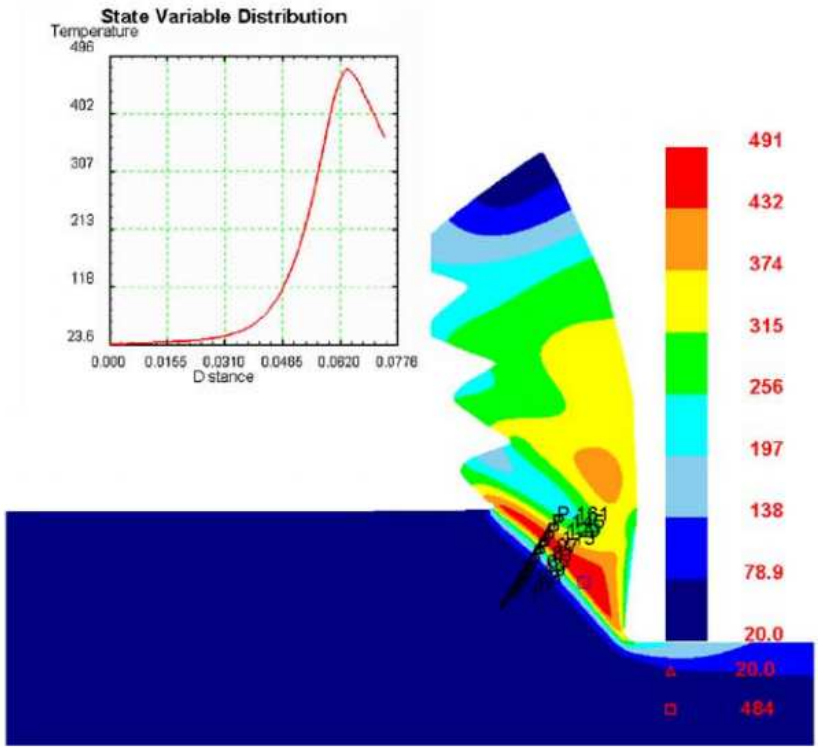

Figure 2.26: Temperature distribution on the forming chip during titanium machining [18]

machining of Ti-6Al-4V using a modified Johnson-Cook equation and predicted the effect of various tool coatings on temperature of the tool. In the model, the authors introduced hyperbolic relationship of strain and strain rate and had different temperature-dependent strain softening terms for different strain rates. In addition, they introduced the chip-tool friction term to simulate more realistic cutting conditions. Figure 2.27 shows the three-dimensional temperature distribution of the tool with no coatings applied. The peak temperatures generated were 250°C higher than previous models due to the addition of the friction factor and the modification of the Johnson-Cook model. It is observed that temperature profile remains at a

nearly constant level near the cutting zone (∼0.5 mm) but drops sharply outside the cutting zone. This indicates the importance of measuring the temperature as close to the cutting edge of the tool and signifies that reducing the temperature at the cutting edge will determine/improve the tool life.

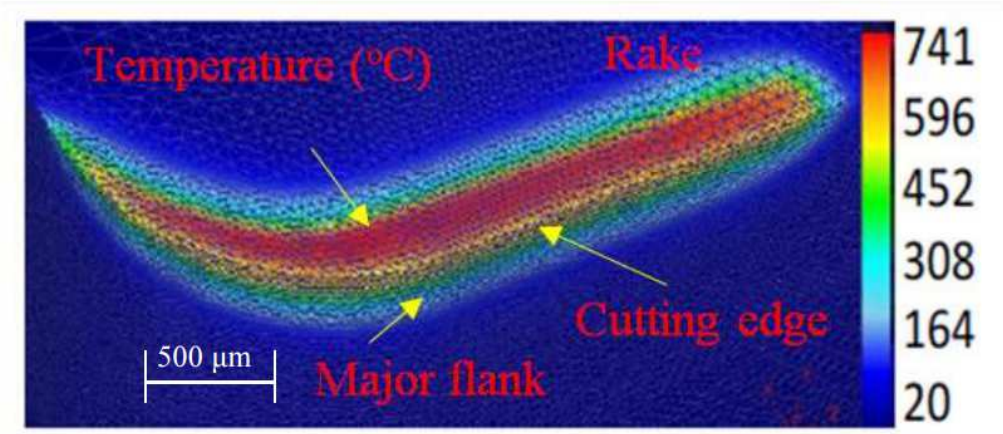

Figure 2.27: Temperature distribution of tool for orthogonal cutting of Ti-6Al-4V [17]

Thepsonthi *et al.* [19] used finite element model to predict the effect of tool cBN (cubic boron nitride) coating on the cutting zone temperature during milling of Ti-6Al-4V alloys. The model constitutes of temperature-dependent strain softening terms. The prediction on temperature profile indicates that using a cBN coating on the tool decreases the cutting temperature of the tool, as shown in Fig. 2.28. As a result, tool wear rate of cBN coated tool is lower than tool wear rate of uncoated WC/Co tool.

Pervaiz *et al.* [20] have conducted FE simulation coupled with CFD simulation to predict the temperature distribution in tool in Ti-6Al-4V machining.

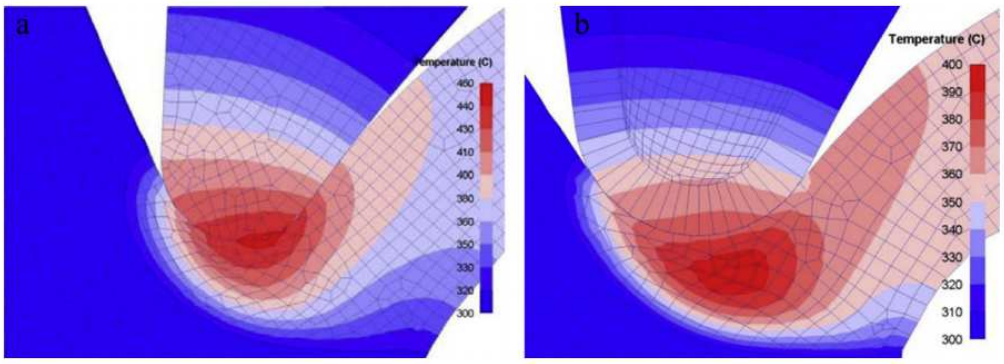

Figure 2.28: Temperature distribution at the cutting zone: (a) WC/Co and (b) cBN coated WC/Co) [19]

Modified version of Johnson-Cook constitutive model was incorporated in the conventional finite element based machining simulations to predict the behavior of flow stresses for Ti-6Al-4V titanium alloy. In the research, the extent of temperature reduction due to presence of dry air is studied. This study is an alternative approach to estimate the temperature distribution of the cutting tool by considering the solid fluid interface approach in commercial CFD software packages. Figure 2.29 shows the temperature profile of the cutting tool obtained from the simulation. However, by considering the flow of air only, this model can only be extended simulate MQL and flood cooling techniques.

2.5 Thermal models of Droplets and Sprays

There are a few droplet and spray heat transfer models in the literature but majority of them deal with temperatures that are lower than the cutting

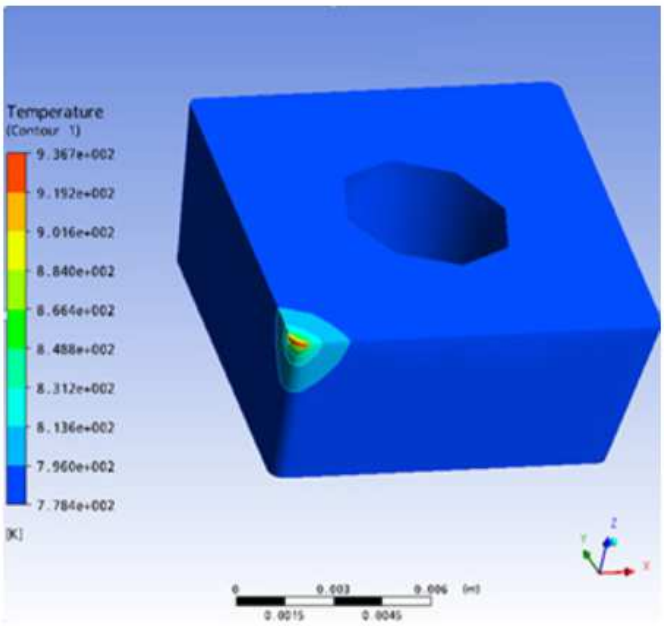

Figure 2.29: Temperature profile of the cutting tool) [20]

zone temperature usually found during titanium machining and also focus on heat transfer within the droplets. Zhao *et al.* [21] formulated a mathematical model for the conjugate heat transfer process in the liquid metal droplet impinging on a glass substrate using time-dependent momentum and energy equations. Cooling of a hot surface with a water droplet was also considered. The droplet-substrate boundary was considered as a conducting interface but the free surface of the droplet included no conduction or convection boundary. The theoretical model was solved numerically utilizing the finite element method with a deforming mesh and grid generation. Results from the predicted temperature distribution during the quench cooling at conditions near maximum spreading for high impact velocities indicate that the heat transfer occurs mainly in the radial direction, despite the fact that the spread

diameter is many times larger than the spread thickness. However, the study focused mainly on the impact shape of the droplets and considered time-dependent metal solidification process only.

Abramzon *et al.* [71] developed a droplet vaporization model for spray combustion in engines that involved heat transfer between the droplet and the free surface. The model included Stefan flow (transport of heat and mass between gas and liquid). The transient liquid heating inside the droplet was calculated using the spherically symmetric 'effective conductivity model'. The 'effective' thermal conductivity of the liquid fuel is introduced to account for the heat enhancement due to the internal liquid circulation. Results from the model are shown in the form of isotherms in Fig. 2.30. It is clear from the droplet isotherms that the study was interested in the heat transfer within the droplet alone and neglected any solid-liquid interface heat transfer. Mehmet *et al.* [22] modeled unsteady convective heat transfer for fuel droplets but the work also focused on the heat transfer between droplet and the ambient gas only and did not include any validation of the model predictions.

Nishio *et al.* [25] modeled heat transfer of dilute spray impinging on hot surface but focused the study on rebound motion. In the model, the local heat flux was assumed to be the sum of the heat flux components by droplets, induced air flow and radiation. To estimate the heat flux component by droplets, it was assumed that the heat flux upon droplet impact is proportional to the energy which heats up the droplet to the saturation

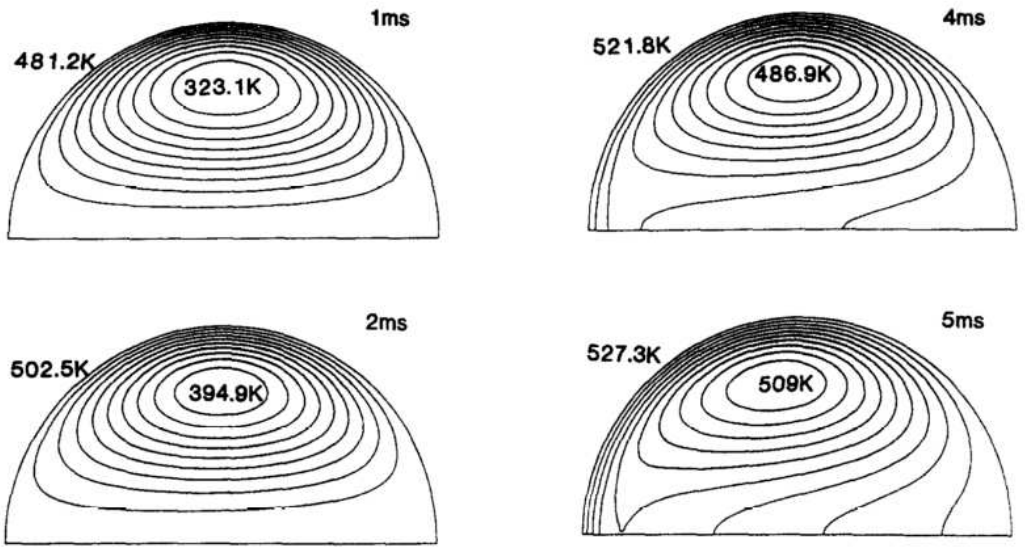

Figure 2.30: Evolution of droplet isotherms at 1, 2, 4 and 5 ms) [71]

temperature. The flight distance of droplets during rebound motion was distributed uniformly from 0 to a maximum length, where the maximum length was an empirical parameter determined from experiments.

Sazhin *et al.* [23] modeled droplet heat transfer model of biodiesel. In the study, a comparative analysis of predictions of several models of biodiesel fuel droplet heating and evaporation in realistic diesel engine-like conditions was presented. The model took into account the contributions of all components of biodiesel fuels, their realistic diffusion, temperature gradient, and recirculation within the droplet (in the case of moving droplets) and predicted the evaporation time for the droplets. Although in this model, the surface temperature was set at 700 K and the droplet initial temperature at 360 K, evaporation of the droplet due at boiling point was considered only. This is expected, since the whole study focused on the droplet and considered the

solid-liquid interface as a fixed temperature boundary only.

Yang *et al.* [24] developed a 3D modeling of droplet heat transfer to understand the fundamental nature of the heat transfer phenomenon of a subcooled droplet upon impact with a superheated flat surface. The numerical technique adopted in their model involved a finite-volume algorithm coupled with the level-set methods that tracks the deformation of the droplet surface. The model included film boiling phenomenon and considered vapor film heat transfer. The temperature profile from the model is shown in Fig. 2.31. The model predicted the time-dependent variation of the super-heated surface temperature, but it did not include any heat source term as encountered in machining and also considered the surface to be isothermal.

Bernardin *et al.* [26] also studied film boiling heat transfer of droplet streams but the relied on empirical correlations based on single droplet stream characteristics and did not include any droplet-surface interaction

2.6 Literature Gap

The atomized spray system has demonstrated that it can improve tool life compared to flood cooling techniques by reducing the average tool temperature but the process by which it does is largely unknown. There is a lack of physics-based understanding of the heat transfer phenomena when the ACF spray system is used that leads lowering of the cutting temperature and increasing the tool life. A possible way of understanding the mechanism could

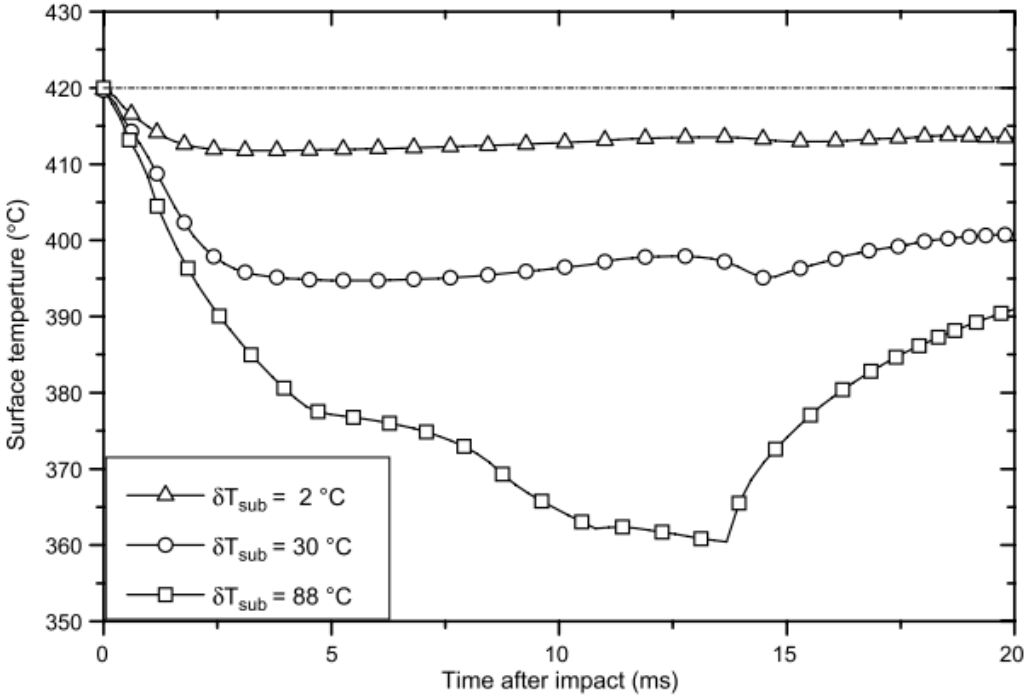

Figure 2.31: The effect of the subcooling degree of the droplet on the transient temperature variation of the heated surface) [24]

be to model the heat transfer process.

A number of works is available in the literature regarding models for predicting temperature during machining of metals and alloys. They focus mainly on the cutting principle of metals to calculate the heat flux and predict the temperature profile at the cutting interface. While most of these models can be extended to titanium machining, they are limited to dry machining and do not include any cooling technique by the cutting fluid. On the other hand, droplet and spray models focus mainly on the deformation and the shape of droplets after impingement. The models that focus on heat

transfer of droplets mostly deal with splashing and evaporation mechanism of droplets at much lower temperatures than those faced in machining. Additionally, the thermal models concentrate on the variation of temperature within the droplets, since many of these models have been developed for spray mechanisms in engines. As a result, the current study needs to be focused on combining the machining heat generation in the tool with the heat transfer from the tool with the aid of droplets/spray.

A study of film formation due to ACF spray impingement has also been made on a cold tool surface. However, the temperature measurements taken show that a very high average temperature ($\sim$ 600°C) is reached during turning of titanium alloys that is likely to initiate boiling heat transfer. Also, the boiling regime should govern if a film or droplets are formed at the cutting interface. Therefore, the model to be developed for the problem should consider the effects of boiling on the ACF spray droplets being impinged on to the heated surface of the tool. Additionally, the model should be able to generate a thermal profile for the tool and predict the temperature near the cutting edge for machining of titanium alloys with ACF spray system.

In the initial studies of the ACF spray system, carbon dioxide seemed to play an important role in reducing the tool temperature. As a result, a study on the effect of the gas on the ACF spray cooling mechanism also needs to be explored.

CHAPTER 3

HEAT TRANSFER MODEL OF ATOMIZED-BASED CUTTING FLUID (ACF) SYSTEM

Atomized-based cutting fluid (ACF) spray system has been established as a viable alternative for difficult-to-cut materials such as Ti alloys [7]. Through the use of atomized cutting fluid (ACF) spray system the tool temperature has been significantly reduced [10]. While it has been established that ACF spray system is an efficient technique for cooling and lubrication in machining, the studies have been primarily experimental in nature [8, 10, 7, 9]. In order to effectively use the ACF spray system in machining, it is essential to understand the spray droplet interaction with the heated tool surface and the mechanism of heat transfer that takes place at the cutting interface.

3.1 Thermal Model Development

In machining Ti-6Al-4V, the temperature can reach as high as 600°C with the use of cutting fluid. As a result, it is highly possible that boiling heat transfer takes place at the cutting interface. However, boiling involves different heat transfer regimes including nucleate and film boiling depending on temperature rise. In order to identify the mechanism that is taking place

during machining, a controlled experiment where the WC tool is placed on a hot plate and the cutting-fluid is sprayed on the rake face of the tool is carried out. The plate is gradually heated to over 300°C and the temperature of the plate/tool is measured with a K-type thermocouple. It is seen that a film is formed for the first few minutes (See Fig. 3.1(a)). However, with time, nucleate boiling is seen to occur near the cutting edge (Fig. 3.1(b)) and after 15 minutes when the temperature is over 300°C, the droplets impinged from the ACF spray system are seen to be skittering around indicating that Leidendfrost point has been reached and the film boiling may be occurring (Fig. 3.1). Since the maximum temperature reached in this experiment is much lower than the tool temperature observed during machining Ti-6Al-4V (300°C<600°C), it can be safely assumed that vapor film boiling through the spreading droplet will dominate during actual machining.

The procedure involved in developing the thermal model that includes film boiling heat transfer shown in Fig. 3.2. First, the initial temperature of the tool surface on which the droplet is being impinged is determined from the heat flux, q' generated during cutting [72]. The heat flux due to film boiling is determined next. Since the film boiling heat flux is a function of heated tool surface temperature and the vapor film thickness, the vapor film thickness is obtained using the maximum spreading length of the droplet, which in turn depends on the spreading regime droplet velocity. Finally, the tool temperature field due to boiling heat transfer that takes place at

Figure 3.1: Film boiling phenomenon: (a) Initial film formation when cold, (b) Nucleate boiling after 8 min, (c) Film boiling after 15 min.

the cutting interface due to ACF spray droplet is then determined from the energy equation using the net heat flux acting at the cutting interface.

3.1.1 Model of Heat Transfer due to an Impinging Droplet

When the droplet impinges on the heated tool surface, the liquid in contact with the high temperature surface vaporizes immediately, forming the vapor film. Some of the vapor molecules escape from the film (this occurs mainly due to the weight of the droplet that forces the vapor out) but the film thickness is maintained due to continuous vaporization at the droplet-film interface. Any heat transfer from the tool surface now occurs through the vapor film. As a result, the determination of the vapor film thickness will provide an estimate of the boiling heat flux, q'' due to the impinged droplet. The configuration of the ACF spray droplet on the heated surface is shown in Fig. 3.3, which depicts an axisymmetric droplet floating on a vapor film of thickness, δ due to the Leidenfrost effect [73]. The surface temperature is designated as T_s and the liquid is assumed to be at the normal boiling

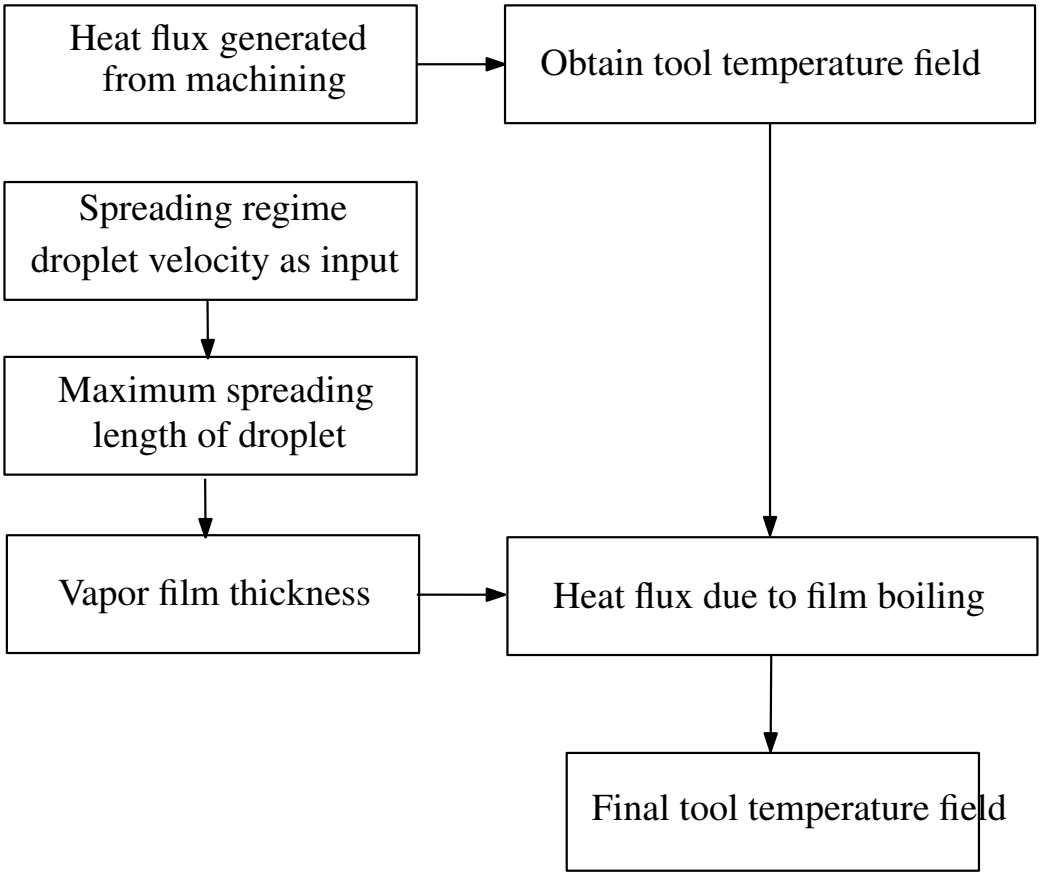

Figure 3.2: Steps in the thermal model

temperature, T_b. The surface at the interface of liquid and vapor is denoted by S_{BC} and is assumed to be flat. The spreading droplet is assumed to be a spherical cap with base diameter, r_0. Using the Fourier's law of heat conduction through the vapor film thickness, the heat flux can be written as:

$$q'' = \frac{k_v(T_s - T_b)}{\delta}. \tag{3.1}$$

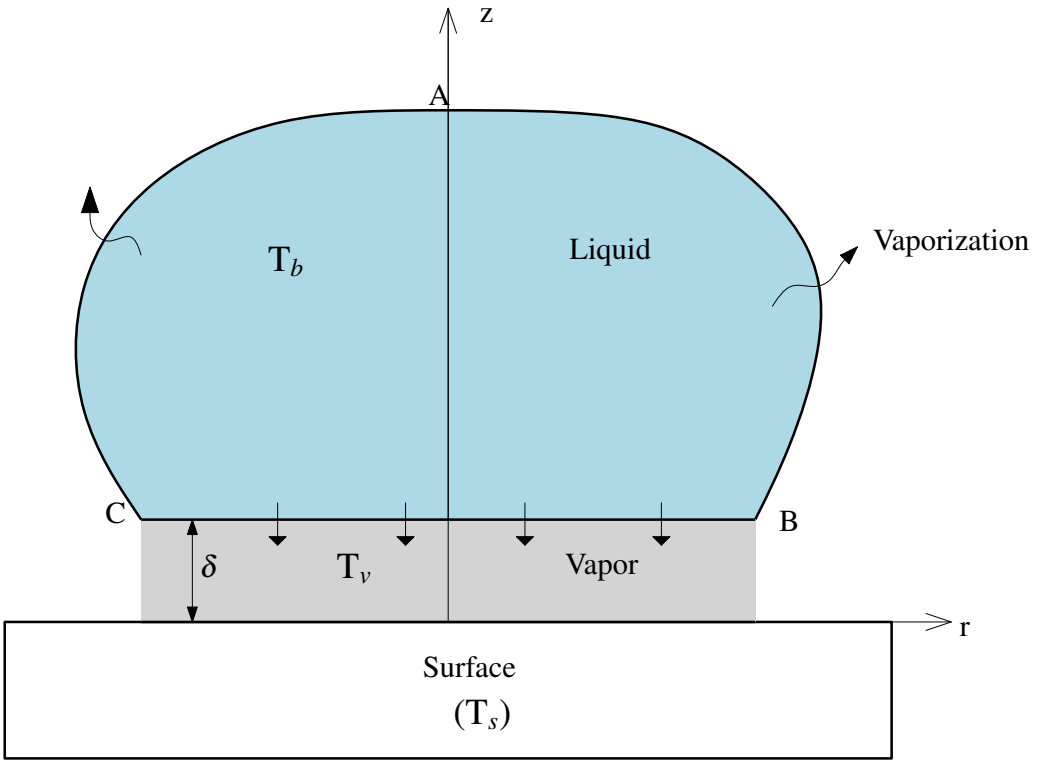

Figure 3.3: Schematic showing the film boiling of droplet

In order to determine the vapor film thickness, δ, the transient problem of heat transfer of a spreading droplet is simplified into a quasi-steady-state problem. The governing equations for vapor phase can be written as:

Continuity:

$$\rho_v v = \rho_v \frac{d\delta}{dt} - \rho_l \frac{ds}{dt}, \tag{3.2}$$

where, v represent axial component of vapor velocity in the film, ρ_v is the vapor density, ρ_l is the liquid density, ds/dt represents the surface (S_{BC}) recession rate due to evaporation.

Momentum:

$$\mu_v \frac{\partial^2 u}{\partial z^2} = \frac{\partial p}{\partial r}, \tag{3.3}$$

$$\frac{\partial p}{\partial z} = -\rho_v g, \tag{3.4}$$

$$\frac{1}{r}\frac{\partial (ru)}{\partial r} + \frac{\partial v}{\partial z} = 0, \tag{3.5}$$

where, μ_v is the vapor viscosity, p is the vapor pressure and u is the radial velocity. Equations 3.2–3.5 are subject to the following boundary conditions:

$$u\Big|_{z=0} = v\Big|_{z=0} = 0, \quad \text{and} \quad u\Big|_{z=\delta} = 0. \quad \text{(no slip condition)} \tag{3.6}$$

Since heat flows from the tool surface to the vapor film, any heat transfer within the vapor film along the radial direction is assumed to be negligible. As a result, the energy equation for the vapor film thickness can be written as,

Energy:

$$k_v \frac{\partial^2 T}{\partial z^2} = 0, \tag{3.7}$$

where, k_v is the vapor thermal conductivity. Equation 3.7 is solved using the following boundary conditions:

$$T\Big|_{z=0} = T_s, \quad T\Big|_{z=\delta} = T_b, \quad \text{and} \tag{3.8}$$

$$\rho_l L_v \frac{ds}{dt} = -k_v \frac{\partial T}{\partial z}\Big|_{z=\delta}. \tag{3.9}$$

It is assumed that the liquid is at a constant temeprature equal to the boiling temperature. ρ_l is the liquid density, L_v is the latent heat of vaporization. Equation 3.9 represents the Stefan's condition that describes evaporation due to the heat flux from liquid to vapor.

The steady-state vapor film thickness, δ can be obtained by solving Eq 3.7–3.9, and is given as:

$$\delta = \frac{k_v}{\rho_l L_v} \frac{(T_b - T_s)}{ds/dt}. \tag{3.10}$$

The recession rate, ds/dt can be determined by studying the force balance of the droplet weight and force caused by the vapor pressure. The force balance is expressed as:

$$\rho_l V(t) g = 2\pi \int_0^{r_0} rpdr, \tag{3.11}$$

where, $V(t)$ represents the liquid volume. The volume, $V(t)$ can be determined by subtracting the volume of the evaporated droplets from the initial

droplet volume, V_0 as,

$$V(t) = V_0 - \int_0^t \left(S_{BC} \frac{ds}{dt} + S_{BAC} \frac{df}{dt} \right), \tag{3.12}$$

where, df/dt represents the evaporation rate over the surface S_{BAC}. Since (S_{BAC}) is very small compared to that of vaporization at the liquid-vapor interface it can be ignored.

The vapor pressure, p can be determined by first solving the momentum Eq. 3.3–3.5 for the axial and radial vapor velocities and then using the continuity Eq. 3.2 along with the boundary conditions given in Eq. 3.6 and applying the pressure boundary as the pressure boundary condition $(p = 0,\ r = D_{max}/2)$. The velocities and pressure are obtained as:

$$u = \frac{1}{2\mu_v} \left(\frac{\partial p}{\partial r} \right) [z(z - \delta)]. \tag{3.13}$$

$$v = -\frac{1}{12\mu_v r} \frac{\partial}{\partial r} \left(r \frac{\partial p}{\partial r} \right) \cdot z^2 (2z - 3\delta). \tag{3.14}$$

$$p = \frac{3\mu_v}{\delta^3} \left(\frac{d\delta}{dt} - \frac{\rho_l}{\rho_v} \frac{ds}{dt} \right) \left(r^2 - r_0^2 \right). \tag{3.15}$$

Substituting the expression of pressure, p from Eq. 3.15 in the force balance Eq. 3.11 yields:

$$\rho_l V(t) g = \frac{3\pi\mu_v r_0^4}{2\delta^3} \left(\frac{d\delta}{dt} - \frac{\rho_l}{\rho_v} \frac{ds}{dt} \right). \tag{3.16}$$

For steady-state condition, $d\delta/dt$ is zero. The steady-state vapor film thickness can now be obtained from Eq. 3.10 by substituting the expression for

ds/dt from Eq. 3.16 and is given as:

$$\delta = \left(\frac{9\mu_v k_v r_0 (T_s - T_b)}{8\rho_v \rho_l g L_v} \right)^{1/4}. \tag{3.17}$$

The evaluation of base diameter of the droplet, r_0 in Eq. 3.17 is discussed in the next section. The film thickness, δ for Eq. 3.17 can be substituted in Eq 3.1 to obtain the heat flux, q''.

Finally, knowing the net heat flux acting at the cutting interface as, $q' - q''$, the boundary condition at the cutting interface can be given as:

$$q' - q'' = k_c \left. \frac{\partial T}{\partial z} \right|_{z=0}, \tag{3.18}$$

where k_c is the thermal conductivity of the tool material. Using this boundary, the temperature field of the whole tool can be obtained using the energy equation for the tool:

$$k_c \left(\frac{\partial^2 T}{\partial x^2} + \frac{\partial^2 T}{\partial y^2} + \frac{\partial^2 T}{\partial z^2} \right) = 0, \tag{3.19}$$

where dx, dy and dz represent the differential dimensions of the tool.

Determination of the Base Diameter of the Droplet, r_0:

To determine r_0 of the impinging droplet, energy balance of the droplet just before and after impingement and at its maximum spreading condition

is considered. The two stages of the droplet are shown Fig. 3.4. It is assumed that the droplet velocity just before impact is such that the interaction of the droplet upon impact is within the spreading regime.

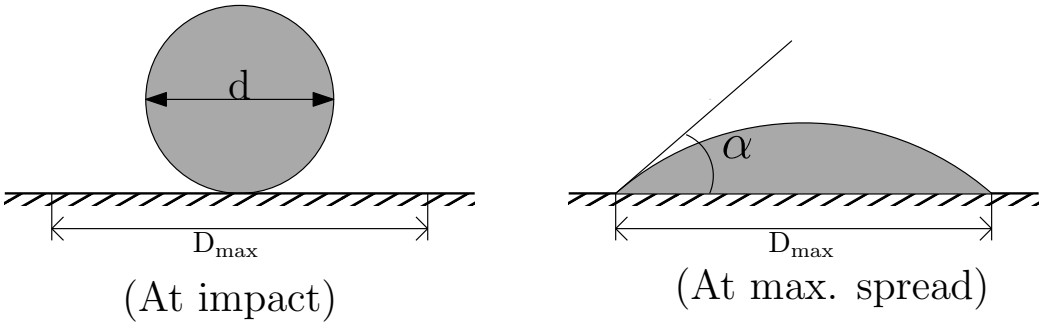

Figure 3.4: Schematic of droplet just before impact and at maximum spreading

At the initial stage, i.e. just before the impact, the droplet of diameter, d possesses both kinetic energy and surface energy. Since the droplet size is small, the potential energy of the droplet is ignored. The initial energy of the droplet-surface system just before the impact (E_1) can be written as [74, 75]:

$$E_1 = K_1 + S_{lg,1} + S_{sg,1}, \tag{3.20}$$

where, K_1 is the initial kinetic energy of the droplet, $S_{lg,1}$ is the initial liquid-air surface energy and $S_{sg,1}$ is the initial solid-air surface energy at the maximum spread of droplet. The initial kinetic energy is given by:

$$K_1 = \left(\frac{1}{6}\pi d^3\right)\left(\frac{1}{2}\rho_l v^2\right), \tag{3.21}$$

where ρ and v are density and velocity of the droplet, respectively. The initial surface energies are given by:

$$S_{lg,1} = \pi d^2 \sigma_{lg}, \tag{3.22}$$

$$S_{sg,1} = \frac{1}{4}\pi D_{max}^2 \sigma_{sg}, \tag{3.23}$$

where, σ_{lg} and σ_{sg} represent the liquid-air surface tension and solid-air surface tension, respectively; and D_{max} is the maximum spreading length of the droplet and v is the velocity of the droplet.

The final energy of the droplet-surface system at maximum spreading length can be written as

$$E_2 = K_2 + S_{lg,2} + S_{sl,2}, \tag{3.24}$$

where, K_2 is the final kinetic energy of the droplet, $S_{lg,2}$ is the final liquid-air surface energy and $S_{sl,2}$ is the final interfacial kinetic energy between the liquid and the surface. Since, the droplet comes to a rest at its maximum spreading length, $K_2 = 0$. Assuming the droplet takes the shape of a spherical cap and the volume of the fluid is constant, the liquid-air surface energy can be written in terms of the contact angle (α) at maximum spreading length:

$$S_{lg,2} = \frac{1}{2}\pi(1 - \cos\alpha)\left(\frac{4}{2 - 3\cos\alpha + \cos^3\alpha}\right)^{2/3} d^2 \sigma_{lg}. \tag{3.25}$$

The interfacial contact energy between solid-liquid is given by [76]:

$$S_{sl,2} = \frac{1}{4}\pi D_{max}^2 \sigma_{sl}, \tag{3.26}$$

where, σ_{sl} is the solid-liquid surface tension.

After the impact, the droplet spreads along the surface leading to an increase in its surface area. During this time, the kinetic energy of the impinging droplet is converted into increasing the surface area and in overcoming the viscous forces. Therefore, the energy conservation equation is given by,

$$E_1 - E_2 - \Pi_{diss} = 0, \tag{3.27}$$

where, Π_{diss} represents the energy of the fluid dissipated during its spread. For low viscosity fluids like water, the dissipation energy was estimated by Pasandideh-Fard *et al.* [77] and Mao *et al.* [78] as:

$$\Pi_{diss} = 0.33\pi \frac{We}{\sqrt{Re}} D_{max}^2 \sigma_{lv}. \tag{3.28}$$

Substituting Eq. 3.20, 3.24 and 3.28 into the eenergy conservation Eq. 3.27 and simplifying, the following relation can be obtained:

$$\frac{1}{2}(1-\cos\alpha)\left(\frac{4}{2-3\cos\alpha+\cos^3\alpha}\right)^{2/3}+ \left(0.33\frac{We}{\sqrt{Re}}-\frac{1}{4}\cos\theta\right)\zeta_{max}^2-1-\frac{We}{12}=0, \tag{3.29}$$

where, ζ_{max} represents the ratio of maximum droplet spreading length to its diameter ($\zeta_{max} = D_{max}/d$). Weber number is obtained from the Eq. 2.3 by using cutting fluid properties and the spreading regime droplet velocity as inputs. The term θ is the equilibrium contact angle is given by Young's equation [79]:

$$\sigma_{lg}\cos\theta = \sigma_{sl} - \sigma_{sg}. \tag{3.30}$$

Park *et al.* [76] studied a single droplet impaction on the solid surface assuming the shape of the droplet as a spherical cap and developed a relation between α and ζ_{max} as,

$$\zeta_{max} = \sin\alpha \cdot \left(\frac{4}{2-3\cos\alpha+\cos^3\alpha}\right)^{1/3}. \tag{3.31}$$

Substituting for ζ_{max} from Eq. 3.31 into Eq.3.29, the value of α is obtained, which is then used in determining ζ_{max} and hence, the maximum spreading length, D_{max}. The base diameter of the droplet, r_0 is then equal to arithmetic mean of maximum spreading length D_{max} and droplet diameter, d.

3.2 Chapter Summary

In this chapter, the thermal model developed for the ACF spray system to predict the temperature of the cutting tool is described. The model considers film boiling as the major heat transfer phenomenon. Film boiling is caused by the high temperature involved in turning of Ti-6Al-4V alloy. Due to this high temperature, the cutting-fluid spray droplets from the ACF spray system form a thin vapor film between themselves and the heated surface due to the rapid vaporization of the liquid when it comes into contact with the surface. In the model, heat transfer through this film by conduction is carried out. Additionally, the model takes into account the temperature variation on the tool surface and develops a film thickness expression as a function of tool surface temperature. The model also considers the deformation of the droplet by taking the maximum spread diameter of the droplet to calculate the film thickness. By obtaining the film thickness, the boiling heat flux and hence, the temperature profile of the tool can be determined. The predicted results and the validation are discussed in Chapter 5.

CHAPTER 4

SPRAY GENERATION MODEL

Since the degree of cooling due to boiling heat transfer that takes place at the cutting interface largely depends on spray characteristics including droplet velocity, a spray model is developed to predict droplet velocity profiles along the spray distance for a given droplet diameter and gas pressure, and establish the spray distance range where the droplets are within the spreading regime needed for ACF spray cooling. The approach used in modeling of the ACF spray is described in this section.

4.1 Spray Model

The model developed to study the spray behavior of the ACF spray system involves two stages: the gas model and the droplet model. The gas model is used for solving the steady-state velocity field of the gas emerging out of the nozzle at a certain high pressure, assuming the flow to be compressible. This is followed by solving for the droplet velocity profiles in the presence of the gas field. The droplets are introduced into the flow field from a droplet generator (source). Droplet velocities are tracked at different positions as the droplets traverse through the gas flow field.

The geometry of the model consists of the ACF droplet nozzle that encloses a high-velocity gas nozzle of a smaller diameter, as shown in Fig. 4.1. The dimensions of the nozzle are taken from the actual nozzle used for ACF spray system characterization measurements by Hoyne *et al.* [9]. Figure 4.2 shows the schematic of the actual ACF spray system and the dimensions of the nozzle and its position with respect to the tool. For the sake of simplicity and for more efficient mesh setup the L-shaped design of the high-velocity nozzle is ignored in the model. The droplet source in the model is assumed to be a rear circular face of the ACF spray nozzle (See Fig. 4.1) and represents the droplet generator (source).

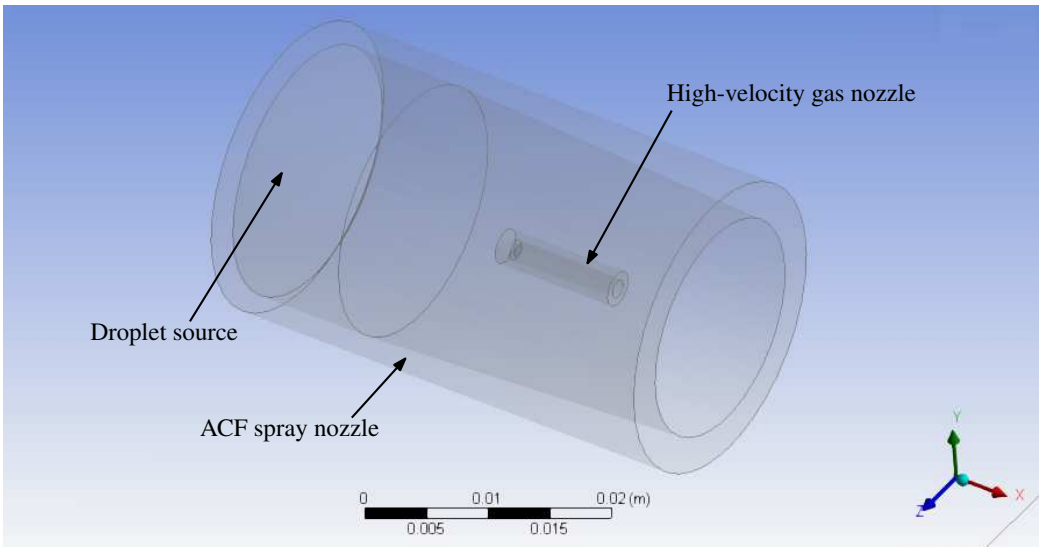

Figure 4.1: Model of the nozzle used in ANSYS Fluent

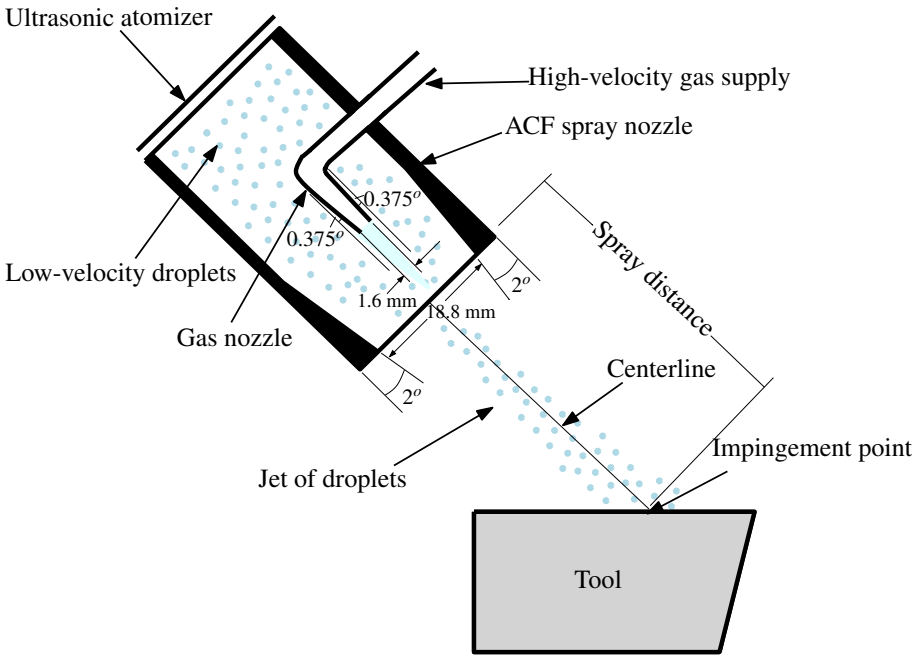

Figure 4.2: ACF spray system setup

4.1.1 Gas Model

The gas model deals with the flow of the gas coming out of the gas nozzle in the ACF spray system. The gas (air) phase is treated as a steady, compressible fuid. At high gas pressure, the Reynold's number is high and as a result, the flow is turbulent. Therefore, the effects of turbulence are accounted for in the flow. Since in turbulent flow the velocities and pressure fluctuate at all points and instances and it is not possible to solve the instantaneous equations directly through conventional continuity and momentum equations, average equations are utilized to solve for the unknowns. Generally, Favre average equations are used for the flow for compressible flows [80]. Favre averaging is density weighted time averaging. Let Φ be any dependent variable and $\overline{\rho}$ be average density. It is convenient to define two different

types of averaging of Φ:

Classical time averaging (Reynolds averaging);

$$\overline{\Phi} \equiv \frac{1}{T}\int_{T} \Phi(t)dt. \tag{4.1}$$

and density weighted time averaging (Favre averaging);

$$\widetilde{\Phi} \equiv \frac{\overline{\rho\Phi}}{\overline{\rho}}. \tag{4.2}$$

The Favre-averaged equations for conservation of mass, momentum and energy that are used in the model are given as [80]:

$$\frac{\partial \rho}{\partial t} + \frac{\partial(\rho u_i)}{\partial x_i} = 0 \tag{4.3}$$

$$\frac{\partial(\rho u_i)}{\partial t} + \frac{\partial(\rho u_j u_i)}{\partial x_j} = -\frac{\partial P}{\partial x_i} + \frac{\partial(\rho\tau_{ji})}{\partial x_j} + \rho f \tag{4.4}$$

$$\frac{\partial[\rho(\frac{1}{2}u_i u_i + k)]}{\partial t} + \frac{\partial[\rho u_j(\frac{1}{2}u_i u_i + k)]}{\partial x_j} = \frac{\partial[(u_i\rho\tau_{ji}) + (\mu + \sigma^*\frac{\rho k}{\omega})\frac{\partial k}{\partial x_j}]}{\partial x_j}, \tag{4.5}$$

where ρ, μ, P, u and f are the average density ($= \overline{\rho}$), dynamic viscosity, Favre averaged pressure, Favre averaged velocity and body force (gravitational force) of the flow, respectively. The variable k represents the turbulent kinetic energy, σ the specific dissipation and $\sigma^*=\frac{1}{2}$. It can be observed from these equations that the flow is compressible in nature. Additionally, the flow is assumed to be steady, which in this case, would eliminate the temporal terms.

A k-ω turbulence model is used to account for convection and diffusion of turbulent energy. The k-ω is one of the most commonly used turbulence models. It is a two-equation model, that is, it includes two extra transport equations to represent the turbulent properties of the flow. This allows the two-equation model to account for history effects like convection and diffusion of turbulent energy. The first transported variable is turbulent kinetic energy, k. The second transported variable in this case is the specific dissipation, ω. It is the variable that determines the scale of the turbulence, whereas the first variable, k, determines the mean kinetic energy per unit mass associated with eddies in turbulent flow.

The extra transport equations are represented as [80]:

$$\frac{\partial k}{\partial t} + u_j \frac{\partial k}{\partial x_j} = \tau_{ij} \frac{\partial u_i}{\partial x_j} - \beta^* k\omega + \frac{\partial}{\partial x_j}\left[(\nu + \sigma^* \nu_T)\frac{\partial k}{\partial x_j}\right] \tag{4.6}$$

$$\frac{\partial \omega}{\partial t} + u_j \frac{\partial \omega}{\partial x_j} = \alpha \frac{\omega}{k} \tau_{ij} \frac{\partial u_i}{\partial x_j} - \beta \omega^2 + \frac{\partial}{\partial x_j}\left[(\nu + \sigma \nu_T)\frac{\partial \omega}{\partial x_j}\right], \tag{4.7}$$

where $\nu_T = k/\omega$ and represents the kinematic eddy viscosity. The closure coefficients and auxiliary equations are given as:

$$\alpha = \frac{5}{9},\ \beta = \frac{3}{40},\ \beta^* = \frac{9}{100},\ \sigma = \frac{1}{2},\ \sigma^* = \frac{1}{2},\ \varepsilon = \beta^* \omega k \tag{4.8}$$

By solving Eq. 4.3–4.7, the pressure and velocity fields can be determined. The gas domain both inside the ACF spray system and outside it in a 20cm x 20cm x 20cm size domain is divided into finite volumes across the space. The

minimum dimension used for this spatial discretization is 0.7 mm. A second-order upwind scheme [81] is used for the discretization of the equations and the velocities and pressures are solved for at each of the nodes using the discretized equations. Figure 4.3 shows a typical vector plot obtained for the velocity field for a gas nozzle pressure of 50 kPa.

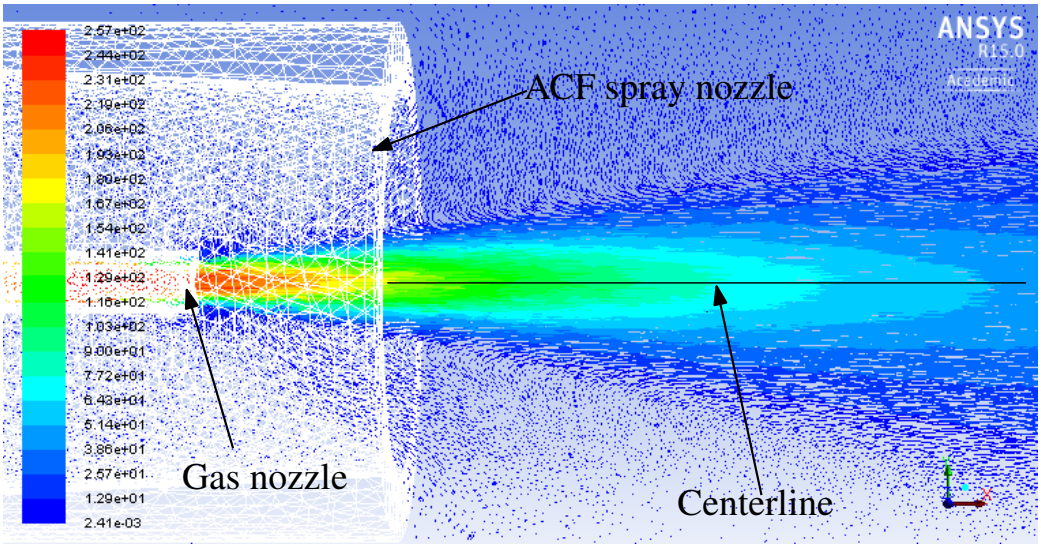

Figure 4.3: Velocity vector plot for 50 kPa gas nozzle pressure

4.1.2 Droplet Model

After obtaining the steady-state gas flow velocity field from the transport equations, the droplet velocity is solved for using force balance on individual droplets as they are released into the domain. The force balance equation used to predict the droplet trajectory is written in the Lagrangian frame of reference. Lagrangian frame of reference is the way of looking at fluid motion where the observer follows the droplet in space and time (as opposed

to Eulerian frame of reference, where the observer focuses on specific locations in the space through which the fluid flows as time passes). The trajectory of the droplet is then obtained by following the droplet's position through time.

The force balance equation for this particular case is written as:

$$\frac{du_p}{dt} = F_d(u - u_p) + \frac{g(\rho_p - \rho)}{\rho_p}, \tag{4.9}$$

where, $F_d(u - u_p)$ is the drag force per unit mass, and F_d is given by [81]:

$$F_d = \frac{18\mu C_d Re}{24\rho_p d_p^2}, \tag{4.10}$$

where, u, u_p, ρ_p, d_p, Re and g are gas velocity, droplet velocity, density of the droplet, diameter of the droplet, Reynolds number and acceleration due to gravity, respectively. Assuming the droplets maintain spherical shape, the drag coefficient C_d is taken as [82],

$$C_d = 0.424, \qquad Re > 1000 \tag{4.11}$$

$$C_d = \frac{24}{Re(1 + \frac{1}{6}Re^{\frac{2}{3}})}, \qquad Re \leq 1000 \tag{4.12}$$

To account for the dispersion of droplets due to the turbulence in the flow, a stochastic tracking method is applied. This method includes the effect of instantaneous turbulent velocity fluctuations on the droplet trajectories. In

this approach, the turbulent dispersion of droplets is predicted by integrating the trajectory equations of individual droplets using instantaneous gas velocity along the droplet path. By computing trajectory for a large number of representative droplets the random effects of turbulence on droplet dispersion in terms of velocity is accounted for. Figure 4.4 shows the droplet velocity contour plot. The droplets gain momentum from the velocity field of the gas (obtained from the gas model) and attain the velocity profile as shown in the figure.

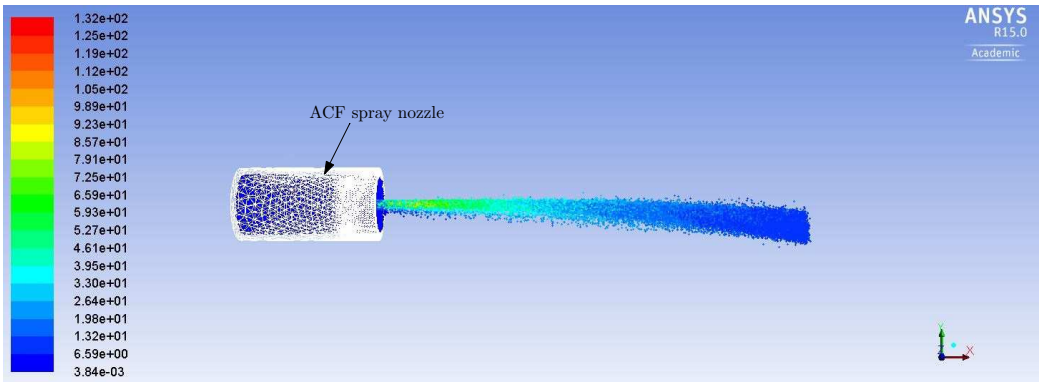

Figure 4.4: Velocity contour plot for 12.5 μm-size droplets sprayed with 50 kPa gas nozzle pressure

4.2 Implementation of the Model

The domain for the gas model and the droplet model are identical as they are both utilized in the same ACF spray system boundaries. The whole ACF spray system is enclosed in a boundary where the walls of the enclosure are at ambient pressure of 1 atm and temperature of 20°C. At the inlet of the gas nozzle of the ACF spray system, a constant gas nozzle pressure of

Table 4.1: Spray simulation parameters

Parameter	Values considered for simulation
Gas type	Air at 20°C
Gas density	1.16 kg/m^3
Cutting-fluid dynamic viscosity	1.22 cP
Cutting fluid density	1001 kg/m^3

P is applied as the input of the model. All other nozzle surfaces have wall boundaries with no-slip condition. Physical properties of droplets are those of the cutting-fluid S-1001 and shape is assumed to be spherical. The properties of the cutting-fluid and gas are tabulated in Table 4.1. Initially, the droplets are given a low velocity of 1 m/s. It is also assumed that the inertia of the droplets does not influence the gas flow field. To solve for the velocity fields for the gas and the droplets as discussed earlier, the commercial software package ANSYS Fluent 15.0 using finite volume method.

4.3 Effect of Droplet Diameter and Gas Nozzle Pressure

To study the effect of droplet size, the diameter of the droplets are varied in the force balance Eq. 4.9 and its effect on velocity of droplets along the ACF spray length is studied. Initially, the droplets are moving with a low velocity (1 m/s). Once the droplets reach the mouth of the gas nozzle, the droplets get entrained by the free shear layer developed due to the large difference between the initial droplet velocity and the high gas velocity, as

shown in Fig. 4.5. Mixing and exchange of momentum between the droplets and the gas occurs and the droplets attain velocities (the high-velocity gas imparts kinetic energy to the liquid droplets, thereby increasing the velocity of droplets) comparable to the gas velocity. The droplets gain momentum and are transported further downstream. In the downstream the droplets move under the influence of the drag force and finally decelerate to a lower velocity. Figure 4.6 shows the gas velocity vectors more closely near the gas nozzle (pressure at 50 kPa), where the arrows represent the vectors obtained from the simulation. The vectors are needed to see the direction of high-velocity gas flow and free-stream gas flow. It is seen that the vectors are directed towards the gas flow showing the influence of the high-velocity gas on the free surrounding gas due to the difference in velocities. Since the high-velocity gas has a low pressure zone, the free stream in its vicinity gets influenced by this high-velocity gas and entrains the droplets from the free stream into the high-velocity jet stream.

Figure 4.7 shows the effect of pressure on the droplet velocity. The higher the gas nozzle pressure, the higher is the velocity for the droplets along the spray distance. For both droplet sizes, the velocity profile attained is similar. Additionally, it is observed that the velocity decreases as the spray distance is increased for both droplet sizes.

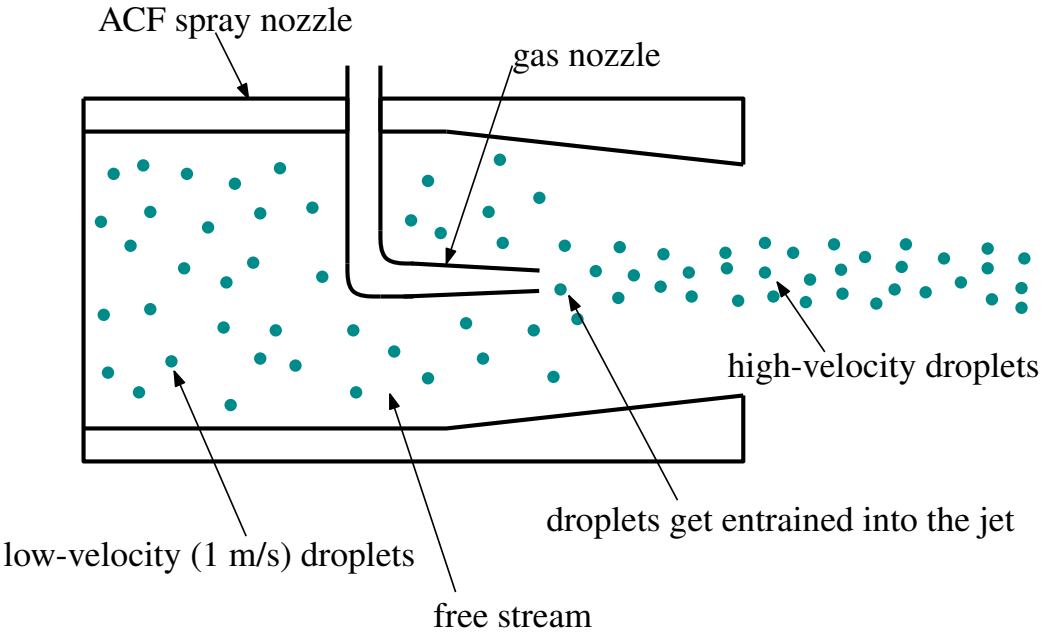

Figure 4.5: Droplet entrainment in the gas flow

4.4 Determination of Spreading Regime Velocity of Droplets

To obtain the ACF spray system parameters that would allow cutting-fluid droplets to spread and contribute to cooling, the spreading regime velocity ranges for the impinging droplets needs to be identified. When the droplets impinge on the surface, four different regimes (rebound, stick, spread, and splash) can occur depending on the impact energy and fluid properties of droplets. The droplet-surface interaction is characterized by several non-dimensional numbers. These include: Reynolds number (Re), Weber number (We) and non-dimensional number, K_m. They are given by:

$$Re = \frac{\rho v d}{\mu}, \tag{4.13}$$

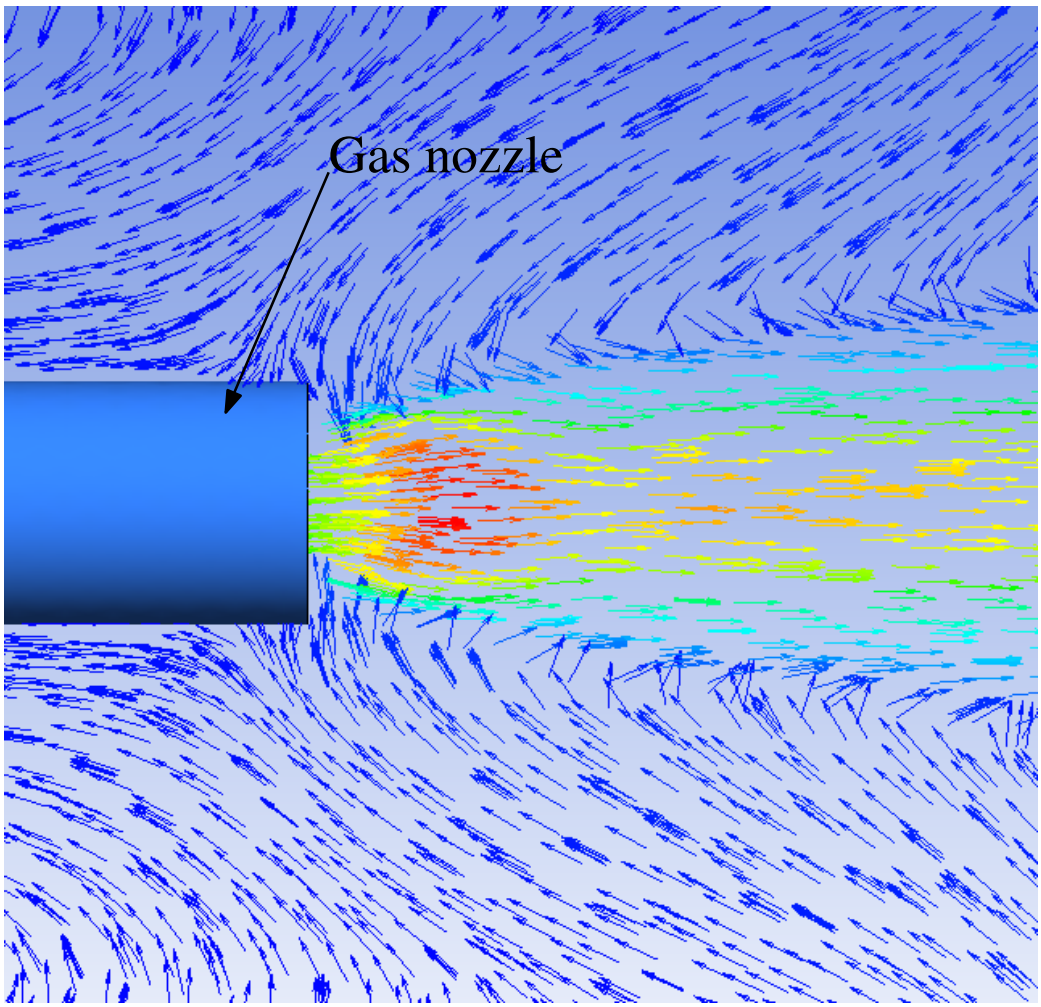

Figure 4.6: Gas velocity vector near the gas nozzle for nozzle pressure of 100 kPa for droplet size of 12.5μm

$$We = \frac{\rho v^2 d}{\sigma}, \tag{4.14}$$

$$K_m = We^{1/2} Re^{1/4}, \tag{4.15}$$

where v ,d, μ, ρ and σ represent the normal component of velocity, diameter, dynamic viscosity, density and surface tension of the droplet, respectively. For $We < 10$, the droplet sticks to the surface. The spreading regime occurs for $We > 10$ and $K_m < 55.7$ [63], in which the impact inertial forces dominate

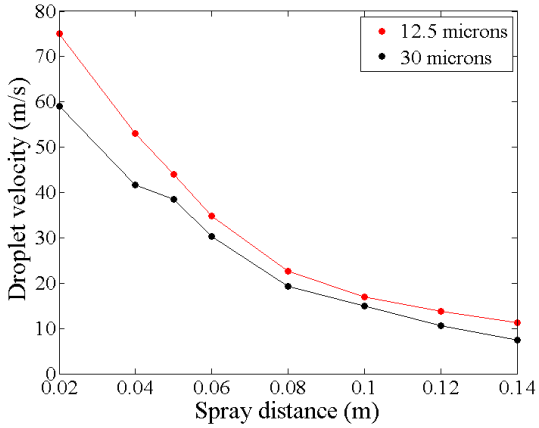

(a) 50 kPa

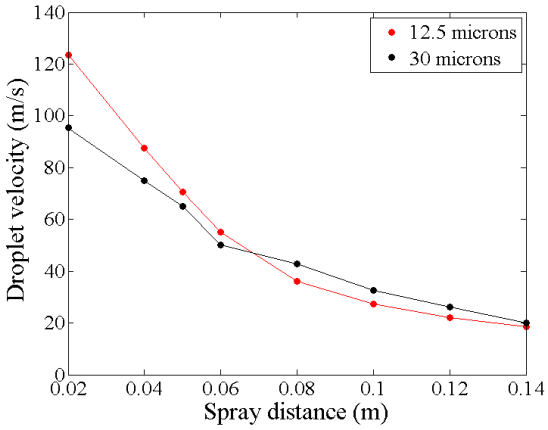

(b) 100 kPa

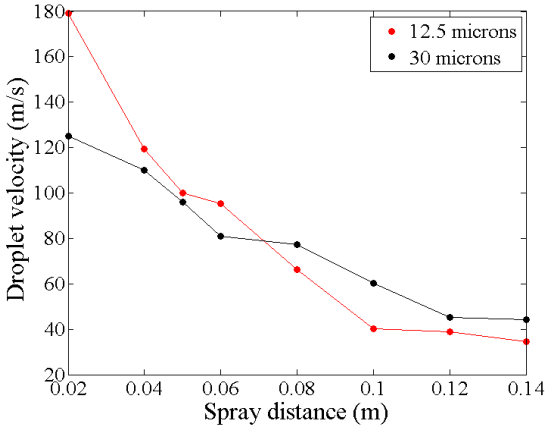

(c) 300 kPa

Figure 4.7: Effect of droplet diameter and gas pressure at (a) 50 kPa, (b) 100 kPa and (c) 300 kPa

and cause spreading of the droplet. For values of $K_m > 55.7$, the impact inertial forces are so high that splashing occurs and the droplet breaks up into tiny droplets. Splashing is undesirable in machining as it would lead to reduction in air quality. Therefore, the spray parameters and fluid properties need to be selected appropriately to be able to achieve the spreading regime that will allow the cutting fluid to enter the cutting interface.

The Weber number and K_m determine the velocity range that will allow the droplet to spread on the surface. The variation of We and K_m with droplet's normal velocity at different droplet diameters is shown in Figs. 4.8 and 4.9, respectively. In the figures, the threshold values of spreading regime are indicated by horizontal lines for $We = 10$ and $K_m = 57.7$. For droplet size of 12.5 μm the droplet velocity between 6 m/s to 40 m/s can ensure the spreading regime. For 30μm droplet size, the droplet velocity range is from 4.2 m/s to 24 m/s. Similarly, for droplet size of 80 μm the range is from 3 m/s to 14 m/s. It is observed that the range of droplet velocities that correspond to the spreading regime is very narrow for the 80 μm sized droplet. This shows that droplet diameter sizes from 12.5 to 30 μm could be used to utilize their wider ranges of spreading regime velocities, with smaller droplet size providing a greater range of velocities for the spreading regime.

For 12.5μm droplet to be within the spreading regime, the spray distance has to be set at a minimum of 55 mm at 50 kPa (See Fig. 4.7). Similarly, for the gas pressures of 100 kPa and 300 kPa, the spray distance is required to

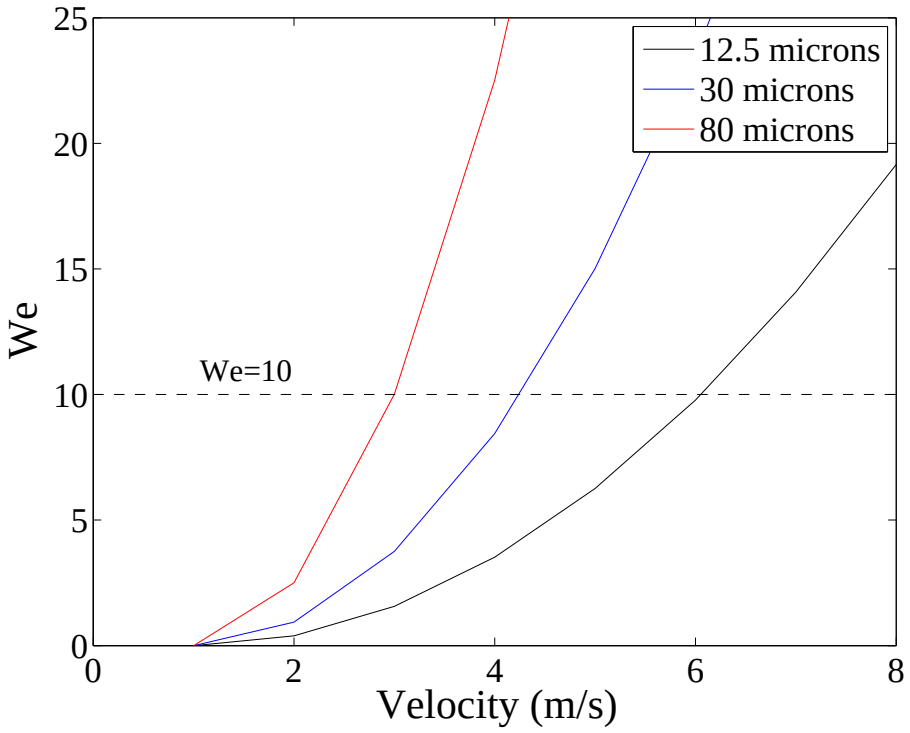

Figure 4.8: We vs. v at different droplet diameters

be set at 80 mm at 100 kPa and 100 mm, respectively. For droplet diameter of 30μm, the spray distance has to be set at a minimum spray distance of 70 mm for 50 kPa and greater than 140 mm for 100 kPa and 300 kPa, which may be difficult to achieve in a limited machine tool work volume. Therefore, the droplet size of 12.5μm, which requires the spray distance to be set at 50 mm or more should be used for ACF spray system. If a longer spray distance is required, then the gas-nozzle pressure can be increased consequently.

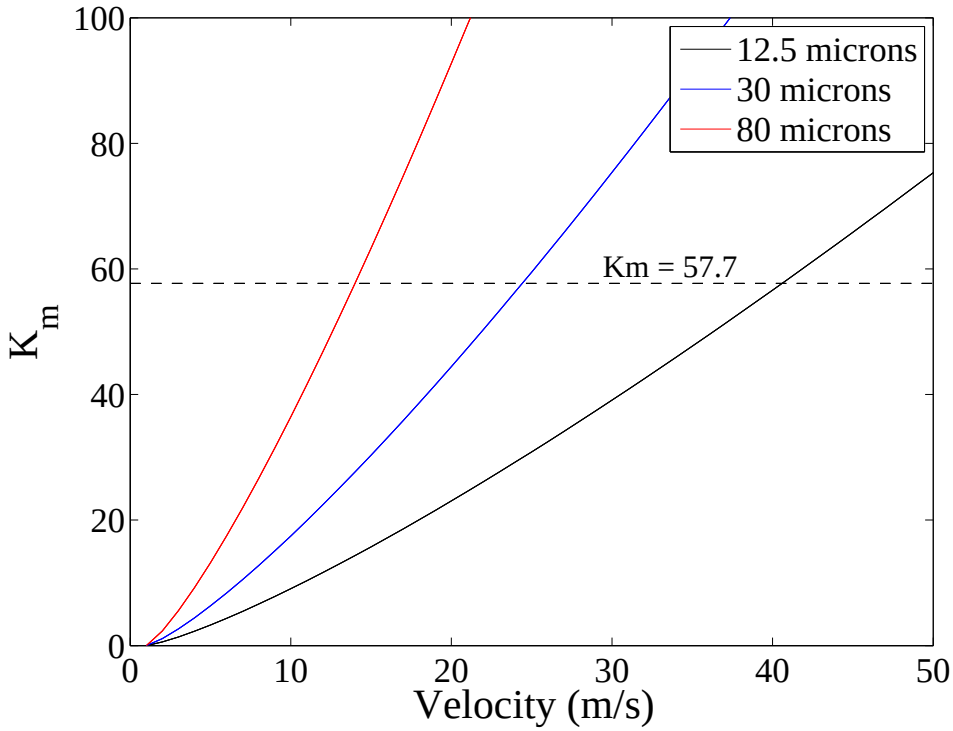

Figure 4.9: K_m vs. v at different droplet diameters

4.5 Chapter Summary

In this chapter, a spray model is developed to predict the ACF spray system parameters including gas nozzle pressure and spray distance that will ensure spreading of the ACF spray droplets and enhance boiling heat transfer on heated tool surface. The model consists of introducing droplets of given sizes to a gas flow field and observing the effect of gas nozzle pressure on the droplets. By changing the pressure, the velocity of droplets along the spray distance is predicted. Since the regime for which the droplets will spread depends on the Weber number, We and non dimensional number, K_m, by determining the threshold for these non-dimensional identities for the given

fluid, the range of spreading velocities are found out. By comparing them with the model's droplet velocity profile, the range of distance along which the droplets will move with spreading regime velocity at different pressure values is identified.

It is found from the simulation that for 12.5 μm droplet to be within the spreading regime, the spray distance has to be set at a minimum of 55 mm at 50 kPa, 80 mm at 100 kPa and 100 mm at 300 kPa. For 30μm droplet size, the spray distance has to be set at a minimum of 70 mm for 50 kPa and greater than 140 mm for 100 kPa and 300 kPa, respectively. Accordingly, the design for an ACF spray system can be made depending on other factors, such as machine tool work volume available and gas pressure requirements.

CHAPTER 5

TEMPERATURE AND GAS FLOW VALIDATION

The objective of this chapter is to validate the temperatures predicted from the thermal model by measuring the temperatures at various locations of the cutting interface during titanium machining with the ACF spray system. The cutting temperature measurement during titanium machining is highly challenging because the low elongation-to-break ratio of titanium leads to a smaller toolchip contact size making sensor placement in the cutting interface difficult. Hence, an inserted thermocouple approach has been used [10]. In addition, the gas velocity profile predicted in the spray model developed in Chapter 4 is validated by measuring the centerline gas velocity for different gas nozzle pressures. Since the gas acts as a carrier for the droplets and has a direct influence on the droplet velocity, as well as challenges associated with measuring the droplet velocities accurately it has been deemed sufficient to measure the gas velocities and compare them with the predicted values from the spray model.

The chapter is divided into two subsections. Section 4.1 presents the experimental setup and design used for cutting temperature measurement and results and Sec.4.2 gives a presentation of experimental setup and validation

for the gas flow velocity measurement.

5.1 Measurement of Tool Temperature

5.1.1 Experimental Setup

Titanium turning experiments are conducted on the Mori Seiki FrontierI lathe. Ti6Al4V workpiece is turned using fresh Kennametal K313 tungsten carbide (WC). The tool insert set in the lathe have principle cutting edge angle of 60^o and orthogonal rake angle of 5^o.

The setup with the ACF spray system is shown in Fig 5.1. It consists of a converging gas nozzle with an exit diameter of 1.6 mm and convergence angle of 0.75° enclosed by a low-velocity droplet nozzle of 18.8 mm and convergence angle of 4°. The ACF spray nozzle is set at a minimum distance of 55 mm from the cutting edge so that the droplet velocity lies in the spreading regime. CO_2 gas and/or air are supplied to the front of the nozzle using a gas supply tube. The high-pressure gas at 50 kPa and flow rate of 20 mL/min are used for the ACF spray system. Cutting fluid S-1001 at 10% dilution in water is used for the experiments [7]. The cutting temperatures are collected for two repeated experiments of 2 cm of cutting length using inserted thermocouple technique. Table 5.1 also includes the ACF spray parameters and cutting conditions used in machining experiments.

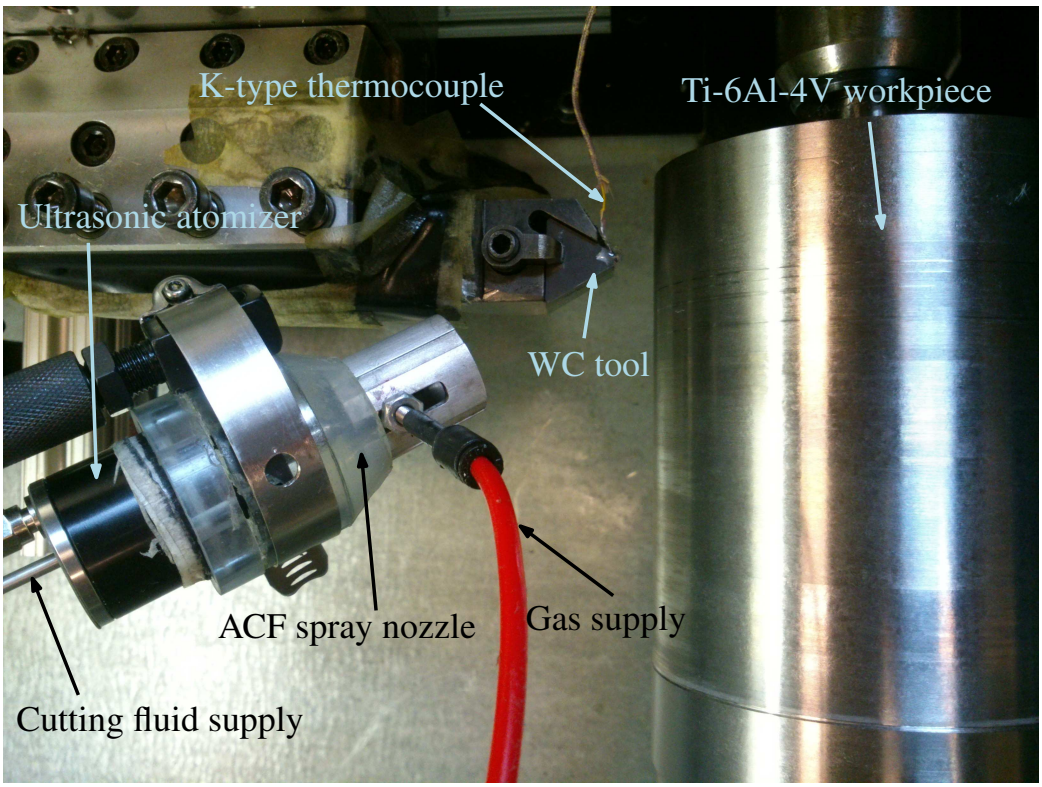

Figure 5.1: Experimental setup for the temperature measurement

5.1.2 Thermocouple Principle

The thermocouple works on the principle of Seebeck effect, which states that an electromotive force (emf) is generated at two junctions when two different or unlike metals (chromel and alumel in this case) are joined together at two junctions and the amount of emf generated varies according to the combinations of the metals. This electromotive force can be used to perform work but in the thermocouple it is used to develop an open-circuit voltage. Under open-circuit conditions where there is no internal current flow, the gradient of voltage is directly proportional to the gradient in temperature. The measured voltage can be found by integrating the electromotive forces

Table 5.1: Values of the parameters used in the experiment

Parameter	Values considered for experiment
Spray distance	55 mm
Gas type	CO_2
Gas pressure	50 kPa
Cutting fluid	S-1001 at 10% (by volume)
Fluid flow rate	20 mL/min
Fluid viscosity	1.22 cP
Depth of cut	1.5 mm
Cutting speed	80, 110 m/min
Feed-rate	0.15, 0.2 mm/rev

along the entire path from the negative terminal of the voltmeter to the positive terminal (See Fig 5.2). The measurement configuration, in this case, has four temperature gradient regions and therefore four voltage contributions:

1. T_{meter} to T_{ref}
2. T_{ref} to T_{sense}
3. T_{sense} to T_{ref}
4. T_{ref} to T_{meter}

The first and the fourth temperature contributions cancel out exactly, since they involve same temperature difference due to presence of a reference temperature, T_{ref} and are made of identical materials. As a result, T_{meter} does not influence the measured voltage. The second and third contributions do not cancel, as they involve different materials, and it is the difference between these values that is registered as a reading. Finally, the readings are calibrated with known temperatures.

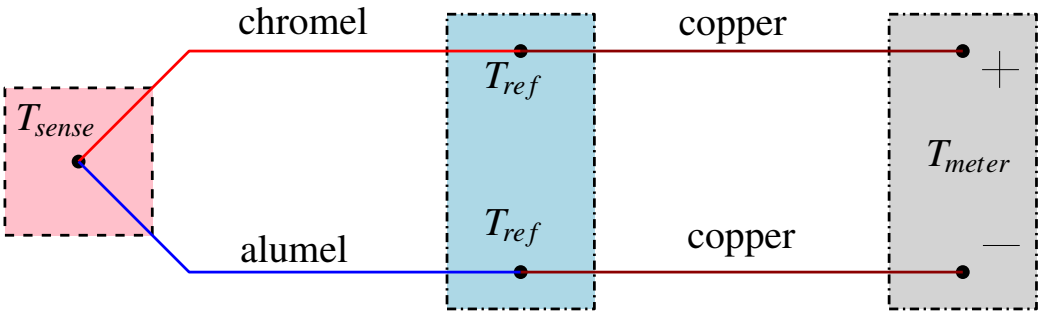

Figure 5.2: Working principle of the thermocouple [10]

5.1.3 Inserted Thermocouple Setup

Due to the small chip-tool interface present during titanium machining, thermocouples need to be placed less than 0.3 mm from the cutting edge so that the cutting interface temperatures could be measured and the temperature gradient could be mapped. The thermocouples are inserted inside the holes machined by electrical discharge machining (EDM) perpendicular to the tool flank, allowing thermocouple placement as close as 0.15 mm from the cutting edge without risk of breakage of the thermocouple wire during machining operations. Figure 5.3 shows the thermocouple placement inside the tool. Since the position of thermocouples in the cutting interface risks immediate damage from the chip forming during machining, they are inserted into blind holes machined into the WC tool inserts. The dimensions (i.e. a_t, b_t, c_t, and d_t in Fig. 5.3) of these holes are chosen to protect both the thermocouple during machining and also to maintain the strength of the tool insert. Thermocouple placements of 0.15mm, 0.2mm, 0.25mm, 0.3mm, 0.35mm and 0.45mm are used to take thermocouple measurements. JB weld

metal adhesive is used for the secure fixture of the thermocouple wires. With temperature data at various lengths a thermal gradient can be plotted and compared with the numerical results. Figure 5.4 shows the respective dimensions and positions of the different holes machined inside the WC tools.

K-type (chromel-alumel) thermocouples from Omega Instruments are used in this study since it can measure temperatures as high as 1300°C. The temperature data is recorded using a National Instrument TC01 Thermocouple Measurement Device at a sampling frequency of 1 Hz.

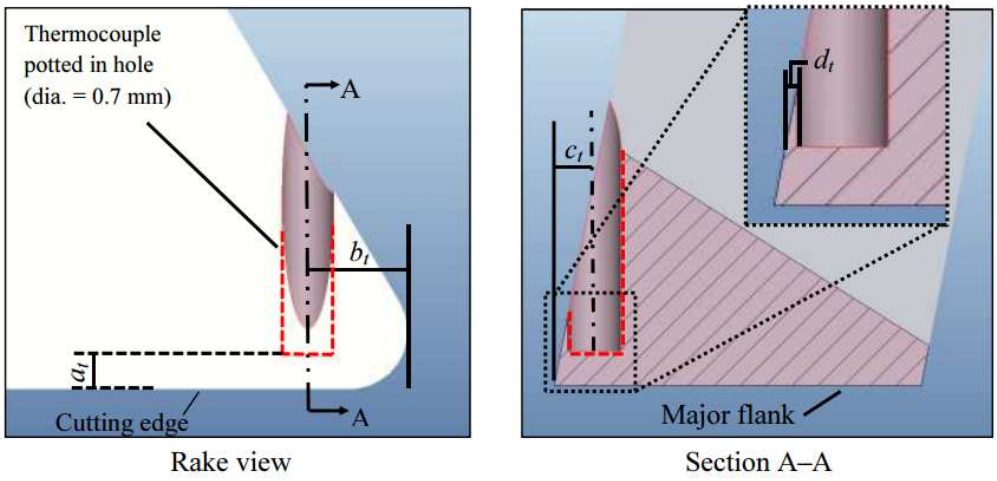

Figure 5.3: Inserted thermocouple setup [9]

5.2 Comparison of Temperature Profiles

In this section, the results obtained from the thermal model described in Chapter 3 are compared with the temperature measurements from the experiment. The boundary conditions and the thermal properties used in the model are described in the following section. The measurements obtained

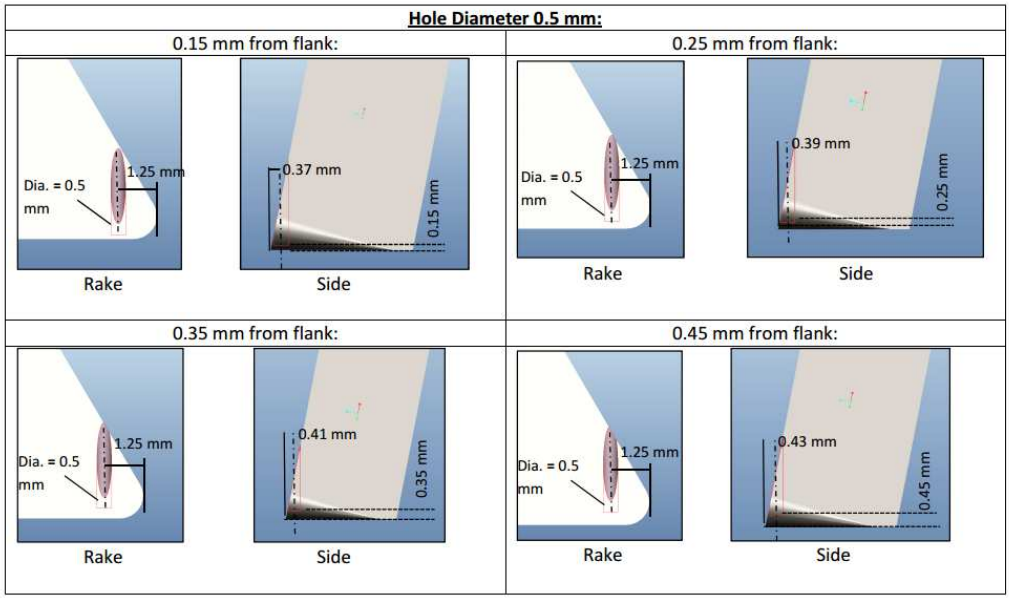

Figure 5.4: Slot dimensions and positions inside the tools for insertion of thermocouples [9]

from the experimental setup are compared with the predicted values along the length of the rake face from the cutting edge. Finally, the temperature fields predicted for different machining conditions are discussed.

5.2.1 Model Predictions

To map the temperature field using the model, the energy equation for the tool domain is solved using finite element technique. The boundary at the cutting interface is considered to be a heat flux boundary condition with a net boiling heat flux acting on the interface. Tool-chip contact lengths are used from the experimental works by Hoyne *et al.* [10] and are used to calculate the cutting interface area over which the net heat flux acts. Table 5.2 shows the contact lengths for the different cutting conditions used. The tool domain

faces that are exposed to surrounding gas have convective surface boundary conditions with convective heat transfer coefficient of 20 W/m^2. Ambient temperature of the surrounding gas is assumed to be 20°C for air and -18°C for CO_2. At the far ends of the tool, adiabatic boundary condition is used. Thermal conductivity and specific heat capacity of the WC tool are taken to be 88 W/m K and 292 J/kg K, respectively. The tool domain is divided into finite elements of size of 0.05 mm and the conduction equation is solved for each of the nodes created to generate the temperature field of the tool during cutting.

Table 5.2: Contact length values for different cutting conditions [10]

Depth of cut (mm)	Feed (mm/rev)	Speed (mm/min)	Contact length (mm)
1.5	0.15	80	0.26
1.5	0.2	80	0.33
1.5	0.2	110	0.34

5.2.2 Validation

Figure 5.5 shows the temperature of the tool predicted by the thermal model as well as mean measured temperature +/- std. dev. for replicated trials along the cutting edge for three sets of machining conditions. The data shows that the predicted temperature profiles follow the decreasing trend as the one created by the measured values (See Table 5.3). Also, the model predictions match reasonably well within the experimental measurements

and lie within the limits of the experimental errors. The data for cutting conditions 0.2 mm/rev and 80 m/min at 0.3 mm could not be measured due to breakage of thermocouple.

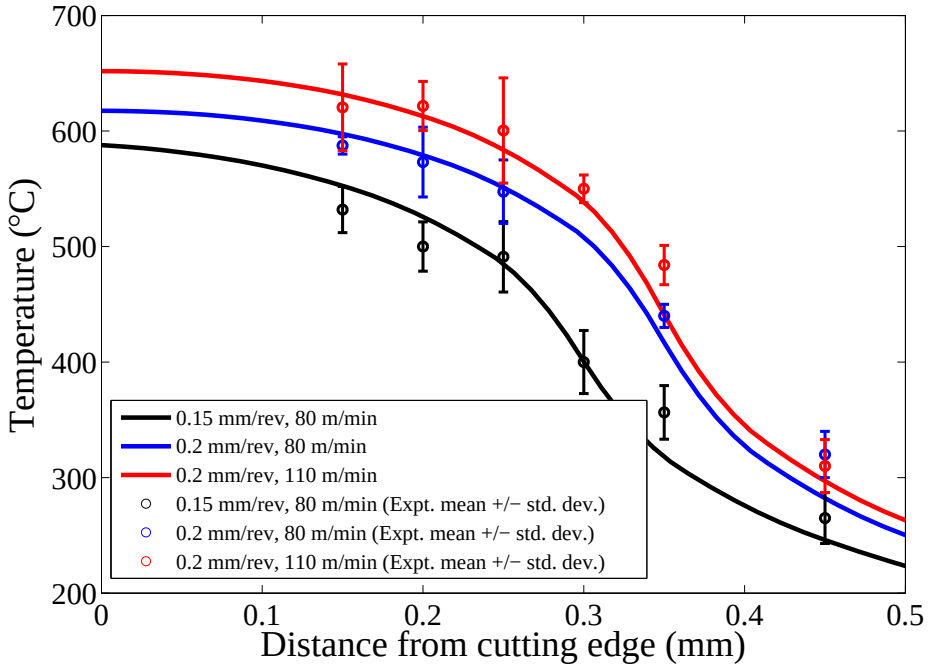

Figure 5.5: Comparison between numerical and experimental results

Figures 5.6 and 5.7 show the temperature profile of the tool from the cutting edge and the temperature field inside the tool for different spray and cutting conditions, respectively. It is observed from Fig. 5.6 and Fig 5.7(a) that the tool temperature at the cutting edge is as high as 1200°C for dry cutting at feed-rate 0.2 mm/rev and speed 80 m/min. The data is comparable to measurements available in the literature [1]. This high temperature is expected because there is no method of cooling present other than free convection. However, using ACF spray system even with air as a high-velocity gas (See Fig. 5.6 and 5.7(e)) shows a considerable decrease in the temper-

Table 5.3: Temperature at different locations from the cutting edge

Cutting conditions	Location (mm)	Temp1 (degC)	Temp2 (degC)	Avg.	Std. Dev.
0.15 mm/rev, 80 m/min	0.15	552	512	532	20
	0.2	521	477	500	21.3
	0.25	522	460	491	30.5
	0.3	427	373	400	27.3
	0.35	380	333	356	23.2
	0.45	287	243	265	22
0.2 mm/rev, 80 m/min	0.15	595	580	588	7.5
	0.2	603	543	573	30.2
	0.25	575	520	548	27.5
	0.3	n/a	n/a	n/a	n/a
	0.35	450	430	440	10
	0.45	340	300	320	20
0.2 mm/rev, 110 m/min	0.15	658	583	621	37.5
	0.2	643	600	622	21.3
	0.25	646	555	601	45.5
	0.3	562	538	550	12
	0.35	501	467	484	17
	0.45	333	287	310	22.9

ature. The temperature drops by almost 40°C at the cutting edge if CO_2 is used with the ACF spray system. This is because of the Joule-Thomson effect of CO_2. CO_2 expands when released from a high-pressure supply. The expansion causes the gas to cool down and lowers the temperature of the gas. This increases the thermal gradient for the heat lost from the tool and consequently, reduces the temperature of the tool.

Figures 5.6 and 5.7 also show the predicted tool temperatures when cutting conditions are varied. It is seen that the temperature at the cutting edge is lowest with feed-rate of 0.15 mm/rev and speed of 80 m/min, and highest with feed-rate of 0.2 mm/rev and speed of 110 m/min. This shows that the temperature increases with increase in both the feed-rate and/or speed, although it is not as high as that for dry cutting. Also, there is a decreasing trend in the temperature for all cutting conditions at distances away from

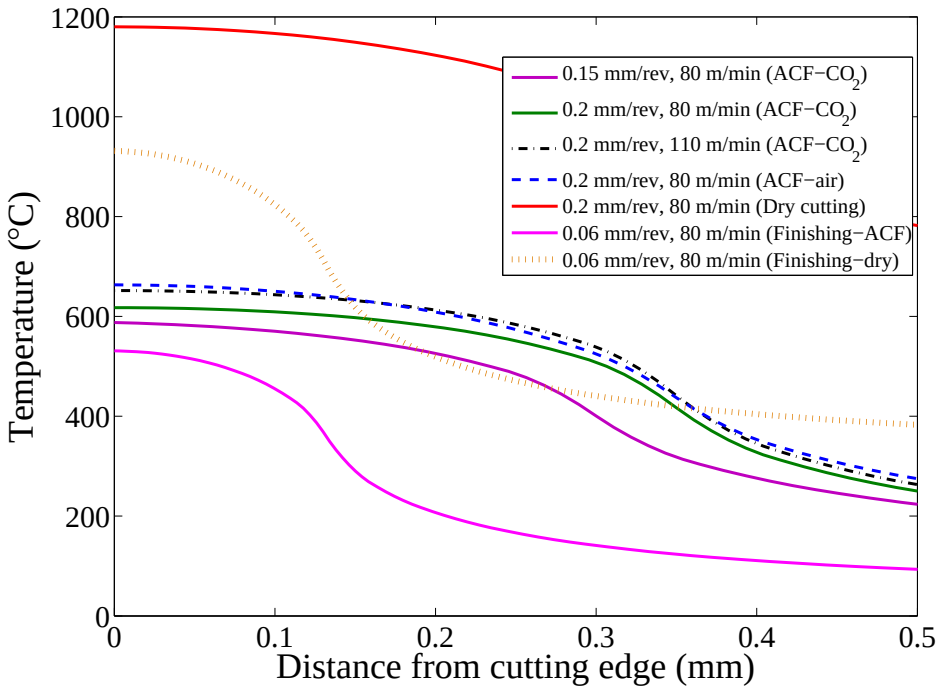

Figure 5.6: Temperature profile for different cutting conditions

the cutting edge. However, for the most conservative cutting conditions the thermal gradient between 0.2 mm and 0.3 mm is slightly larger than those for the other two conditions. This can be attributed to the small tool-chip contact length (See Table 5.2) associated with the cutting conditions of 0.15 mm/rev and 80 m/min, respectively. This further suggests that although the temperature may not be as high as the values for other machining conditions, there is a possibility of thermal degradation due to this slightly steeper thermal gradient. From Fig. 5.7, it is also observed that the flank edge of the tool is exposed to the high temperature during machining titanium as shown by the temperature contours near the flank edge. This means that the flank along with the rake is susceptible to damage during machining of Ti alloys.

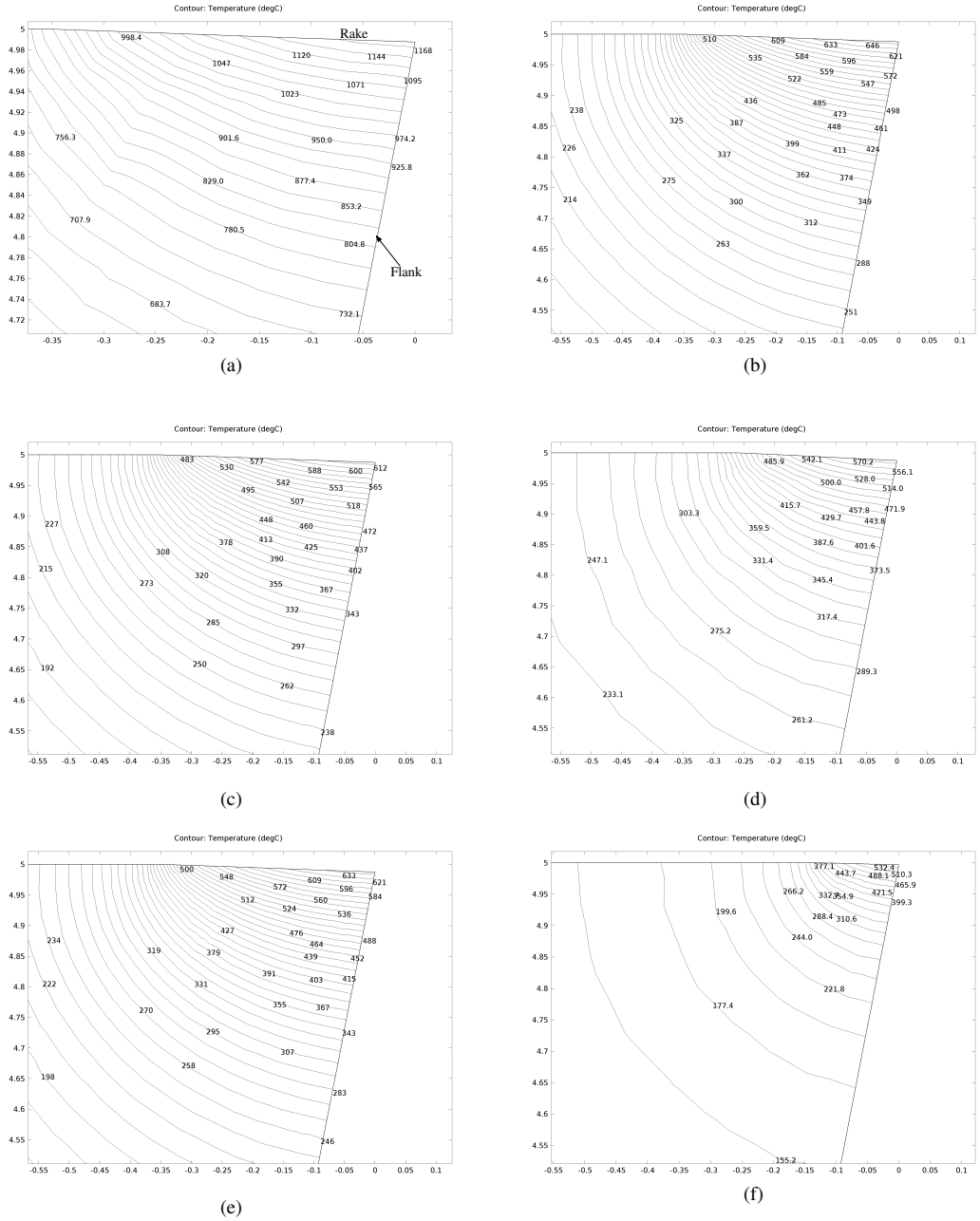

Figure 5.7: Temperature fields for (a) dry cutting at 0.2 mm/rev, 80 m/min; (b) ACF-CO_2 at 0.2 mm/rev, 110 m/min; (c) ACF-CO_2 at 0.2 mm/rev, 80 m/min; (d) ACF-CO_2 at 0.15 mm/rev, 80 m/min; (e) ACF-air at 0.2 mm/rev, 80 m/min; (f) Finishing with ACF-CO_2 at 0.06 mm/rev, 80 m/min;

Figure 5.6 also shows the temperature profile for finish turning at 0.06 mm/rev and 80 m/min predicted by the model. The contact length for finish turning at the specified cutting conditions was obtained from extrapolating data in Table 5.2. It is observed from Fig. 5.6 that the overall temperature is low compared to other cutting conditions described. In fact, the temperature at the cutting edge is below 550°C. Not that only above 550°C, titanium starts to react with tool materials [1] and cause degradation of the tool. Hence, with the ACF spray system, the carbide tool wear slowly and has longer tool life.

5.3 Measurement of Gas Velocity

5.3.1 Experimental Setup

Figure 5.8 shows the experimental setup used for measurement of gas velocity of the ACF spray system. The nozzle used is identical to the one used for tool temperature measurement using the ACF spray system. Compressed air at desired pressure is fed directly to the nozzle. The ACF gas nozzle pressures of 50, 100, 300, 400 and 500 kPa are used in this study. An electronic pitot tube (Range: 0 to 30 psi) is used for measurement of gas velocity. The pitot tube has holes along its length (perpendicular to the flow) along with the tube hole parallel to the flow. The holes perpendicular to the flow measure the static pressure and the tube measures the total pressure. The pressure transducer inside the instrument takes the difference

between these two pressures and evaluates the dynamic pressure, from which the velocity of the flowing gas is calculated.

For validation, the centerline velocity of gas coming out of the nozzle is considered, since it is easier to place the pitot tube concentrically to the nozzle axis. To locate the centerline, the nozzle is fixed on a stage that can slide along horizontal and vertical axes. Using the stage and measuring the maximum pressure with the pitot tube, the centerline of the nozzle is determined. By moving the pitot tube along the centerline further away from the nozzle the pressures at different positions are measured. The pitot tube measures the dynamic pressure of the flow which is then processed to obtain the velocity of the gas flow at different locations.

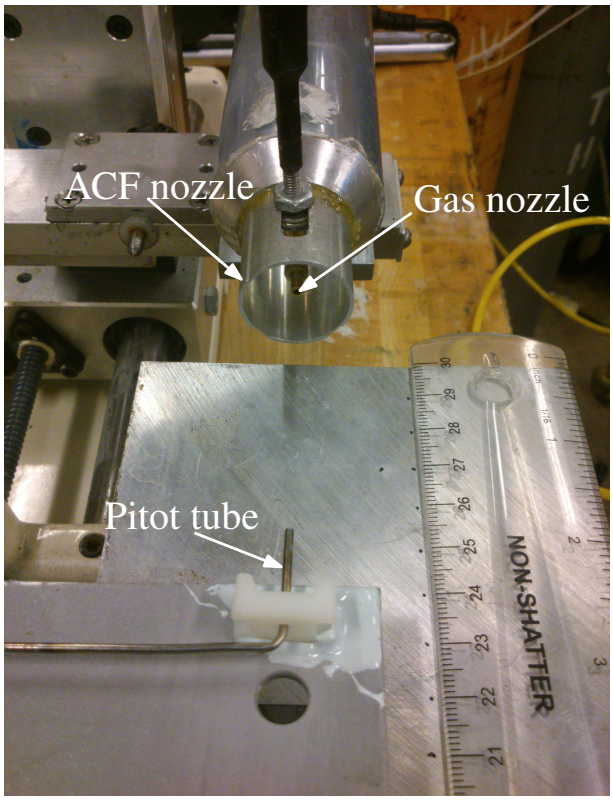

Figure 5.8: Experimental setup for gas flow measurement

Measurement Principle of Pitot Tube

According to the continuity law derived by Bernoulli and the energy equation, the sum of the pressure energy and the potential and kinetic energy of a flowing fluid inside a pipe and in conditions of stationary and frictionless flow is the same at any time and in any part of the pipe.

$$P_{stat} + P_{dyn} = constant. \tag{5.1}$$

The term P_{stat} is the static pressure equally distributed in all directions. The factor, P_{dyn} in the equation represents the dynamic pressure, which is effective in the flow direction. For flowing fluids in horizontal pipes, with a small velocity compared to the Mach-number (Ma<1), the dynamic pressure P_{dyn} of a fluid having density ρ and with a flowing velocity v is calculated as:

$$P_{dyn} = \frac{\rho}{2} v^2. \tag{5.2}$$

If a fixed body is inserted into a flowing fluid (See Fig. 5.9), it will cause the flow to stop immediately upstream of the body and to be completely zero near it. At this point the total pressure P_{S2} is:

$$P_{S2} = P_{stat} + P_{dyn}. \tag{5.3}$$

In the downstream of the body, the sensors are only affected by the direction-independent static pressure, P_{stat}. The difference in the upstream and downstream pressures, the differential pressure ΔP, is then a measure of the velocity with which the inserted body is impacted:

$$\Delta P = P_{S2} - P_{stat} \tag{5.4}$$

Substituting Eq. 5.3 into Eq. 5.4, the velocity of flow can be obtained:

$$v = \sqrt{\frac{2\Delta P}{\rho}} \tag{5.5}$$

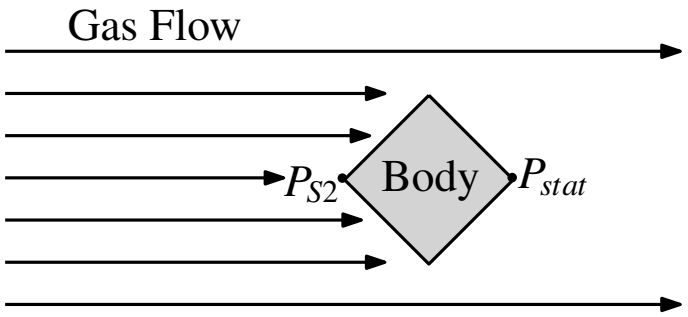

Figure 5.9: Working principle of the pitot tube

5.3.2 Comparison of Gas Velocity Profiles

The velocity contour of gas obtained from the simulation are shown in Fig. 5.10 for different gas nozzle pressures. The gas exits the converging nozzle and due to the large pressure difference between the inlet pressure and the ambient pressure, the gas reaches a very high velocity right after the exit

from the nozzle. This is expected since the sudden decrease in pressure is accompanied by the increase in velocity to conserve energy. It is observed that the overall gas flow velocity increases with increase in the inlet pressure. Further downstream, the velocity decreases but the area over which this high velocity gas influences increases. This is caused by the developing shear layer.

Figure 5.11 compares the velocity of gas predicted from the spray model with the experimental values along the centerline of the ACF spray system (See Fig. 4.2). The centerline velocity starting from the mouth of the ACF spray nozzle to the surface of the tool is validated only since the velocity within that distance is of general interest to determine where the spreading regime velocity occurs. For a given pressure, the gas velocity decreases as distance from the ACF spray system is increased. This is expected as energy gets dissipated to the surrounding and the gas settles down to atmospheric condition. As can be seen for Fig. 5.11, the results from the model closely match the experimental findings with a maximum discrepancy of 11% for all conditions tested.

5.4 Chapter Summary

In summary, it has been observed that the temperature profile predicted by the thermal model closely match with the temperature data obtained from the experimental measurements. For cutting conditions of 0.15 mm/rev and

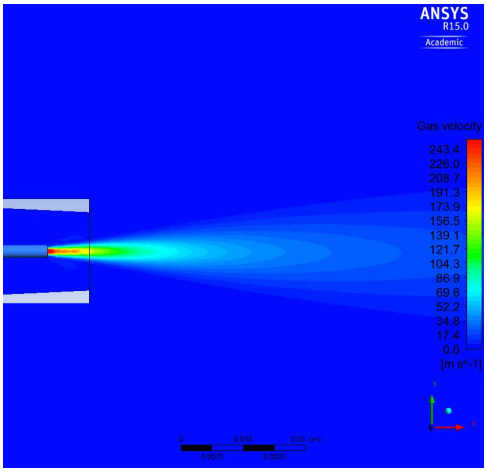

(a) 50 kPa

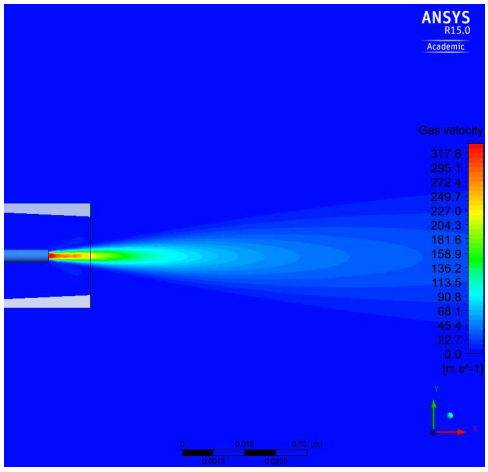

(b) 100 kPa

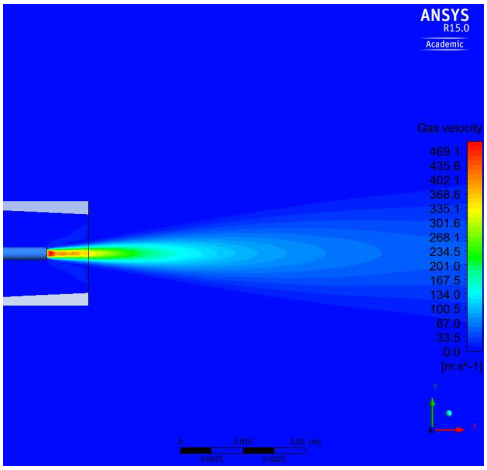

(c) 300 kPa

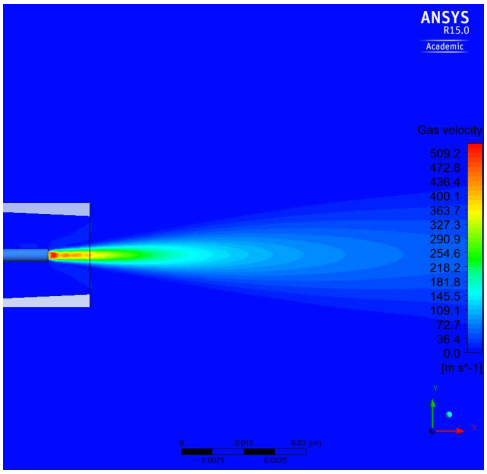

(d) 400 kPa

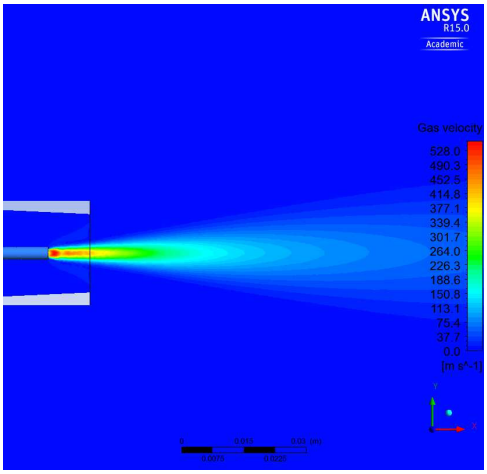

(e) 500 kPa

Figure 5.10: Velocity contour of the ACF spray system gas flow

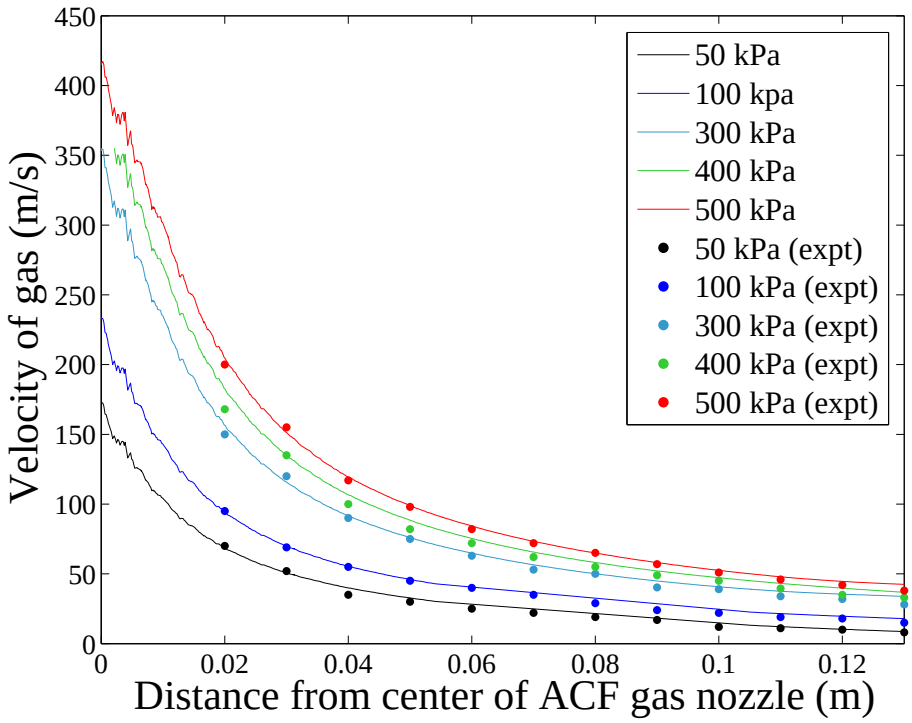

Figure 5.11: Comparison of the experimental and simulated gas velocity profiles

80 m/min, as well as for 0.2 mm/rev and 80 m/min, experimental data match fairly close to the predicted values.

A gas model is also developed and validated in this work. Measurement and validation of gas velocity includes the positioning of pitot tube at the centerline of the nozzle and measuring the velocity at different locations along the line. It is observed that the data from the gas model predicts the actual velocity fairly well, and follows the decreasing trend for all pressure conditions as distance is increased.

CHAPTER 6

CONCLUSIONS AND RECOMMENDATIONS

6.1 Summary

The work presented in this thesis develops a thermal model that simulates the cooling effect due to ACF spray system in machining by incorporating film boiling of droplets. The research also determines the spray parameters through a CFD study for which the droplets formed from the ACF spray system will spread on the heated surface of the tool and therefore, contribute to the heat transfer.

To develop the thermal model, a controlled experiment is conducted at first to observe the heat transfer phenomenon that is likely to take place at the cutting interface at high machining temperatures. A tool is heated to over 300°C and the cutting fluid from the ACF system is sprayed on it. It is observed that boiling heat transfer phenomenon is the dominant form of heat transfer at that temperature. The thermal model is developed with an impinged droplet cushioned over a thin vapor film to replicate the Leidenfrost effect in film boiling. It is through this thin vapor film that heat is conducted away from the tool. Using equations of mass and momentum, the thickness

of the film is first determined and the net heat flux acting on the cutting interface is evaluated and the temperature field of the tool is obtained.

In the spray model, ACF spray parameters are determined for which the droplets being impinged on the surface of the tool are within the spreading regime velocity. Using CFD technique, a gas flow velocity profile is created that simulates the gas nozzle velocity for a given pressure. Cutting fluid droplets are then introduced to the flow field and the resultant velocity of the droplets are evaluated. For a given pressure and droplet size, the spray distance range within which the velocity falls within the spreading range is determined. This ensures that the droplet spreads upon impact with the tool surface and introduce film boiling heat transfer.

6.2 Conclusions

In this study, a thermal model based on the film boiling heat transfer is developed to predict the tool temperature at the cutting edge and map the temperature field in the tool. Additionally, a spray model to determine the minimum spray distance to ensure droplets spread on the heated surface has been formulated. Based on the analyses made from the model results, the following conclusions can be drawn.

1. Boiling is one of the principal heat transfer mechanisms that take place during ACF spray cooling. With tool temperature much above 600°C, film boiling is assumed to take place near the cutting edge. The model

considers heat conduction through the vapor layer formed by film boiling. This work also takes into account the variation of surface temperature in the model unlike most works in literature, where the temperature is assumed to be constant.

2. Due to the high temperature involved at the cutting interface, the cutting-fluid spray from the ACF spray system forms droplets on the heated surface and contributes to the cooling by film boiling heat transfer.

3. The predicted temperature profiles follow the decreasing trend as also seen for the measured data. Also, the model predictions match reasonably well within the experimental measurements and lie within the limits of the experimental errors.

4. The temperature field in the tool provided by the model for dry cutting shows that the cutting edge temperature is almost twice as high as compared to that with ACF spray for cutting conditions of 0.15 mm/rev and 80 m/min.

5. In the ACF spray cooling, the CO_2 gas expands when released from the nozzle and lowers the ambient temperature of the tool. This increases the temperature difference between the tool surface and the surrounding and as a result, enhances the heat transfer rate. The result of this Joule-Thompson effect of CO_2 enables the ACF spray system to reduce

the tool temperature more effectively.

6. Cutting conditions including feed-rate and speed influence the maximum temperature at the cutting edge for machining with ACF spray cooling. However, the temperatures are not as drastically high as in dry cutting.

7. In finish turning of titanium alloy, the ACF spray system provides a cooling effect to keep the cutting temperature below 550°C. As a result, the carbide tool can survive longer without having any significant wear.

8. The spray model that takes into account both the gas flow and the droplet flow is able to demonstrate the entrainment of droplets in the gas jet stream. In addition, it is also able to predict the droplet velocities for a given gas nozzle pressure and droplet size over the spray distance. This helps in determining the distance range at which droplet reaches the spreading regime velocity and is able to contribute to the heat transfer on the heated surface.

9. Droplet size range of 12.5-30 μm has been observed to be suitable for providing a large range in spray distance in the ACF spray system. Increasing the droplet size will narrow the velocity range required for spreading of the droplet.

6.3 Recommendations for Future Work

Below are suggestions for extending the research in order to better predict the temperature of the tool when machining with the ACF spray system.

1. The temperature of the tool is as high as 600°C. As the surface temperature is increased, radiation through the vapor film becomes more significant and the heat flux increases with increasing excess temperature. A model that would include the heat transfer due to radiation is needed.

2. The model could predict the tool temperature profile more accurately if a distribution of the droplets impinging on the surface could be determined. A Rosin-Rammler distribution could be introduced to determine the droplet size and number distribution. By accounting for the number of droplets on an interface area, the temperature of the cutting interface could be better determined.

3. The thermal model should be enhanced to include the solid-fluid interaction between the chip and the droplet. Since, the chip also takes away some heat from the shear zones, involving the geometry of the chip could help predict the temperature of the tool more accurately. This could be done by using a finite element model where the chip is generated from the workpiece by introducing machining conditions. The thermal model could then be incorporated with the resultant domain

to achieve the temperature field.

4. It is assumed in this study that the heat transfer problem is a quasi-steady state one. However, in reality the boiling heat transfer is a result of the constant evaporation of the whole droplet and regeneration of new droplets from the droplet source. The model should be improved by considering the whole transient process from the point of impingement to the complete evaporation of droplets.

5. Further studies should be carried out to determine effect of cutting fluid viscosity on the ACF spray system cooling by varying the fluid properties in the thermal model. Such a study should also investigate the effectiveness of less-hazardous cutting fluids, for e.g. vegetable oil.

6. The thermal model could be applied in machining for predicting tool temperature for other hard-to-machine materials that experience similar temperature-related wear issues as titanium and its alloys. Such a study could reveal any difference in the cooling mechanism for different materials.

REFERENCES

[1] E. Ezugwu and Z. Wang, "Titanium alloys and their machinability," *Journal of Materials Processing Technology*, vol. 68, pp. 262–274, 1997.

[2] A. Machado and J. Wallbank, "Machining of titanium and its alloys - a review," pp. 53–60, 1990.

[3] R. R. Boyer, "An overview on the use of titanium in the aerospace industry," *Materials Science and Engineering A*, vol. 213, no. 1-2, pp. 103–114, 1996.

[4] Y. Li, C. Yang, H. Zhao, S. Qu, X. Li, and Y. Li, "New developments of ti-based alloys for biomedical applications," *Materials*, vol. 7, pp. 1709–1800, 2014.

[5] M. Peters and J. Kumpfert, "Titanium alloys for aerospace applications," *Advanced Engineering ...*, vol. 5, pp. 419–427, 2003.

[6] a. K. Nandy, M. C. Gowrishankar, and S. Paul, "Some studies on high-pressure cooling in turning of Ti-6Al-4V," *International Journal of Machine Tools and Manufacture*, vol. 49, no. 2, pp. 182–198, 2009.

[7] C. Nath, S. G. Kapoor, A. K. Srivastava, and J. Iverson, "Study of Droplet Spray Behavior of an Atomization-Based Cutting Fluid Spray System for Machining Titanium Alloys," *Journal of Manufacturing Science and Engineering*, vol. 136, no. 2, p. 021004, Jan. 2014.

[8] M. B. G. Jun, S. S. Joshi, R. E. DeVor, and S. G. Kapoor, "An Experimental Evaluation of an Atomization-Based Cutting Fluid Application System for Micromachining," *Journal of Manufacturing Science and Engineering*, vol. 130, no. 3, p. 031118, 2008.

[9] A. C. Hoyne, C. Nath, and S. G. Kapoor, "Characterization of Fluid Film Produced by an Atomization-Based Cutting Fluid Spray System During Machining," *Journal of Manufacturing Science and Engineering*, vol. 135, no. 5, p. 051006, Sep. 2013.

[10] A. C. Hoyne, C. Nath, and S. G. Kapoor, "Cutting Temperature Measurement During Titanium Machining with an Atomization-based Cutting Fluid (ACF) Spray System," *IMECE*, 2013.

[11] U. T. M. R. M. B. Davies, M.A. and A. Cooke, "On the measurement of temperature in material removal processes," *Annals of CERP*, vol. 56, pp. 581–604, 2007.

[12] E. Loewen and M. Shaw, "On the analysis of cutting tool temperatures," *Transactions of ASME*, vol. 76, pp. 217–231, 1954.

[13] J. Weiner, "Shear plane temperature distribution in orthogonal cutting," *Transactions of ASME*, vol. 77, p. 1331, 1954.

[14] R. Radulescu, "Dynamic modeling of machining processes using a finite element approach," *M.S. Thesis, UIUC*, 1991.

[15] A. U. Anagonye and D. a. Stephenson, "Modeling Cutting Temperatures for Turning Inserts With Various Tool Geometries and Materials," *Journal of Manufacturing Science and Engineering*, vol. 124, p. 544, 2002.

[16] R. Li and A. Shih, "Finite element modeling of 3D turning of titanium," *International Journal of Advanced Manufacturing Technology*, vol. 29, pp. 253–261, 2006.

[17] M. Sima and Ozel.T, "Modified material constitutive models for serrated chip formation simulations and experimental validation in machining of titanium alloy Ti-6Al-4V," *International Journal of Machine Tools and Manufacture*, vol. 50, pp. 943–960, 2010.

[18] Y. Karpat, "Temperature dependent flow softening of titanium alloy Ti6Al4V An investigation using finite element simulation of machining," *Journal of Materials Processing Technology*, vol. 211, pp. 737–749, 2011.

[19] T. Thepsonthi and T. Özel, "Experimental and finite element simulation based investigations on micro-milling Ti-6Al-4V titanium alloy: Effects of cBN coating on tool wear," *Journal of Materials Processing Technology*, vol. 213, pp. 532–542, Apr. 2013.

[20] S. Pervaiz, I. Deiab, E. M. Ibrahim, A. Rashid, and M. Nicolescua, "A coupled FE and CFD approach to predict the cutting tool temperature profile in machining," *Procedia CIRP*, vol. 17, pp. 750–754, 2014.

[21] Z. Zhao, D. Poulikakos, and J. Fukai, "Heat transfer and fluid dynamics during the collision of a liquid droplet on a substrateI. Modeling," *International Journal of Heat and Mass Transfer*, vol. 39, pp. 2771–2789, 1996.

[22] M. C. Ece and A. Ozturk, "Modelling unsteady convective heat transfer for fuel droplets," *Energy Conversion and Management*, vol. 48, pp. 689–692, 2007.

[23] A. Q. M. Sazhin, S. S., R. Kolodnytska, N. R. Elwardany, a.E., and M. R. Heikal, "Modelling of biodiesel fuel droplet heating and evaporation," *Fuel*, vol. 115, pp. 559–572, 2014.

[24] Y. Ge and L. S. Fan, "3-D modeling of the dynamics and heat transfer characteristics of subcooled droplet impact on a surface with film boiling," *International Journal of Heat and Mass Transfer*, vol. 49, pp. 4231–4249, 2006.

[25] S. Nishio and Y. C. Kim, "Heat transfer of dilute spray impinging on hot surface (simple model focusing on rebound motion and sensible heat of droplets)," *International Journal of Heat and Mass Transfer*, vol. 41, pp. 4113–4119, 1998.

[26] J. D. Bernardin and I. Mudawar, "Transition Boiling Heat Transfer of Droplet Streams and Sprays," *Journal of Heat Transfer*, vol. 129, p. 1605, 2007.

[27] D. Stephenson and J. Agapiou, "Metal cutting theory and practice," 2006.

[28] B. Bannon and E. Mild, "Titanium Alloys for Biomaterial Application: An Overview. Titanium," *Titanium Alloys in Surgical Implants; ASTM*, pp. 7–15, 1983.

[29] D. Williams, "On the mechanisms of biocompatibility," *Biomaterials*, vol. 29, pp. 2941–2953, 2008.

[30] d.-W. J. v.-B. C. Li, J.P. and K. de Groot, "Porous Ti6Al4V scaffold directly fabricating by rapid prototyping: Preparation and in vitro experiment," *Biomaterials*, vol. 27, p. 12231235, 2006.

[31] N. Zlatin and M. Field, "Procedures and precautions in machining titanium alloys," pp. 489–504, 1973.

[32] S. Sun, M. Brandt, and M. Dargusch, "Characteristics of cutting forces and chip formation in machining of titanium alloys," *International Journal of Machine Tools and Manufacture*, vol. 49, pp. 561–568, 2009.

[33] J. Balaji, V. Krishnaraj, and S. Yogeswaraj, "Investigation on High Speed Turning of Titanium Alloys," *Procedia Engineering*, vol. 64, pp. 926–935, 2013.

[34] F. H. F. J. F. Kahles, D. Eylon and M. Field, "Machining of Titanium Alloys," *Journal of Metals*, vol. 37, pp. 27–35, 1985.

[35] Q. Shi, L. Li, N. He, W. Zhao, and X. Liu, "Experimental study in high speed milling of titanium alloy tc21," *The International Journal of Advanced Manufacturing Technology*, vol. 64, pp. 49–54, 2013.

[36] S. Vijay and V. Krishnaraj, "Machining Parameters Optimization in End Milling of Ti-6Al-4V," *Procedia Engineering*, vol. 64, pp. 1079–1088, 2013.

[37] W. Konig, "Applied research on the machinability of titanium and its alloys," *Proc. 47th Meeting of AGARD Structural and Materials Panel*, vol. 202, pp. 1.1–1.10, 1979.

[38] P. Dearnley and A. Grearson, "Evaluation of principal wear mechanisms of cemented carbides and ceramics used for machining titanium alloy IMI 318," *Materials Science and Technology*, vol. 2, pp. 47–58, 1986.

[39] N. Narutaki, "Study on Machining of Titanium Alloys," *Cirp Annals-manufacturing Technology*, vol. 32, pp. 65–69, 1983.

[40] T. Kitagawa, a. Kubo, and K. Maekawa, "Temperature and wear of cutting tools in high-speed machining of Incone1718 and Ti-6A1-6V-2Sn," *Wear*, vol. 202, no. 2, pp. 142–148, 1997.

[41] P. Benardos and G.-C. Vosniakos, "Predicting surface roughness in machining: a review," *International Journal of Machine Tools and Manufacture*, vol. 43, no. 8, pp. 833 – 844, 2003.

[42] C. H. Che-Haron, "Tool life and surface integrity in turning titanium alloy," *Journal of Materials Processing Technology*, vol. 118, pp. 231–237, 2001.

[43] a. K. M. N. Amin, A. F. Ismail, and M. K. Nor Khairusshima, "Effectiveness of uncoated WC-Co and PCD inserts in end milling of titanium alloy-Ti-6Al-4V," *Journal of Materials Processing Technology*, vol. 192-193, pp. 147–158, 2007.

[44] J. Hua and R. Shivpuri, "Prediction of chip morphology and segmentation during the machining of titanium alloys," *Journal of Materials Processing Technology*, vol. 150, pp. 124–133, 2004.

[45] U. K. Ueda N, Matsuo T, "An analysis of saw-toothed chip formation," *CIRP Ann Manuf Technol*, vol. 31, pp. 81–84, 1982.

[46] D. B. J. H. R. Konmanduri, T.A. Schroeder, "Titanium: a model material for analysis of the high-speed machining process, advanced processing methods for titanium, in: D.f. hasson, c.h. hamilton (eds.)," *The Metallurgical Society of ASME*, pp. 241–256.

[47] A. Li, J. Zhao, Y. Zhou, X. Chen, and D. Wang, "Experimental investigation on chip morphologies in high-speed dry milling of titanium alloy Ti-6Al-4V," *International Journal of Advanced Manufacturing Technology*, vol. 62, pp. 933–942, 2012.

[48] S. Palanisamy, S. D. McDonald, and M. S. Dargusch, "Effects of coolant pressure on chip formation while turning Ti6Al4V alloy," *International Journal of Machine Tools and Manufacture*, vol. 49, pp. 739–743, 2009.

[49] S. Y. Hong and Y. Ding, "Cooling approaches and cutting temperatures in cryogenic machining of Ti-6Al-4V," *International Journal of Machine Tools and Manufacture*, vol. 41, pp. 1417–1437, 2001.

[50] K. a. Venugopal, S. Paul, and a. B. Chattopadhyay, "Tool wear in cryogenic turning of Ti-6Al-4V alloy," *Cryogenics*, vol. 47, pp. 12–18, 2007.

[51] A. Cardoni, *Power Ultrasonics*. Elsevier Ltd., 2010, vol. 57.

[52] D. Sindayihebura, M. Dobre, and L. Bolle, "Experimental study of thin liquid film ultrasonic atomization," *4th World Conference on Experimental Heat Transfer, Fluid Mechanics and Thermodynamics*, pp. 1249–1256, 1997.

[53] M. Rukosuyev, C. S. Goo, and M. B. G. Jun, "Understanding the effects of the system parameters of an ultrasonic cutting fluid application system for micro-machining," *Journal of Manufacturing Processes*, vol. 12, no. 2, pp. 92–98, 2010.

[54] "Spray-combustion interaction mechanism of multiple-injection under diesel engine conditions," *Proceedings of the Combustion Institute*, vol. 35, no. 3, pp. 3061–3068, 2014.

[55] R. Payri, A. García, V. Domenech, R. Durrett, and A. H. Plazas, "An experimental study of gasoline effects on injection rate, momentum flux and spray characteristics using a common rail diesel injection system," *Fuel*, vol. 97, pp. 390–399, 2012.

[56] M. Rein, "Phenomena of liquid drop impact on solid and liquid surfaces," *Fluid Dynamics Research*, vol. 12, no. 2, pp. 61–93, 1993.

[57] W. Zhou, D. Loney, A. G. Ferorov, F. L. Degertekin, and D. W. Rosen, "Shape Characterization for Droplet Impingement Dynamics in Ink-Jet Deposition," pp. 1–7, 2015.

[58] A. Yarin, "Drop Impact Dynamics: Splashing, Spreading, Receding, Bouncing..." *Annual Review of Fluid Mechanics*, vol. 38, no. 1, pp. 159–192, 2006.

[59] D. W. Stanton and C. J. Rutland, "Multi-dimensional modeling of thin liquid films and spray-wall interactions resulting from impinging sprays," *International Journal of Heat and Mass Transfer*, vol. 41, no. 20, pp. 3037–3054, Oct. 1998.

[60] K. Range and F. Feuillebois, "Influence of Surface Roughness on Liquid Drop Impact," *Journal of Colloid and Interface Science*, vol. 203, no. 203, pp. 16–30, 1998.

[61] A. V. Mahulkar, G. B. Marin, and G. J. Heynderickx, "Dropletwall interaction upon impingement of heavy hydrocarbon droplets on a heated wall," *Chemical Engineering Science*, vol. 130, pp. 275–289, 2015.

[62] O. W. Jayaratne and B. J. Mason, "The coalescence and bouncing of water drops at an air/water interface," *Proceedings of the Royal Society of London A: Mathematical, Physical and Engineering Sciences*, vol. 280, no. 1383, pp. 545–565, 1964.

[63] C. D. Stow and M. G. Hadfield, "An experimental investigation of fluid flow resulting from the impact of a water drop with an unyielding dry surface," *Proceedings of the Royal Society of London A: Mathematical, Physical and Engineering Sciences*, vol. 373, no. 1755, pp. 419–441, 1981.

[64] C. Mundo, M. Sommerfield, and C. Tropea, "Droplet - Wall Collisions : Experimental Studies of the Deformation and Breakup Process," vol. 21, no. 2, 1995.

[65] C. X. Bai, H. Rusche, and a. D. Gosman, "Modeling of Gasoline Spray Impingment," pp. 1–27, 2002.

[66] A. L. N. Moreira, A. S. Moita, and M. R. Panão, "Advances and challenges in explaining fuel spray impingement: How much of single droplet impact research is useful?" *Progress in Energy and Combustion Science*, vol. 36, pp. 554–580, 2010.

[67] J. Fukai, Y. Shiiba, T. Yamamoto, O. Miyatake, D. Poulikakos, C. M. Megaridis, and Z. Zhao, "Wetting effects on the spreading of a liquid droplet surface : Experiment and modeling colliding with a flat," *Physics of Fluids*, vol. 7, pp. 236–247, 1995.

[68] I. Ghai, J. Wentz, R. E. DeVor, S. G. Kapoor, and J. Samuel, "Droplet Behavior on a Rotating Surface for Atomization-Based Cutting Fluid Application in Micromachining," *Journal of Manufacturing Science and Engineering*, vol. 132, p. 011017, 2010.

[69] D. a. Weiss and A. L. Yarin, "Single drop impact onto liquid films: neck distortion, jetting, tiny bubble entrainment, and crown formation," *Journal of Fluid Mechanics*, vol. 385, pp. 229–254, 1999.

[70] K. J. Trigger and B. T. Chao, "An Analytical Evaluation of Metal Cutting Temperatures," *Trans. ASME*, vol. 73, pp. 57–58, 1951.

[71] B. Abramzon and W. Sirignano, "Droplet vaporization model for spray combustion calculations," *International Journal of Heat and Mass Transfer*, vol. 32, pp. 1605–1618, 1989.

[72] N. Abukhshim, P. Mativenga, and M. Sheikh, "Investigation of heat partition in high speed turning of high strength alloy steel," *International Journal of Machine Tools and Manufacture*, vol. 45, pp. 1687–1695, 2005.

[73] B. Incropera, DeWitt and Lavine, *Fundamentals of Heat and Mass Transfer, 6th edition.*

[74] O. G. Engel, "Waterdrop Collision with Solid Surface," *J. Res. Natn. Bur. Stand.*, vol. 54, p. 281, 1955.

[75] R. E. Ford and C. G. L. Furmidge, "Impact and Spreading of Spray Drops on Foliar Surfaces," *Wetting. Soc. Chem. Industry Monograph*, p. 417, 1967.

[76] H. Park, W. Carr, J. Zhu, and J. Morris, "Single drop impaction on a solid surface," *Fluids Mechanics and Transport Phenomena*, vol. 49, no. 10, pp. 2461–2471, 2003.

[77] M. Pasandideh-Fard, Q. Y. M., S. Chandra, and J. Mostaghimi, "Capillary effects during droplet impact on a solid surface," *Physics of Fluids (1994-present)*, vol. 8, no. 3, pp. 650–659, 1996.

[78] T. Mao, D. C. S. Kuhn, and H. Tran, "Spread and rebound of liquid droplets upon impact on flat surfaces," *AIChE Journal*, vol. 43, no. 9, pp. 2169–2179, 1997.

[79] T. S. Chow, "Wetting of rough surfaces," *Journal of Physics: Condensed Matter*, vol. 10, p. L445, 1998.

[80] D. C. Wilcox, "Formulation of the k-w Turbulence Model Revisited," *AIAA Journal*, vol. 46, pp. 2823–2838, 2008.

[81] "Ansys fluent," http://www.arc.vt.edu/ansys_help.

[82] D. M. A. B. Liu and R. D. Reitz, "Modeling the Effects of Drop Drag and Breakup on Fuel Sprays," *SAE Technical Paper 930072*, 1993.